Advancing the Functionality of Bound States in the Continuum Metasurfaces

Xingye Yang

Munich, 2026

Advancing the Functionality of Bound States in the Continuum Metasurfaces

Xingye Yang

Dissertation
zur Erlangung des Doktorgrades
der Naturwissenschaften (Dr. rer. nat.)
an der Fakultät für Physik
der Ludwig–Maximilians–Universität
München

vorgelegt von
Xingye Yang

aus
Luoyang

München, den 01.02.2026

Erstgutachter: Prof. Dr. Andreas Tittl

Zweitgutachter: PD Dr. Theobald Lohmüller

Tag der mündlichen Prüfung: 26/03/2026

Contents

List of Figures

List of Abbreviations

BIC	Bound states in the continuum
qBIC	Quasi bound states in the continuum
RSP-BIC	Restored symmetry protected bound states in the continuum
g-qBIC	Geometry breaking quasi bound state in the continuum
ε-qBIC	Permittivity breaking quasi bound states in the continuum
Q	Quality factor
BZF	Brillouin zone folding
TE	Transverse electric
TM	Transverse magnetic
PMMA	Poly methyl methacrylate
SNR	Signal-to-noise ratio
RI	Refractive index
FTIR	Fourier-transformed infrared spectroscopy
NA	Numerical aperture
Mid-IR	Mid-infrared
FPA	Focal plane array
FOM	Figure of merit
FOV	Field of view
FWHM	Full width at half maximum
PECVD	Plasma enhanced chemical vapor deposition
RIE	Reactive ion etching
SEM	Scanning electron microscopy

Zusammenfassung

Die Fähigkeit, Licht in ultradünnen optischen Plattformen räumlich zu begrenzen und gezielt zu formen, ist ein zentrales Thema der modernen Nanophotonik. Dielektrische Metasurfaces, bestehend aus subwellenlängigen Resonatoren, die in periodischen Arrays angeordnet sind, bieten einen skalierbaren Ansatz zur gezielten Beeinflussung von optischer Phase, Amplitude und Polarisation, bei gleichzeitiger Kompatibilität mit planaren Fertigungsprozessen. Für viele metasurface-basierte Funktionalitäten, etwa die Brechungsindex- (RI-) Sensorik, die vibronische Molekülspektroskopie, nichtlineare Optik sowie verstärkte Licht–Materie-Wechselwirkung, wird die Leistungsfähigkeit letztlich durch den Resonanzgütefaktor (Q) und die damit verbundene Feldverstärkung bestimmt. Die Realisierung hoch-Q-Resonanzen in praktischen Bauelementen erfordert die gleichzeitige Reduktion zweier Verlustkanäle: (i) intrinsische Verluste infolge von Materialabsorption und Dissipation sowie (ii) Strahlungsverluste durch Kopplung an freie Raumstrahlung. Erstere motivieren den Einsatz verlustarmer dielektrischer Materialien, während letztere durch gebundene Zustände im Kontinuum (bound states in the continuum, BICs) systematisch gestaltet werden können, d. h. nichtstrahlende Eigenzustände, die im Strahlungskontinuum eingebettet sind. In Metasurfaces sind symmetriegeschützte BICs durch kontrollierte Perturbationen zugänglich, die sie in Quasi-BIC (qBIC) Resonanzen überführen und dadurch ultrascharfe spektrale Merkmale bei gleichzeitig messbarer Fernfeldkopplung ermöglichen.

Diese Dissertation etabliert einen kohärenten Rahmen zum Verständnis, zur Auslegung und zur Anwendung von qBIC-Metasurfaces mit verbesserter Praktikabilität und reduzierten Systemanforderungen. Die Arbeit führt von grundlegenden Mechanismen und Verlust-Engineering über polarisationsrobuste Gerätekonzepte bis hin zu kompakten Sensorarchitekturen im mittleren Infrarot (mid-infrared, mid-IR), die auch unter stark absorbierenden Hintergründen funktionsfähig bleiben. Zunächst wird die theoretische Grundlage symmetriegeschützter BICs eingeführt; die Dissertation diskutiert diese aus unterschiedlichen Perspektiven, darunter (i) die quantenmechanische Analogie, welche die Entkopplung von Strahlungskanälen motiviert, (ii) ein wellenphysikalisches Bild mit Fokus auf Symmetrie-Auswahlregeln und Interferenz sowie (iii) die quanti-

tative Beschreibung mittels zeitlicher gekoppelter Modentheorie (temporal coupled-mode theory, TCMT), die Strahlungskopplung, intrinsische Dissipation und experimentell beobachtbare Resonanzlinienformen direkt miteinander verknüpft. Anschließend werden die in dieser Dissertation verwendeten numerischen und experimentellen Methoden zusammengefasst, einschließlich vollständiger elektromagnetischer Simulationen mit periodischen Randbedingungen sowie Nanofabrikationsrouten zur Realisierung dielektrischer Metasurfaces und deren optischer Charakterisierung.

Der erste Teil der Dissertation konzentriert sich auf qBIC-Metasurfaces, deren Strahlungskopplung nicht nur durch die Geometrie, sondern auch durch die umgebende Permittivitätsverteilung bestimmt wird. Während konventionelle geometrie-asymmetrische qBICs nach der Fertigung hohe Q-Faktoren liefern, sind ihre Strahlungsverluste im Wesentlichen festgelegt, was typischerweise zu RI-Antworten führt, die von einer spektralen Verschiebung dominiert werden, ohne die Resonanzmodulation wesentlich zu verändern. Zur Überwindung dieser Einschränkung wird eine permittivitäts-asymmetrische qBIC-Strategie (ε-qBIC) entwickelt, bei der die Umgebungs-RI-Variation in einen effektiven Asymmetrieparameter codiert wird. Mittels Simulationen und Experimenten werden dielektrische Beschichtungen wie Poly(methyl methacrylate) (PMMA) als kontrollierbare Perturbation eingesetzt, deren Dicke und Bedeckungsgrad präzise einstellbar sind, wodurch eine flexible Nach-der-Fertigung-Abstimmung von Resonanzlage und Modulation ermöglicht wird. Entscheidend ist, dass das ε-qBIC-Konzept eine Sensorantwort liefert, die sowohl Resonanzwellenlängenverschiebung als auch Modulationsänderung kombiniert und dadurch eine deutlich verbesserte Linearität bei der Einwellenlängen-Auslese im Vergleich zu geometrie-asymmetrischen qBICs erzielt. Darüber hinaus deuten numerische Untersuchungen darauf hin, dass eine Permittivitätsasymmetrie eine vorgegebene geometrische Asymmetrie kompensieren kann und damit eine optische Wiederherstellung eines ultra-hohen-Q-Zustands nahe der BIC-Bedingung ermöglicht (mit in Simulationen Q-Werten größer als 10^7). Diese “restored-BIC”-Perspektive hebt einen alternativen Freiheitsgrad für das Strahlungsverlust-Engineering hervor und weist Wege zu Bauelementen, deren Strahlungskopplung durch Umgebungs- oder Overlay-kontrollierte Perturbationen abgestimmt werden kann.

Der zweite Teil erweitert qBIC-Metasurfaces hin zu polarisationsunabhängigem Betrieb, motiviert durch die praktischen Einschränkungen polarisationsselek-

tiver Anregung in konventionellen qBIC-Designs. Durch die Verwendung C_4-symmetrischer Einheitszellen können polarisationsunabhängige Resonanzen für beliebige einfallende Polarisationszustände angeregt werden, wodurch die Anforderungen an die Beleuchtung reduziert und die effektive Nutzung des einfallenden Lichts verbessert wird. Es wird ein Metasurface-Design vorgeschlagen und experimentell demonstriert, das auf vier Siliziumquadraten in einem zweidimensionalen Array basiert und dessen qBIC-Eigenschaften durch den Kantenlängenunterschied zwischen verschiedenen Quadraten gesteuert werden. Die realisierte Struktur erreicht ein praktikables Gleichgewicht zwischen Resonanzschärfe und Modulationstiefe, mit einem experimentell beobachteten Q-Faktor von ungefähr 100 und einer Resonanzmodulation von etwa 50%. Dieses Design adressiert einen verbreiteten Zielkonflikt früherer polarisationsunabhängiger Konzepte, bei denen hohe Q-Faktoren oft nur mit schwacher Modulation erreichbar waren oder umgekehrt starke Modulation mit niedrigen Q-Werten einherging. Die gemessene Antwort bleibt über verschiedene Polarisationswinkel hinweg konsistent, was einen robusten Betrieb ohne Polarisationskontrolle unterstützt und die Integration in kompakte optische Systeme erleichtert.

Der dritte Teil kombiniert polarisationsunabhängige qBICs mit räumlichen Modulationsschemata, um eine kompakte molekulare mid-IR-Sensorik unter realistischen, verlustbehafteten Umgebungen zu ermöglichen. Die mid-IR-Vibrationsspektroskopie liefert molekülspezifische Fingerabdrücke, jedoch werden nanophotonische Implementierungen häufig durch Systemkomplexität sowie durch starke Dämpfung in wässrigen Hintergründen erschwert. Dielektrische Metasurfaces mindern die ohmschen Verluste und lokale Erwärmung metallischer Resonatoren und können spektral selektive Resonanzen bereitstellen, die für bildbasierte Auslese geeignet sind. Ihre räumlich ausgedehnten Nahfelder können jedoch stark durch Umgebungsabsorption beeinflusst werden, was den Betrieb in Wasser behindern kann. Um diese Einschränkungen zu überwinden, wird eine kompakte dielektrische Perfect-Absorber-Metasurface entwickelt, die C_4-symmetrische qBICs mit einer Dual-Gradient-Architektur kombiniert. Dabei werden eine in-plane geometrische Perturbation und ein globaler Skalierungsparameter genutzt, um Strahlungsverlust und Resonanzwellenlänge in hohem Maße unabhängig voneinander zu steuern. Dadurch können unterschiedliche Kopplungsregime innerhalb einer einzelnen Metasurface programmiert werden, während über den relevanten Parameterbereich hinweg eine hohe Absorbanz (über 0.8) erhalten bleibt. Die Plattform wird für PMMA-Sensorik in

Luft demonstriert und zeigt eine Absorbanz-Hüllkurvenmodulation von $\sim 20\%$ unter beliebigen Polarisationszuständen. Darüber hinaus wird eine Sensorkonfiguration auf Basis eines residualen dünnen Wasserfilms von ungefähr $700\,\mathrm{nm}$ eingeführt, die qBIC-Resonanzen (Absorbanz ~ 0.5) in der Nähe eines ausgeprägten Wasserabsorptionsbandes erhält und messbare molekulare Signaturen unter Wasserhintergrund mit einer Absorbanz-Hüllkurvenmodulation von über 30% ermöglicht. Diese Ergebnisse unterstützen einen praktikablen Ansatz für die dielektrische metasurface-basierte mid-IR-Sensorik in Umgebungen, die für biologische und wässrige Systeme relevant sind, bei gleichzeitiger Beibehaltung eines kompakten und beleuchtungstoleranten Systems.

Zusammenfassend entwickelt diese Dissertation qBIC-Metasurfaces von einem mechanistischen Verständnis hin zu geräteorientierten Strategien weiter, die Abstimmbarkeit, Linearität, Polarisationsrobustheit und Umweltkompatibilität verbessern. Die Konzepte der permittivitäts-asymmetrischen qBICs und der restored-BICs führen einen zusätzlichen Freiheitsgrad ein, um Umgebungsänderungen in die Strahlungskopplung zu codieren und dadurch eine zuverlässigere Einwellenlängen-Sensorik zu ermöglichen. Die C_4-symmetrische qBIC-Plattform lockert Polarisationsanforderungen und erhöht die praktische Robustheit. Die Dual-Gradient-Perfect-Absorber-Architektur erweitert polarisationsunabhängige qBIC-Metasurfaces schließlich zu kompakten mid-IR-Sensorikschemata, die auch unter stark absorbierenden Hintergründen funktionsfähig bleiben. Insgesamt tragen diese Entwicklungen dazu bei, hoch-Q-nanophotonische Konzepte mit praktikableren Metasurface-Systemen zu verbinden, Systemanforderungen zu reduzieren und gleichzeitig die Funktionalität für Sensorik und verwandte Anwendungen der Licht–Materie-Wechselwirkung zu erweitern.

Abstract

The capability to confine and tailor light within ultrathin optical platforms is a central theme in modern nanophotonics. Dielectric metasurfaces, composed of subwavelength resonators arranged in periodic arrays, offer a scalable route to engineer optical phase, amplitude, and polarization, while maintaining compatibility with planar fabrication. For many metasurface-enabled functionalities, such as refractive index (RI) sensing, vibrational molecular spectroscopy, nonlinear optics, and enhanced ligh-matter coupling, the performance is ultimately governed by the resonance quality factor (Q) and the associated field enhancement. Achieving high-Q resonances in practical devices requires the simultaneous mitigation of two loss channels: (i) intrinsic loss originating from material absorption and dissipation, and (ii) radiative loss caused by coupling to free-space radiation. The former motivates the use of low-loss dielectric materials, whereas the latter can be systematically engineered through bound states in the continuum (BICs), which are non-radiating eigenstates embedded within the radiation continuum. In metasurfaces, symmetry-protected BICs can be accessed through controlled perturbations that convert them into quasi-BIC (qBIC) resonances, thereby enabling ultra-sharp spectral features while retaining measurable far-field coupling.

This thesis establishes a coherent framework for understanding, designing, and deploying qBIC metasurfaces with improved practicality and reduced system constraints. The work progresses from fundamental mechanism and loss engineering, to polarization-robust device concepts, and finally to compact mid-infrared (mid-IR) sensing architectures that remain functional under strongly absorptive backgrounds. First we introduce the theoretical basis of symmetry-protected BICs, the thesis discusses them from different perspectives, including (i) the quantum-mechanical analogy that motivates decoupling from radiation channels, (ii) an wave-physical picture emphasizing symmetry selection rules and interference, and (iii) the quantitative description provided by temporal coupled-mode theory (TCMT), which directly connects radiative coupling, intrinsic dissipation, and experimentally observable resonance line shapes. The numerical and experimental methodologies used throughout this thesis are then summarized, covering full-wave electromagnetic simulations with peri-

odic boundary conditions and nanofabrication routes for dielectric metasurface realization and optical characterization.

The first part of the thesis focuses on qBIC metasurfaces whose radiative coupling is controlled not only by geometry but also by the surrounding permittivity distribution. While conventional geometry-asymmetric qBICs provide high Q after fabrication, their radiative loss is essentially fixed, which typically leads to RI responses dominated by a spectral shift without a substantial modification of the resonance modulation. To address this limitation, a permittivity-asymmetric qBIC (ε-qBIC) strategy is developed, in which the environmental RI variation is encoded into an effective asymmetry factor. Through simulations and experiments, dielectric coatings such as poly(methyl methacrylate) (PMMA) are used as a controllable perturbation whose thickness and coverage can be precisely adjusted, enabling flexible post-fabrication tuning. Importantly, the ε-qBIC concept yields a sensing response that combines resonance wavelength shift and modulation variation, leading to a substantially improved linearity in single-wavelength readout compared to geometry-asymmetric qBICs. In addition, numerical investigations indicate that permittivity asymmetry can compensate a pre-defined geometric asymmetry, enabling an optical restoration of an ultra-high-Q state approaching the BIC condition (with Q exceeding 10^7 in simulations). This "restored-BIC" perspective highlights an alternative degree of freedom for engineering radiative loss and suggests routes toward devices whose radiative coupling can be tuned through environmental or overlay-controlled perturbations.

The second part extends qBIC metasurfaces toward polarization-independent operation, motivated by the practical limitations of polarization-selective excitation in conventional qBIC designs. By adopting C_4-symmetric unit cells, polarization-independent resonances can be excited under arbitrary incident polarization states, thereby relaxing illumination requirements and improving the effective utilization of incident light. A metasurface design based on four silicon squares in a two-dimensional array is proposed and experimentally demonstrated, where the qBIC properties are controlled through the edge-length difference between different squares. The realized structure achieves a practical balance between resonance sharpness and modulation depth, with an experimentally observed Q factor of approximately 100 and a resonance modulation around 50%. This design addresses a common trade-off in prior polarization-independent concepts, where high Q often came with weak modulation or, conversely, strong modulation was accompanied by a low Q. The measured response remains con-

sistent across different polarization angles, supporting robust operation without polarization control and facilitating integration into compact optical systems.

The third part combines polarization-independent qBICs with spatial modulation schemes to enable compact mid-IR molecular sensing under realistic, lossy environments. Mid-IR vibrational spectroscopy provides molecule-specific fingerprints, yet nanophotonic implementations are often challenged by system complexity and by severe damping in aqueous backgrounds. Dielectric metasurfaces mitigate the ohmic loss and local heating constraints of metallic resonators and can provide spectrally selective resonances suitable for image-based readout. However, their spatially extended near-fields can be strongly affected by environmental absorption, which may hinder operation in water. To overcome these constraints, a compact dielectric perfect-absorber metasurface is developed that combines C_4-symmetric qBICs with a dual-gradient architecture. In this approach, an in-plane geometric perturbation and a global scaling parameter are used to control radiative loss and resonance wavelength. As a result, distinct coupling regimes can be programmed within a single metasurface while maintaining high absorbance (above 0.8) across the targeted parameter range. The platform is demonstrated for PMMA sensing in air, showing an absorbance-envelope modulation of $\sim 20\%$ under arbitrary polarization states. Furthermore, a sensing configuration based on a residual thin-water film of approximately $700\,\mathrm{nm}$ is introduced, which preserves qBIC resonances (absorbance ~ 0.5) near a prominent water absorption band and enables measurable molecular signatures under a water background with absorbance-envelope modulation exceeding 30%. These results support a practical route toward dielectric metasurface-based mid-IR sensing in environments relevant to biological and aqueous systems, while maintaining a compact and illumination-tolerant system.

In summary, this thesis discusses qBIC metasurfaces from mechanism-level understanding to device-level strategies that improve tunability, linearity, polarization robustness, and environmental compatibility. The permittivity-asymmetric and restored-BIC concepts introduce an additional handle to encode environmental changes into radiative coupling, enabling more reliable single-wavelength sensing. The C_4-symmetric qBIC platform relaxes polarization constraints and improves practical robustness. The dual-gradient perfect-absorber architecture further extends polarization-independent qBIC metasurfaces to compact mid-IR sensing schemes that remain functional under strongly absorptive backgrounds. Together, these developments contribute to bridging high-Q nanophotonic con-

cepts with more practical metasurface systems, reducing system requirements while expanding functionality for sensing and related light–matter interaction applications.

1

Introduction

Our understanding of light has undergone several conceptual shifts, evolving from classical wave and particle pictures to a unified electromagnetic and quantum description that forms the foundation of modern optics.[1–5] Alongside the evolving understanding of light, various methods of manipulating light have emerged. Classical approaches such as prisms, lenses, and diffraction gratings offered the first means of steering and dispersing light.[6] In the late 20th century, photonic crystals provided a route to control light at the wavelength scale by exploiting periodic structures and photonic band gaps.[7] More recently, the concept of metasurfaces, planar arrays of subwavelength resonators, has revolutionized optical engineering.[8,9] These ultrathin structures enable unprecedented control of phase, amplitude, and polarization within a compact footprint.[10,11]

While metasurfaces provide powerful tools for light manipulation, a central challenge remains: how to enhance light–matter interactions.[12] This problem is closely tied to resonances. Resonances amplify the interaction between light and nanostructures, but their effectiveness strongly depends on the quality factor (Q). A high-Q resonance sustains energy for a long duration, leading to sharper spectral features and stronger local fields, which are particularly beneficial for sensing[13–16], nonlinear optics[17–19], and enabling the exploration of material properties such as excitonic resonances, photon–polariton interactions, and other light–matter coupling effects.[20–23] Conventional resonant nanostructures,

such as those based on Mie scattering, are fundamentally limited by radiation losses.[24]

To overcome these limitations, the concept of bound states in the continuum (BIC), originally formulated in quantum mechanics, has been translated to photonic structures.[25–31] A BIC is a non-radiating eigenmode embedded in the radiation continuum; it arises either by symmetry protection or by destructive interference between distinct radiation channels, and consequently exhibits an ideally infinite quality factor.[32] Such perfectly bound states, however, have vanishing external coupling and cannot be excited from the far field. In practice, one deliberately relaxes the BIC condition by introducing controlled perturbations in the unit cell, such as breaking the relevant symmetry or folding the Brillouin zone, which opens a weak radiation channel.[32–34] The resulting quasi-BIC (qBIC) retains the strong field confinement of a BIC while acquiring a finite, tunable radiative linewidth. This framework affords continuous control over resonance linewidth and field enhancement, enabling flexible resonance engineering for enhanced light-matter interactions. In this thesis, we systematically investigate the design, implementation, and application of qBIC metasurfaces.

Chapter 2 provides several complementary perspectives for understanding the concept of BIC. First, drawing an analogy to quantum mechanics, a BIC can be regarded as a bound-state wavefunction confined within an infinitely deep potential well, vanishing outside the well despite being energetically embedded in the continuum. This picture offers an intuitive interpretation of the non-radiating nature of BICs. Second, from the viewpoint of electromagnetic wave theory, one can derive the scaling relation between the resonance quality factor Q and the asymmetry parameter, showing that Q decreases quadratically with increasing structural asymmetry. This framework highlights how small perturbations transform an ideal BIC into a qBIC with controllable radiation losses. Third, employing temporal coupled-mode theory (TCMT), the resonance can be rigorously described in terms of radiative and intrinsic loss channels, providing a quantitative model for evaluating and predicting the quality factor. Taken together, these three perspectives, quantum analogy, electromagnetic description, and TCMT, establish an intuitive theoretical foundation for symmetry-protected BIC, which will serve as the basis for the subsequent chapters of this thesis.

Chapter 3 details the numerical simulation workflow and the nanofabrication procedures used throughout this thesis, thereby laying the technical groundwork

for the subsequent experimental studies. On the simulation side, we employ CST Studio Suite in the frequency domain with unit-cell (Floquet) boundary conditions to model infinite periodic arrays at normal incidence. Material dispersion is implemented via tabulated dielectric functions imported from spectroscopic ellipsometry. Adaptive mesh refinement and stringent convergence criteria are used to ensure reproducibility of spectral features. On the fabrication side, we use electron-beam/thermal evaporation for material deposition, electron-beam lithography (e-line) for patterning and reactive ion etching (RIE) for pattern transfer, and standard lift-off processes.

Chapter 4 investigates qBIC metasurfaces in which radiative coupling is engineered not only by geometric symmetry breaking but also by the permittivity landscape surrounding the resonators. In widely used geometry-asymmetric qBICs (g-qBICs), the radiation leakage is largely predetermined once the structure is fabricated; consequently, refractive-index (RI) changes are most often read out as a predominantly horizontal spectral shift, with limited reshaping of the resonance modulation. To introduce an additional and tunable handle, this chapter develops a permittivity-asymmetric qBIC approach (ε-qBIC), where variations of the ambient RI translate into an effective asymmetry parameter. We use poly(methyl methacrylate) (PMMA) as a representative dielectric overlay in simulations and experiments. This resonance modulation upon refractive index shows both in resonance wavelength shift and strength modulation results in a more linear response for single-wavelength readout compared with g-qBIC implementations, while preserving high sensitivity. Moreover, numerical results suggest that an appropriately engineered permittivity asymmetry can counterbalance a predefined geometric asymmetry and drive the system towards an ultra-high-Q state approaching to the symmetry-protected BIC, with simulated Q values exceeding 10^7.

Chapter 5 addresses the practical challenge that many qBIC metasurfaces require a well-defined input polarization for efficient excitation. To remove this constraint, we adopt C_4-symmetric unit cells that support resonances accessible under arbitrary linear polarization states, thereby simplifying illumination conditions and improving the usable fraction of incident light. The chapter proposes and experimentally realizes a silicon metasurface comprising four square resonators per unit cell, where the radiative loss of qBIC is tuned via the edge-length difference between the squares. The demonstrated devices achieve a compromise between linewidth and resonance modulation, with an

experimental Q of about 100 and a modulation depth around 50%. Compared to earlier polarization-independent designs that often fall into the extremes of either high-Q but weak contrast or strong contrast but low-Q, the presented architecture yields a distinct and robust spectral signature that remains stable across polarization angles, supporting straightforward integration into compact optical systems.

Chapter 6 builds on polarization-independent qBICs and combines them with spatially modulated metasurface architectures to realize compact mid-infrared (mid-IR) molecular polarization-independent sensing under lossy conditions. While mid-IR spectroscopy offers chemically specific vibrational fingerprints, practical nanophotonic implementations are frequently hindered by instrumental complexity and pronounced attenuation in aqueous environments. Dielectric metasurfaces avoid ohmic heating and can provide spectrally selective resonances suitable for image-based, spectrometer-free detection; however, extended near-fields can also increase susceptibility to environmental absorption, particularly in water. To mitigate this limitation, this chapter develops a dielectric absorber metasurface that integrates C_4-symmetric qBICs with a dual-gradient design. By combining an in-plane perturbation with global scaling, radiative loss and resonance wavelength can be adjusted with a high level of independence, enabling multiple coupling regimes within a single sample while sustaining high absorbance (around 0.8) over the targeted wavenumber range. We demonstrate PMMA sensing in air with an absorbance-envelope modulation of approximately 20% under arbitrary polarization. Furthermore, we introduce an operating configuration that retains a residual thin-water film of roughly 700 nm, which preserves qBIC features (absorbance ~ 0.5) near a strong water absorption band and enables measurable molecular signatures under a water background, with absorbance-envelope modulation exceeding 30%.

Overall, this thesis connects qBIC fundamentals with device-oriented design rules that enhance tunability, improve the linearity of readout, relax polarization requirements, and extend operation into strongly absorbing environments. The ε-qBIC translate environmental changes into radiative coupling variations, which supports more reliable single-wavelength sensing. The permittivity restored BIC concept provides an additional degree of freedom to design extreme high-Q photonic devices. The C_4-symmetric platform removes polarization constraints and increases practical stability, while the dual-gradient architecture expands polarization-independent qBIC metasurfaces to compact mid-IR sensing schemes

that remain functional under absorption background. Together, these advances help bridge high-Q nanophotonic principles with metasurface implementations that better match the constraints of realistic sensing and light–matter interaction applications.

2

Fundamentals

In recent years, optical BICs have become an important focus of nanophotonics research. By supporting resonant modes with extremely high quality factors, BICs provide a platform for strongly enhanced light–matter interactions, which is advantageous for applications including optical sensing, nonlinear optics, and the study of material properties. To build a comprehensive understanding of BIC, this chapter discusses the concept from several perspectives. We first revisit the origin of the term BIC in the context of quantum mechanics, where it was introduced to describe localized states embedded in a continuum of radiation modes. We then relate the concept to classical electrodynamics, where BICs appear as non-radiating solutions of the wave equation despite lying in the radiation continuum. Since experimental implementations typically involve qBICs with finite radiative leakage, we further employ the framework of temporal coupled-mode theory to capture their intrinsic and radiative loss channels in a practical setting.

2.1 Confinement of waves

The confinement of waves, either partial or complete, is a common phenomenon in both natural systems and wave-based technologies. Typical examples include electrons localized in atoms and molecules, light guided in optical fibers, modes

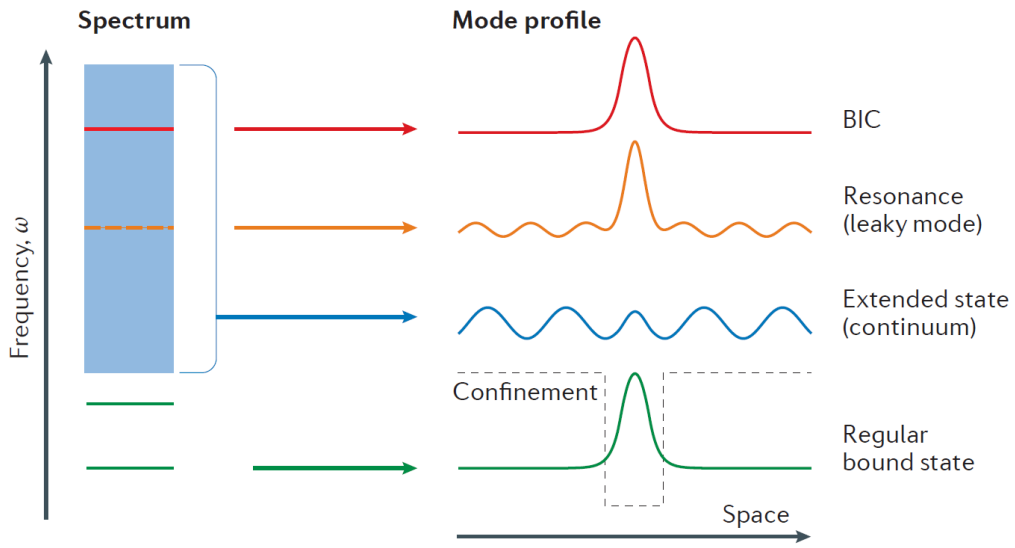

Figure 2.1: Illustration of a BIC. In an open system, the frequency spectrum consists of a continuum or several continua of spatially extended states (blue) and discrete levels of bound states (green) that carry no outgoing flux. The spatial localization of the bound states is a consequence of a confining structure or potential (black dashed line). States inside the continuous spectrum typically couple to the extended waves and radiate, becoming leaky resonances (orange). BICs (red) are special states that lie inside the continuum but remain localized with no radiation. Adapted from[25].

located below the light line, and the partial trapping of acoustic waves in musical instruments. The set of allowed oscillation frequencies is generally referred to as the wave spectrum[25].

In an open system, whether a wave can form a perfectly confined mode, a bound state, can often be judged by its frequency. If the frequency lies outside the continuum spanned by propagating waves, the state is bounded, as there is no channel for radiation. Conversely, when the frequency falls within the continuum, the state normally appears as a resonance that inevitably couples to radiation and leaks energy to infinity. However, there also exist modes that reside within the continuum yet remain perfectly confined without radiation. These are referred to as bound states in the continuum, which are localized modes that do not couple to the radiative continuum.

Figure 2.1 illustrates a schematic understanding of different types of modes in an open system. When considering a simple wave confined by a potential well (black dashed line), the solutions of the Schrödinger equation yield discrete energy levels represented by localized wavefunctions. These bound states are restricted to the vicinity of the potential well and cannot propagate to the far field. Outside the well, the spectrum forms a continuum of extended states

whose energies exceed the confining potential, allowing them to radiate away from the localized region, as indicated by the orange resonances in the figure.

Remarkably, by carefully tuning system parameters, it is possible to create a state that resides within the continuum but remains localized, as if the potential were infinitely deep. In this case, the wavefunction exhibits finite amplitude only near the confining region while vanishing outside. Such a state is referred to as a bound state in the continuum, shown in red in Figure 2.1.

The concept of BICs was first introduced in 1929 by von Neumann and Wigner[35]. As a demonstration, they mathematically constructed a three-dimensional potential that extends to infinity and oscillates in a specifically designed manner, such that it supports an electronic bound state embedded within the continuum.

Their idea was to construct special wavefunctions that, despite having energies embedded in the continuum, remain spatially localized. For a target wavefunction Ψ with positive energy $E > 0$, the corresponding potential V can be obtained by rearranging the Schrödinger equation (in reduced units):

$$-\frac{1}{2}\nabla^2\Psi + V\Psi = E\Psi \tag{2.1}$$

which directly yields

$$V = E + \frac{\nabla^2\Psi}{2\Psi} \tag{2.2}$$

In this construction, both Ψ and E must be chosen such that the resulting potential V vanishes at infinity, thereby ensuring compatibility with the continuum and remaining well defined throughout space. In this limit, the problem effectively reduces to the case of an infinitely deep potential well, where the wavefunction Ψ must vanish at the boundary due to the continuity condition. As a result, the wavefunction has finite values only inside the well, meaning that the probability of finding the electron is strictly confined to the interior and zero outside. By appropriately tuning the parameters, such a configuration realizes a BIC. This approach demonstrates that bound states can exist within the radiation continuum by carefully engineering the form of the potential, providing the first mathematical foundation for the concept of BICs.

2.2 Electromagnetic description

While the original concept of BICs was formulated in the framework of quantum mechanics, the idea was later extended to photonics and classical wave systems. In this context, Maxwell's equations replace the Schrödinger equation as the governing framework, and BICs correspond to non-radiating electromagnetic modes. These modes are localized in space but exist within the continuum of radiation states, exhibiting infinite lifetimes in the ideal case. From the photonics perspective, BICs arise from destructive interference or symmetry protection, which prevent coupling to outgoing radiation channels despite spectral overlap.

2.2.1 Analogy of the Helmholtz and Schrödinger equations

For general time-dependent electromagnetic fields, Maxwell's equations in differential form are[36]

$$\nabla \times \mathbf{E}(\mathbf{r},t) = -\frac{\partial \mathbf{B}(\mathbf{r},t)}{\partial t}, \tag{2.3}$$

$$\nabla \times \mathbf{H}(\mathbf{r},t) = \frac{\partial \mathbf{D}(\mathbf{r},t)}{\partial t} + \mathbf{J}(\mathbf{r},t), \tag{2.4}$$

$$\nabla \cdot \mathbf{D}(\mathbf{r},t) = \rho(\mathbf{r},t), \tag{2.5}$$

$$\nabla \cdot \mathbf{B}(\mathbf{r},t) = 0. \tag{2.6}$$

Here, $\mathbf{E}$ and $\mathbf{H}$ denote the electric and magnetic field intensities, $\mathbf{D}$ and $\mathbf{B}$ are the electric and magnetic flux densities, $\mathbf{J}$ is the electric current density, and ρ is the free charge density. In linear media, the constitutive relations read as follows

$$\mathbf{D}(\mathbf{r},t) = \varepsilon(\mathbf{r})\,\mathbf{E}(\mathbf{r},t), \tag{2.7}$$

$$\mathbf{B}(\mathbf{r},t) = \mu(\mathbf{r})\,\mathbf{H}(\mathbf{r},t). \tag{2.8}$$

where $\varepsilon(\mathbf{r}) = \varepsilon_0\varepsilon_r(\mathbf{r})$ and $\mu(\mathbf{r}) = \mu_0\mu_r(\mathbf{r})$ may vary spatially.

These material equations are central to describe light–matter interactions, as they define how the electric permittivity ε and magnetic permeability μ govern the propagation of electromagnetic waves in a medium. By spatially tailoring

the material distribution on subwavelength scales, metasurfaces provide access to engineered electromagnetic responses, including anisotropy, nonlinearity, and tailored dispersion. Such control enables forms of light–matter interaction that go beyond the limitations of naturally occurring materials.

In a medium without charges and currents ($\mathbf{J} = \mathbf{0}$, $\rho = 0$), the solution of Maxwell's equations can be expressed in terms of time-harmonic plane waves. For the electric field we write

$$\mathbf{E}(\mathbf{r}, t) = \mathrm{Re}\{\mathbf{E}(\mathbf{r})\, e^{-i\omega t}\}, \tag{2.9}$$

where $\mathbf{E}(\mathbf{r})$ denotes the complex field amplitude.

Substituting (2.9) into (2.3)–(2.6) together with the constitutive relations (2.7) yields the frequency-domain curl equations. Taking the curl of Faraday's law and eliminating $\mathbf{H}$ leads to the vector wave equation (curl–curl form) for the electric field:

$$\nabla \times \big[\mu^{-1}(\mathbf{r})\, \nabla \times \mathbf{E}(\mathbf{r})\big] = \omega^2\, \varepsilon(\mathbf{r})\, \mathbf{E}(\mathbf{r}). \tag{2.10}$$

In homogeneous and isotropic regions, where ε and μ are constants, (2.10) reduces to the vector Helmholtz equation

$$\nabla^2 \mathbf{E}(\mathbf{r}) + k^2\, \mathbf{E}(\mathbf{r}) = \mathbf{0}, \qquad k^2 = \omega^2 \varepsilon \mu, \tag{2.11}$$

For periodic photonic structures, fields satisfy Bloch boundary conditions

$$\mathbf{E}(\mathbf{r} + \mathbf{R}) = \mathbf{E}(\mathbf{r})\, e^{i\mathbf{k}\cdot\mathbf{R}}, \tag{2.12}$$

BIC construction Starting from Equation 2.1, the time-independent Schrödinger equation can be rewritten as (in reduced unit)

$$-\frac{1}{2}\nabla^2 \psi(\mathbf{r}) + \big[V(\mathbf{r}) - E\big]\psi(\mathbf{r}) = 0, \tag{2.13}$$

where $V(\mathbf{r})$ denotes the potential and E is the eigenenergy of the electron.

Comparing (2.13) with the scalar Helmholtz equation,

$$\nabla^2 \psi(\mathbf{r}) + k^2(\mathbf{r})\, \psi(\mathbf{r}) = 0, \tag{2.14}$$

where ψ denotes a representative field component and $k = n\omega/c$ with $n = \sqrt{\varepsilon\mu/(\varepsilon_0\mu_0)}$, reveals a clear structural similarity: both equations are second-order elliptic eigenvalue problems in space, where the spatially varying term plays the role of an effective potential. In the quantum case, the potential $V(\mathbf{r})$ defines bound or extended electronic states, while in electromagnetism the effective term $k^2(\mathbf{r}) = \omega^2\varepsilon(\mathbf{r})\mu(\mathbf{r})$ is governed by the spatial distribution of the permittivity $\varepsilon(\mathbf{r})$ and permeability $\mu(\mathbf{r})$. This analogy shows that tuning $\varepsilon(\mathbf{r})$ in photonic systems is formally equivalent to engineering $V(\mathbf{r})$ in quantum systems: both shape the allowed modes, their confinement, and their coupling to continuum.

This correspondence highlights a deep mathematical isomorphism between electron and photon wave phenomena. Just as tailoring the potential landscape $V(\mathbf{r})$ in solid-state physics produces discrete energy levels, band structures, and localized states, spatial modulation of the refractive index $n(\mathbf{r})$ (with $n^2 = \varepsilon\mu/(\varepsilon_0\mu_0)$) yields photonic band structures, energy gaps, and confined modes. For instance, periodic variations in $n(\mathbf{r})$ give rise to photonic band gaps that forbid light propagation at specific frequency ranges, directly mirroring the emergence of electronic band gaps in crystals due to a periodic potential $U(\mathbf{r})$. Concepts such as Bloch waves, Brillouin zones, and band gaps thus have natural analogs in photonic systems.

In this context, BICs can be understood as the optical counterpart of quantum bound states embedded within a continuum. While the Schrödinger framework demonstrates that such states can exist through carefully engineered potentials, the Helmholtz framework shows that non-radiating optical eigenmodes may exist within the radiation continuum through symmetry protection or destructive interference.

2.2.2 Coupling to the continuum

We analyze the transmission of a periodic photonic structure with isotropic dielectric permittivity $\varepsilon(\omega, \mathbf{r})$, embedded in a homogeneous background medium of unit permittivity. A normally incident x-polarized plane wave with amplitude E_0 excites the structure, $\mathbf{E}_{\text{inc}} = \mathbf{e}_x E_0 \exp(ikz)$, producing a total field $\mathbf{E}(\mathbf{r}) = \mathbf{E}_{\text{inc}}(\mathbf{r}) + \mathbf{E}_{\text{sc}}(\mathbf{r})$, where $\mathbf{E}_{\text{inc}}$ is the incident field and $\mathbf{E}_{\text{sc}}$ is the scattered field.

The scattered field satisfies the Lippmann–Schwinger equation[37,38],

$$\mathbf{E}_{\text{sc}}(\mathbf{r}) = -k^2 \int d\mathbf{r}' \, [\varepsilon(k, \mathbf{r}') - 1] \, \hat{G}_0(k; \mathbf{r}, \mathbf{r}') \cdot \big[\mathbf{E}_{\text{inc}}(k, \mathbf{r}') + \mathbf{E}_{\text{sc}}(\mathbf{r}')\big], \tag{2.15}$$

where $k = \omega/c$, and $\hat{G}_0(k; \mathbf{r}, \mathbf{r}')$ is the free-space dyadic Green's function. Here, $\mathbf{r}$ is the *observation point* at which the scattered field is evaluated, while $\mathbf{r}'$ is an *integration variable* that runs over all positions inside the inhomogeneous region of the photonic structure. The term $\varepsilon(k, \mathbf{r}') - 1$ represents the local permittivity contrast relative to the background and acts as the effective source of scattering.

The scattered field inside the integrand can itself be expressed using the dyadic Green's function $\hat{G}$ of the full photonic structure,

$$\mathbf{E}_{\text{sc}}(\mathbf{r}') = -k^2 \int d\mathbf{r}'' \, [\varepsilon(k, \mathbf{r}'') - 1] \, \hat{G}(k; \mathbf{r}', \mathbf{r}'') \cdot \mathbf{E}_{\text{inc}}(k, \mathbf{r}''), \tag{2.16}$$

where $\mathbf{r}'$ now plays the role of an observation point, and $\mathbf{r}''$ is a second integration variable corresponding to another source position inside the scattering volume.

In essence, Eqs. (2.15)–(2.16) state that the scattered field at any point is the coherent superposition of radiation emitted by all material inhomogeneities. Each inhomogeneity acts like a secondary source, excited by the incident wave and re-radiating via the Green's function. The total scattered field results from the sum of all such contributions.

We focus on periodic photonic structures arranged as a rectangular array in the x–y plane. In the following, we restrict our analysis to the case where the lattice periods in both directions are below the diffraction limit, so that only the zeroth diffraction order contributes to the far-field response. By introducing a perturbation operator into the free-space Green's function $\hat{G}_0$, the transmission coefficient can be derived in closed form. The resulting expression for $t(k)$ is given by

$$t(k) = 1 + \Delta t(k) + \frac{ik}{2S_0}[\varepsilon(k) - 1]V_0 - \frac{ik^2}{4S_0} \sum_j \frac{\Big(\int d\mathbf{r}' [\varepsilon(k, \mathbf{r}') - 1] E_{j,x}(\mathbf{r}') e^{-ikz'} \Big)}{k - k_j} \times \Big(\int d\mathbf{r}'' [\varepsilon(k, \mathbf{r}'') - 1] E_{j,x}(\mathbf{r}'') e^{ikz''} \Big), \tag{2.17}$$

where V_0 denotes the volume of a single meta-atom and S_0 is the unit cell area. The correction term $\Delta t(k)$, which accounts for higher-order scattering processes, is expressed as

$$\Delta t(k) = -\frac{ik^3}{2S_0} \int d\mathbf{r}' \left[\varepsilon(k,\mathbf{r}') - 1\right] e^{-ikz'} \int d\mathbf{r}'' \left[\varepsilon(k,\mathbf{r}'') - 1\right] e^{ikz''} \left[\Delta\hat{G}(k;\mathbf{r}',\mathbf{r}'')\right]_{xx}. \tag{2.18}$$

Based on Eqs. (2.17) and (2.18), it is convenient to introduce the concept of the *coupling amplitude*. The coupling amplitude incorporates both the symmetry of the mode profile and permittivity profile, and is defined as

$$D_{x,y}(k) = -\frac{k}{2\sqrt{S_0}} \int \underbrace{E_{x,y}(\mathbf{r}')}_{\text{Mode symmetry}} \cdot \underbrace{\left[\varepsilon(k,\mathbf{r}') - 1\right]}_{\substack{\text{Permittivity} \\ \text{symmetry}}} \cdot \underbrace{e^{ikz'}}_{\text{Incidence angle}} d\mathbf{r}'. \tag{2.19}$$

Here, $E_{x,y}(\mathbf{r}')$ denotes the x- or y-polarized field component of the guided resonance mode, $\varepsilon(k,\mathbf{r}') - 1$ is the local permittivity contrast, and S_0 is the unit cell area. The term $e^{ikz'}$ accounts for the phase accumulation due to the incidence geometry.

This definition provides a compact measure of how efficiently an external plane wave couples into a specific mode of the photonic structure, thereby linking the microscopic material modulation with the macroscopic transmission response.

For the case of normal incidence, when the permittivity distribution of the unit cell is symmetric, the coupling behavior is primarily determined by the symmetry of the mode. In particular, if the excited mode is odd with respect to the up–down mirror symmetry along the z direction, the electric field amplitudes in the upper and lower halves of the structure have opposite signs and therefore cancel each other. Furthermore, in the x–y plane, modes with C_2 symmetry exhibit an additional cancellation: every field contribution $E_{x,y}(\mathbf{r}_1)$ is exactly compensated by its counterpart at the symmetry-related position, $E_{x,y}(-\mathbf{r}_1) = -E_{x,y}(\mathbf{r}_1)$. As a result of this symmetry mismatch, the coupling coefficient defined in Eq. (2.19) vanishes for all C_2-symmetric modes. Consequently, such modes cannot couple to normally incident plane waves at the Γ point and therefore manifest as BICs. These BICs remain perfectly localized within the periodic structure in the out-of-plane direction, as they do not radiate into the far field.

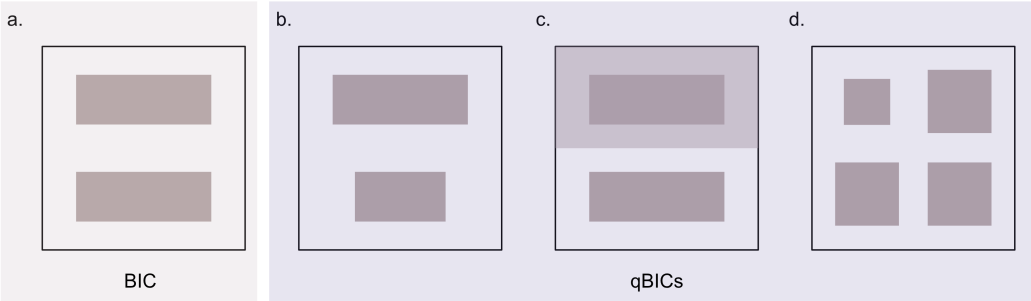

Figure 2.2: Ways of creating qBIC from ideal BIC. The schematic illustrates how a BIC mode from a unit cell can be transformed into a qBIC by introducing different types of perturbations. **a.** Ideal BIC mode with two identical resonators of equal length. **b.** qBIC mode generated by shorting one length from the two resonators, making them unequal. **c.** qBIC mode formed when the two resonators have equal length but are embedded in environments with different permittivities. **d.** Polarization-independent qBIC mode created in a unit cell containing four square resonators, where a slight perturbation is introduced by altering the size of one resonator relative to the other three.

Design routes to qBICs Since BICs are idealized mathematical solutions, they cannot be directly excited or observed in experiments. For practical applications, it is therefore necessary to introduce a controlled perturbation into the BIC-supporting structure. This perturbation breaks the perfect confinement and transforms the BIC into a qBIC, which possesses a very large but finite quality factor. In this regime, the mode acquires weak radiative coupling, making it observable in the far field. The concept of qBICs thus bridges the gap between the mathematical idealization and experimental realizability, enabling the exploitation of high-Q resonances for practical applications.

In Figure 2.2(a), a classical symmetry-protected BIC is illustrated. Within one unit cell, the two resonators are identical, and the BIC mode generates dipole moments in the x–y plane that are equal in magnitude but opposite in direction. Under normal incidence and a homogeneous background, this situation corresponds to the mode symmetry term in Equation 2.19. In this case, the integral evaluates to zero, resulting in vanishing far-field coupling strength. As a consequence, no radiation appears in the far-field spectrum.

In practice, several strategies can be employed to introduce perturbations and thereby transform a BIC into a qBIC. A first common approach is to break the geometric symmetry of the structure. For example, in Figure 2.2(b), the length of one resonator within the unit cell is reduced. As a result, the dipole moments in the x–y plane remain anti-parallel but acquire unequal magnitudes, leading to a nonzero value of the integral in Equation 2.19. The coupling strength

thus becomes finite, giving rise to observable radiation in the far-field spectrum, characteristic of a qBIC. It is called geometry-breaking qBIC (**g-qBIC**).

Alternatively, perturbations can arise from material asymmetry, such as introducing different refractive indices in the surrounding environment, effectively breaking the symmetry within the unit cell. A similar effect occurs in the configuration shown in Figure 2.2(c), where one of the resonators in the unit cell is embedded in a material with a different permittivity. In this case, the permittivity symmetry term in Equation 2.19 is broken, again leading to a nonzero integral and consequently a finite coupling strength. This perturbation likewise transforms the ideal BIC into a qBIC. It is called permittivity-breaking qBIC (**ε-qBIC**).

The first two perturbation strategies, illustrated in Figure 2.2(b) and Figure 2.2(c), generate qBICs that can only be excited by x-polarized incident waves, since the induced asymmetry modifies the x-polarized component of the coupling amplitude in Equation 2.19. In order to achieve a polarization-independent qBIC, a different type of perturbation is required. As shown in Figure 2.2(d), this can be realized in a unit cell consisting of four identical square resonators placed at the centers of the four quadrants. By introducing a slight perturbation to the size of one resonator relative to the other three, the electric field distribution no longer possesses the symmetry required for mutual cancellation, and therefore the integral in Equation 2.19 becomes nonzero for both x- and y-polarized incidence. As a result, a **polarization-independent qBIC** is formed.

It is important to emphasize that, from the viewpoint of structural symmetry, both the geometric-asymmetry and permittivity-asymmetry approaches (Figure 2.2(b) and Figure 2.2(c)) realize qBICs by breaking the in-plane twofold rotational symmetry (C_2) of the unit cell. In these cases, the balance between the two resonators is disrupted, so that the mode symmetry term in Equation 2.19 no longer cancels out.

Another route is engineering symmetry-protected BIC by Brillouin zone folding (BZF), where a bound state outside the light cone is folded into the continuum through the introduction of periodic modulation, thereby giving rise to a qBIC[34]. Specifically, the third approach (Figure 2.2(d)) produces a polarization-independent qBIC. When a slight perturbation is introduced by modifying the size of one resonator, the global C_2 symmetry of the unit cell remains preserved. Therefore, it is not appropriate to interpret this case as a simple breaking of

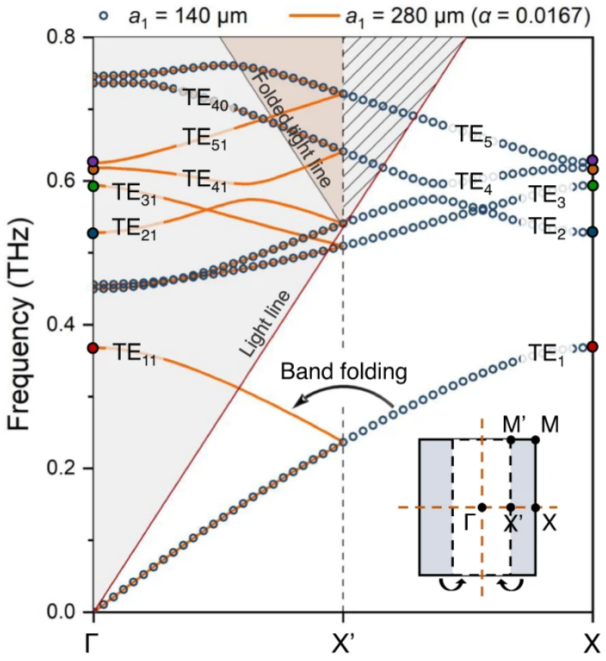

Figure 2.3: Engineering symmetry-protected BICs by Brillouin zone folding. Calculated transverse electric (TE) band structures of unperturbed (blue circles) and perturbed (orange lines) photonic crystals are shown. In the unperturbed case, guided modes located at the X point are folded back to the Γ point once a periodic perturbation is introduced, thereby enabling their coupling under normal incidence. The inset illustrates the Brillouin zone folding process, where the original first Brillouin zone (solid box) shrinks to half its size after the perturbation, causing the modes from the zone boundary to reappear at the Γ point. Adapted from[34]

geometric symmetry. Instead, the mechanism is better understood from the perspective of BZF: the perturbation doubles the periodicity of the structure, which in turn folds a high-symmetry bound mode from the edge of the Brillouin zone back to the Γ point, so that it can be excited from normal incident (Figure 2.3). And due to the perturbation within the unit cell, the electric field distribution no longer exhibits the mutual cancellation required for an ideal symmetry-protected BIC. As a result, the corresponding coupling amplitude in Equation 2.19 becomes nonzero.

In summary, while the first two perturbation strategies create qBICs by explicitly breaking structural C_2 symmetry, the third approach relies on Brillouin-zone folding to engineer the symmetry properties of the mode itself, show the diversity of mechanisms through which qBICs can be realized in photonic systems.

2.2.3 Resonance characteristics of qBICs

A resonant state can be regarded as an eigenmode of a closed resonator that interacts with the radiation continuum. To simplify the discussion, we consider a periodic photonic structure with a constant, real-valued permittivity $\varepsilon(\mathbf{r})$, embedded in an isotropic environment. The same approach can be readily extended to more general scenarios involving dispersive materials with losses or the presence of a substrate. Furthermore, we restrict our analysis to the sub-diffraction regime, where the wavelength of interest is larger than both lattice periods. Based on perturbation theory[37,39]:

$$\frac{\gamma_{\text{rad}}}{c} = |D_x|^2 + |D_y|^2. \tag{2.20}$$

The coupling of the dark mode to the radiation continuum can be characterized by the coupling amplitudes D_x and D_y, corresponding to x- and y-polarized incident light, respectively. These amplitudes quantify the interaction between the qBIC and the zeroth-order diffraction channels, i.e., reflection and transmission normal to the substrate plane. Here, D_x and D_y are from Equation 2.19.

By expanding the exponential factor $e^{ik_0 z'}$ in the definition of the coupling amplitude (Equation 2.19) into a Taylor series, the expressions for D_x and D_y can be simplified into a multipole form:

$$D_x = -\frac{k_0}{\sqrt{2S_0}}\left[p_x - \frac{m_y}{c} + \frac{ik_0}{6}Q_{xz}\right], \tag{2.21}$$

$$D_y = -\frac{k_0}{\sqrt{2S_0}}\left[p_y + \frac{m_x}{c} + \frac{ik_0}{6}Q_{yz}\right], \tag{2.22}$$

where $\mathbf{p}$, $\mathbf{m}$, and $\mathbf{Q}$ denote the electric dipole, magnetic dipole, and electric quadrupole moments, respectively, following the irreducible representations defined in reference[40].

When one contribution dominates the coupling process, the remaining multipole terms can be neglected. For example, in the case of the symmetry-broken structure shown in Figure 2.2(b), the radiation is primarily governed by the electric dipole response. In this situation, the effective dipole moment can be approximated by p_x, and the coupling amplitude reduces to

$$\frac{\gamma_{\text{rad}}}{c} \approx \frac{k_0^2}{2S_0}|p_x|^2, \tag{2.23}$$

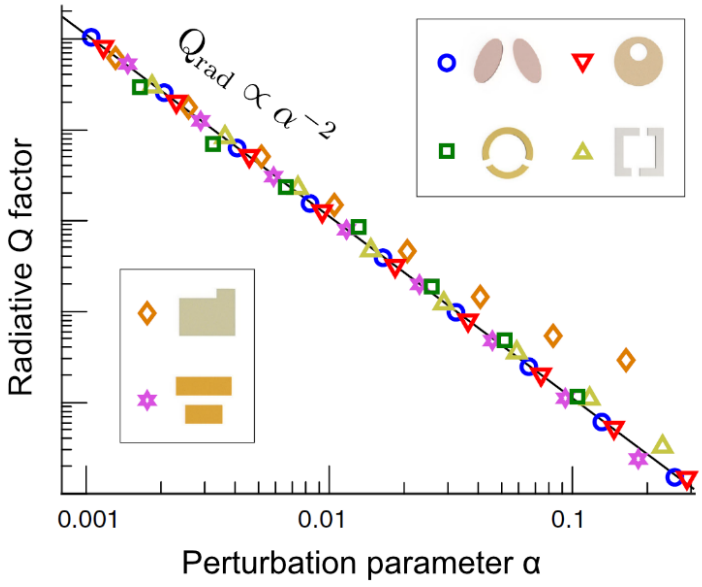

Figure 2.4: Scaling of radiative Q factors with perturbation parameter. The radiative quality factors of all depicted unit-cell designs follow the predicted α^{-2} dependence. Graph adapted from[37].

Here, γ_{rad} denotes the radiative loss rate, which is directly related to the radiative quality factor Q. The magnitude of the effective moment depends on the perturbation introduced into the structure. Using $Q_{\mathrm{rad}} = \omega_0/\gamma_{\mathrm{rad}}$ and introducing a perturbation parameter α, one can establish the relationship between the radiative quality factor of the qBIC resonance and the structural perturbation applied in the unit cell during metasurface design:

$$Q_{\mathrm{rad}} \propto \frac{S_0}{2k_0}\alpha^{-2}, \tag{2.24}$$

Here, α denotes a small geometric perturbation, which is proportional to the effective dipole moment $p_{x,y}$ within the unit cell. The perturbation parameter can be defined in relative terms, for example as a fractional change in volume ΔV, cross-sectional area ΔS, length ΔL of the resonator, or $\Delta\varepsilon$ of the environment permittivity with respect to the unperturbed part. The quadratic dependence of the radiative Q factor on $1/\alpha^2$ represents a key feature of qBICs, establishing a direct correlation between the induced dipole moment of the qBIC resonance and the degree of asymmetry or perturbation. This scaling law not only provides a clear physical picture of how geometric perturbations control radiation leakage, but also offers a practical route to tune the radiative decay rate, constituting an efficient and versatile platform for engineering light–matter interactions with controllable quality factors.

The derivation above was illustrated using the case of geometric asymmetry (Figure 2.2(b), g-qBIC). However, the same mechanism applies to permittivity asymmetry (Figure 2.2(c), ε-qBIC). From the modal perspective, both perturbations modify the effective dipole moment within the unit cell and thus follow the same scaling relation.

In both cases, the perturbation modifies the integrand of the coupling amplitude in Equation 2.19, either by reshaping the modal field $E_{x,y}(\mathbf{r}')$ (geometry) or by changing the material term $[\varepsilon(\mathbf{r}') - 1]$ (environment). This imbalance produces a finite effective dipole moment (p_x or p_y) and hence a nonzero coupling amplitude $D_{x,y}$, which leads to radiation leakage of the qBIC. For small perturbations, the effective dipole scales linearly with the perturbation strength α, so that $\gamma_{\mathrm{rad}} \propto |D|^2 \propto \alpha^2$ and, consequently, $Q_{\mathrm{rad}} \propto \alpha^{-2}$.

The polarization-independent qBIC shown in Figure 2.2(d) involves four resonators within the unit cell, and its resonance originates from a different set of eigenmodes compared to the previous cases. Nevertheless, the radiation behavior is still governed by the dominant mode contribution, and through the same additive relation in Equation 2.21 and Equation 2.22, the effective moment again scales linearly with the perturbation strength. As a result, the radiative Q factor follows the same universal scaling law $Q_{\mathrm{rad}} \propto \alpha^{-2}$.

In summary, despite their different implementations, geometric asymmetry (g-qBIC), permittivity asymmetry (ε-qBIC), or polarization-independent configurations, the underlying mechanism is universal. In all cases, the perturbation introduces a finite effective multipole moment that couples the symmetry-protected BIC to the radiation continuum. The resulting radiative decay rate scales as $\gamma_{\mathrm{rad}} \propto \alpha^2$, leading to the characteristic inverse-square dependence of the radiative quality factor.

2.3 TCMT description

In the previous subsections, we approached the concept of BICs from different perspectives to establish an intuitive understanding. We now turn to the temporal coupled-mode theory framework. In practice, experimental results are typically obtained in the form of a series of far-field spectra, from which quality factors can be extracted. Verifying whether these Q factors follow the characteristic inverse-square dependence on the perturbation strength is crucial to identifying

BIC-derived resonances. TCMT offers an approach for fitting spectral line shapes and extracting Q values, thereby enabling a model-based interpretation of BICs and their perturbative evolution into qBICs. A more detailed derivation can be found in the references[41–43].

For a realistic optical cavity, the resonant mode inevitably experiences losses due to both intrinsic absorption and radiative leakage. The temporal evolution of the complex mode amplitude $a(t)$ can therefore be described by a first-order differential equation of the form

$$\frac{da}{dt} = i\omega_0 a - \gamma a, \tag{2.25}$$

where ω_0 is the resonance frequency of the cavity, and γ denotes the total decay rate of the mode. The decay rate can be further decomposed into intrinsic losses γ_{int} (e.g., absorption or material damping) and radiative losses γ_{rad} due to coupling to the continuum, such that $\gamma = \gamma_{\mathrm{int}} + \gamma_{\mathrm{rad}}$. Equation (2.25) thus captures both the oscillatory behavior of the cavity field at frequency ω_0 and its exponential decay in time caused by energy dissipation.

Next, we extend the model to account for the interaction of the cavity mode with the external radiation field through two ports, which directly corresponds to the physical scenario of a metasurface with one input and one output channel. The coupling to the external channels is described in terms of the incoming and outgoing wave amplitudes, denoted by the vectors

$$\mathbf{s}_{\pm} = \begin{pmatrix} s_{1\pm} \\ s_{2\pm} \end{pmatrix}, \tag{2.26}$$

where s_{i+} and s_{i-} represent the normalized amplitudes of the incoming and outgoing waves at the i-th port, respectively, such that $|s_{i\pm}|^2$ corresponds to the wave power.

The efficiency of amplitude (energy) transfer between the cavity mode and the ports is quantified by the coupling constants $\boldsymbol{\kappa}$ for the incoming waves and $\mathbf{d}$ for the outgoing waves,

$$\boldsymbol{\kappa} = \begin{pmatrix} \kappa_1 \\ \kappa_2 \end{pmatrix}, \quad \mathbf{d} = \begin{pmatrix} d_1 \\ d_2 \end{pmatrix}. \tag{2.27}$$

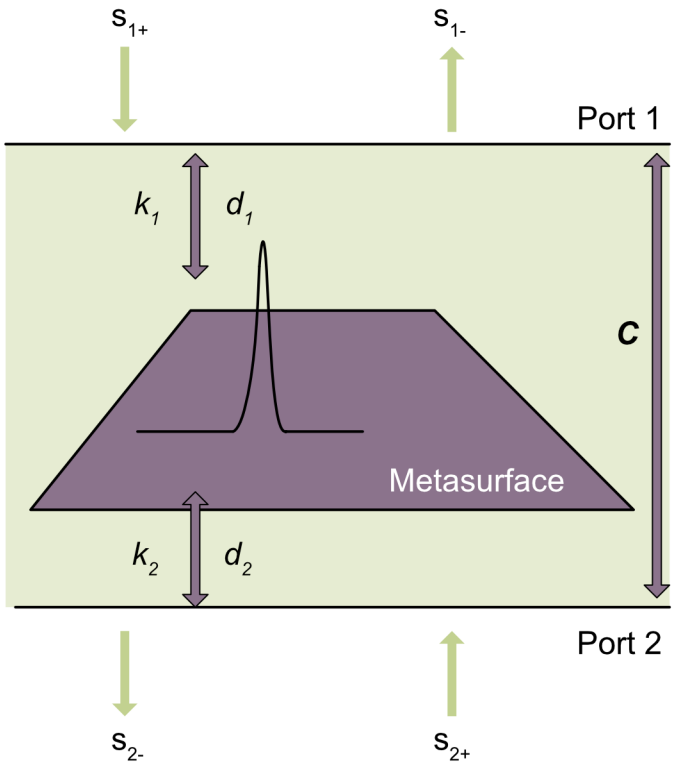

Figure 2.5: Sketch of a BIC metasurface in temporal coupled-mode theory. The system consists of two ports with incident and outgoing fields $\mathrm{s}_{\pm}$, a direct scattering matrix C, and far-field coupling matrices $\mathbf{K}$ and $\mathbf{d}$.

With these definitions, the temporal coupled-mode equation for the mode amplitude $a(t)$ can be generalized to include the external excitation:

$$\frac{da}{dt} = (i\omega_0 - \gamma)a + \boldsymbol{\kappa}^T \mathbf{s}_+. \tag{2.28}$$

Equation (2.28) thus accounts for both the intrinsic evolution of the mode and the driving by the incident waves through the input ports. The term $\boldsymbol{\kappa}^T \mathbf{s}_+$ is written in this form to emphasize its general applicability in more complex scenarios. In the present context, it should be interpreted as the multiplication of a row vector with a column vector, yielding a scalar quantity that describes the net excitation of the cavity mode by the incoming waves.

In addition to the resonant pathway, one must also account for direct, off-resonant scattering channels that contribute to the overall response of the system. This is particularly important when describing illumination with broadband sources, where not all spectral components coincide with the cavity resonance. Such a background contribution can be implemented through a direct scattering matrix $\mathbf{C}$, which is unitary (to ensure energy conservation) and constrained by

the mirror symmetry of the system. $\mathbf{C}$ is expressed as

$$\mathbf{C} = e^{i\phi} \begin{pmatrix} r_0 & it_0 \\ it_0 & r_0 \end{pmatrix}, \tag{2.29}$$

where ϕ, r_0, and t_0 are real parameters, subject to the condition $r_0^2 + t_0^2 = 1$.

Combining the resonant dynamics with the direct scattering channel, the complete set of temporal coupled-mode equations can be written as

$$\frac{da}{dt} = (i\omega_0 - \gamma)a + \boldsymbol{\kappa}^T \mathbf{s}_+, \tag{2.30}$$

$$\mathbf{s}_- = \mathbf{C}\mathbf{s}_+ + a\mathbf{d}, \tag{2.31}$$

Equations (2.30)–(2.31) constitute the standard TCMT formalism for describing resonant scattering in photonic systems.

To further reduce the number of free parameters in the TCMT model, several simplifying assumptions can be applied based on the symmetries of the system. We first consider the case where the cavity mode is initially excited with amplitude a, and the external input fields are switched off ($\mathbf{s}_+ = 0$). In this situation, the temporal dynamics of the stored energy $E \propto |a|^2$ can be expressed as

$$\frac{dE}{dt} = \frac{d|a|^2}{dt} = -2\gamma|a|^2 = -2(\gamma_{\text{int}} + \gamma_{\text{rad}})|a|^2, \tag{2.32}$$

where γ_{int} and γ_{rad} represent the intrinsic and radiative decay channels, respectively. The corresponding power losses can therefore be separated into

$$P_{\text{int}} = -2\gamma_{\text{int}}E, \quad P_{\text{rad}} = -2\gamma_{\text{rad}}E. \tag{2.33}$$

Since no incoming waves are present, the output reduces to $\mathbf{s}_- = a\mathbf{d}$, and the radiative loss must be emitted into the ports. This directly connects the coupling vector $\mathbf{d}$ to the radiative decay rate:

$$|\mathbf{d}|^2 = 2\gamma_{\text{rad}}. \tag{2.34}$$

By invoking time-reversal symmetry, one finds that the relation also holds for the excitation channel, leading to the identification

$$\mathbf{d} = \boldsymbol{\kappa} \tag{2.35}$$

For a system with two symmetric ports, the decay rate is equally distributed, yielding

$$|\kappa|^2 = \kappa_1^2 + \kappa_2^2 = 2\kappa_i^2 = 2\gamma_{\mathrm{rad}} \quad \Rightarrow \quad \kappa_i = \sqrt{\gamma_{\mathrm{rad}}}. \tag{2.36}$$

Finally, it is convenient to recast the TCMT formalism into a scattering-matrix description, where the outgoing fields are expressed in terms of the incoming ones via

$$\mathbf{s}_- = \mathbf{S}\mathbf{s}_+, \tag{2.37}$$

with S denoting the total scattering matrix of the system. Explicitly solving the coupled equations for a yields

$$\mathbf{s}_- = \left[\mathbf{C} + \frac{\boldsymbol{\kappa}\mathbf{d}^T}{i(\omega - \omega_0) + \gamma}\right]\mathbf{s}_+ = \mathbf{S}\mathbf{s}_+. \tag{2.38}$$

In our case, the metasurface is illuminated only from port 1, corresponding to $s_{2+} = 0$. The relation between the incoming and outgoing waves can therefore be expressed as

$$\begin{pmatrix} s_{1-} \\ s_{2-} \end{pmatrix} = \begin{pmatrix} s_{11} & s_{12} \\ s_{21} & s_{22} \end{pmatrix} \begin{pmatrix} s_{1+} \\ 0 \end{pmatrix} = \begin{pmatrix} s_{11}s_{1+} \\ s_{21}s_{1+} \end{pmatrix}. \tag{2.39}$$

From this relation, the reflection and transmission coefficients can be directly identified as

$$r = \frac{s_{1-}}{s_{1+}} = s_{11}, \qquad t = \frac{s_{2-}}{s_{1+}} = s_{21}. \tag{2.40}$$

Since the wave amplitudes are normalized such that $|s|^2$ represents the carried power, the reflectance R and transmittance T follow as

$$R = |r|^2, \qquad T = |t|^2. \tag{2.41}$$

By substituting Equation 2.29, Equation 2.35, and Equation 2.36 into Equation 2.38, we obtain the final expressions for the reflection and transmission coefficients, namely s_{11} and s_{21}, which are the central quantities of interest in our analysis.

$$s_{11} = r_0 e^{i\phi} + \frac{\gamma_{\mathrm{rad}}}{i(\omega - \omega_0) + \gamma_{\mathrm{rad}} + \gamma_{\mathrm{int}}}, \tag{2.42}$$

$$s_{21} = it_0 e^{i\phi} + \frac{\gamma_{\mathrm{rad}}}{i(\omega - \omega_0) + \gamma_{\mathrm{rad}} + \gamma_{\mathrm{int}}}, \tag{2.43}$$

If a mode has $\gamma_{\mathrm{rad}} = 0$, it implies that the mode does not exchange energy with the external ports. Consequently, both reflection and transmission vanish in the far field, i.e., the coefficients s_{11} and s_{21} in Eqs. (2.42)–(2.43) reduce to zero. This condition corresponds to the case of a BIC.

The quality factor Q characterizes the ability of a cavity to store electromagnetic energy and is defined as[44],

$$Q = \omega_0 \frac{E}{P_{\mathrm{loss}}}. \tag{2.44}$$

For a resonance with total decay rate γ, combined with Equation 2.33, this definition can be expressed as

$$Q = \frac{\omega_0}{2\gamma}, \tag{2.45}$$

which is equivalent to the well-known linewidth-based definition

$$Q = \frac{\omega_0}{\Delta\omega}, \tag{2.46}$$

where $\Delta\omega = 2\gamma$ denotes the full width at half maximum (FWHM) of a Lorentzian resonance.

Since multiple decay channels can contribute to the overall losses, it is often useful to introduce partial Q-factors for each mechanism. Of particular importance in the context of BICs is the radiative quality factor,

$$Q_{\mathrm{rad}} = \frac{\omega_0}{2\gamma_{\mathrm{rad}}}, \tag{2.47}$$

which isolates the contribution from radiative leakage. This quantity directly reflects how strongly the mode couples to the radiation continuum and thus serves as the key metric for identifying and quantifying qBIC resonances.

In the case of BIC, the radiative loss rate vanishes ($\gamma_{\mathrm{rad}} = 0$), which corresponds to a formally diverging quality factor $Q \to \infty$. Once a perturbation is introduced into the BIC, as discussed in Sec. 2.2.3, the radiative loss rate γ_{rad} scales quadratically with the perturbation parameter α. Consequently, the radiative quality factor Q_{rad} exhibits an inverse quadratic dependence on α.

By employing the TCMT framework, experimental or simulated spectra can be fitted to extract the radiative loss rate γ_{rad} and the corresponding quality factor Q_{rad}. This procedure provides a practical means to identify BIC modes.

3

Methodology

3.1 General workflow

This chapter sets out the practical methods used across the full workflow, from design through fabrication to measurement. Each stage relies on precise, recipe-level procedures. We therefore highlight only the principal steps and decision points here. Project-specific operating details are provided in the Methods sections of the respective studies.

In experimental nanophotonics, the typical sequence is as follows. Guided by the literature and our existing knowledge, we first formulate an initial, exploratory design concept and assess its feasibility with electromagnetic simulations. When the concept appears viable, we proceed to device fabrication, conducted mainly in a cleanroom and involving substrate cleaning, material deposition, patterning and etching. The completed samples are then optically characterized, and the results are analyzed and consolidated into a manuscript.

Feedback between different stages continuously shapes the direction of a project. In experimental physics, systematic documentation at multiple levels is equally essential. For instance, simulation results should be summarized in a timely manner and linked to their file sources, so that later adjustments can be guided by comparison with experimental data. Recording experimental parameters and data summaries at each stage not only helps in structuring one's own project

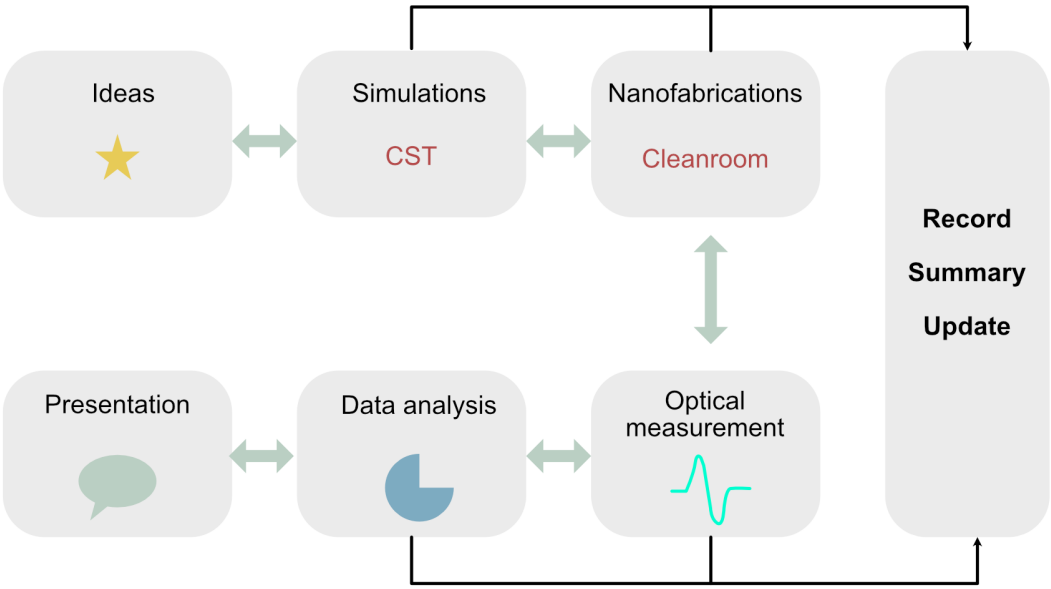

Figure 3.1: General workflow of the project. The workflow consists of sequential steps from concept generation and simulation, to cleanroom fabrication, and finally optical characterization and analysis. Each step involves iterative feedback that guides the project's direction.

but also facilitates the sharing of information with collaborators. Keeping such records is more than a formality: it serves as a basis for reflection, provides evidence of progress, and ensures that the content and scope of one's work are transparent. Ultimately, this process of documentation, review, and traceability plays a critical role both in the advancement of individual projects and in personal scientific development.

3.2 Numerical simulations

In this thesis, the electromagnetic response of the metasurface structures was simulated using the CST Studio Suite, which is part of the SIMULIA brand under Dassault Systèmes (France). The CST platform is based on a full-wave electromagnetic solver framework, where Maxwell's equations are solved numerically in a discretized computational domain to obtain the steady-state or transient electromagnetic field distributions, as well as the transmission and reflection spectra.

In physical reality, the electric field $\mathbf{E}$ and magnetic field $\mathbf{H}$ are continuous vector fields defined at every point in space and evolve according to Maxwell's

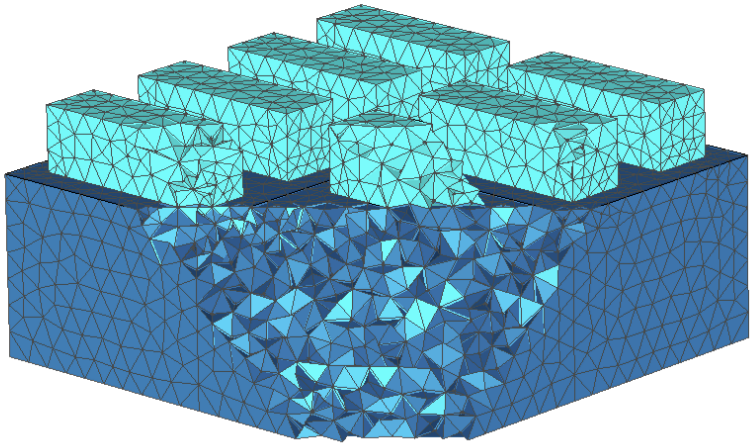

Figure 3.2: Discrete mesh schematic. The simulation domain is discretized into volumetric cells. Material properties such as permittivity ε and permeability μ are assigned to each mesh cell. Electromagnetic field components are stored on the edges and faces of the grid elements, enabling the numerical evaluation of Maxwell's equations on a discrete spatial lattice.

equations. These continuous field quantities cannot be directly computed by a digital computer, which only operates on discrete values. Therefore, the simulation space is partitioned into a finite number of volumetric elements (mesh cells), as illustrated in Figure 3.2. The material parameters (i.e., permittivity ε and permeability μ) are assigned to each cell, and the fields are represented as discrete quantities located on the edges or faces of these cells.

The boundaries between adjacent mesh cells are not treated as physical breaks. Instead, they form numerical interfaces through which the electromagnetic fields are continuously coupled. As a result, the continuity of the fields and the conservation of electromagnetic energy are automatically maintained in the numerical scheme. This ensures that material interfaces are accurately represented and that the propagation of electromagnetic waves is modeled in a physically consistent way.

Depending on the physical characteristics of the structure, CST offers solvers including time-domain and frequency-domain:

Time-domain solver employs a broadband pulse excitation and iteratively updates the electromagnetic fields in the time domain. The fields propagate through the mesh cells according to Maxwell's equations, allowing the full transient response to be captured. A Fourier transform is subsequently applied

to extract the broadband scattering parameters. This method is highly efficient for wideband responses and metasurfaces with moderate-Q resonances.

Frequency-domain solver assumes a steady-state harmonic excitation at a specific frequency and directly solves the corresponding frequency-domain Maxwell eigenvalue problem. Instead of tracking the temporal evolution of the fields, it computes the spatial distribution of the electromagnetic fields that satisfies Maxwell's equations at the specified frequency. This approach is particularly advantageous for high-Q resonances, like qBICs, and other narrowband phenomena where accurate extraction of the resonance frequency and quality factor is required.

To emulate an infinite periodic metasurface, periodic boundary conditions were applied along the in-plane directions (x and y), while perfectly matched layers (PML) or open boundary conditions were imposed along the propagation direction (z) to absorb outgoing waves without artificial reflections. Field monitors are placed at interesting frequencies to record the fields distribution. The scattering parameters S_{21} and S_{11} were obtained by normalizing the transmitted and reflected power to the incident wave, enabling direct calculation of the transmission and reflection spectra.

The transmittance spectrum is calculated as $T = |S_{21}|^2$ and the reflectance spectrum as $R = |S_{11}|^2$, based on the power flow through the output and input ports, respectively. The absorption is then obtained by energy conservation as $A = 1 - T - R$, which quantifies the electromagnetic energy dissipated within the structure. The simulated electric and magnetic field distributions provide direct physical insight into the underlying resonance mechanisms and mode profiles of qBICs.

3.3 Nanostructure fabrication

All nanofabrication steps in this dissertation were carried out in the institutional cleanroom under the local safety regulations. Access was granted only after completion of the mandatory safety briefing and tool-specific training, and equipment usage was performed under supervisor approval with proper logging. Standard gowning and contamination-control practices were followed throughout, and only essential, pre-cleaned items were brought into the facility. Shared workstations were cleaned after each use. Routine solvents, resists,

and wet-chemistry reagents (e.g., acetone/IPA for rinsing, PMMA/CSAR for lithography, metal etchants, and lift-off removers) were handled exclusively in designated fume hoods using appropriate personal protective equipment and in accordance with the corresponding Safety Data Sheets. Chemical containers and waste streams were clearly labeled and disposed of via the certified waste management system, and any incidents were addressed immediately using the available emergency equipment (eye-wash/shower) and reported to the clean-room staff. These measures ensure both personnel safety and the reproducibility of the fabrication workflow.

3.3.1 Thin film deposition

Thin film deposition constitutes a fundamental step in nanofabrication, providing the essential material platforms for subsequent lithography and etching processes. In the following sections, physical vapor deposition (PVD) and chemical vapor deposition (CVD) methods are introduced, with a focus on the specific materials and techniques employed in this dissertation. Detailed experimental recipes are provided in the corresponding Methods sections of individual projects in the following chapters, and a comprehensive introduction can be found in Chapter 4 of Nanostructures and Nanotechnology from Cambridge University Press[45].

Thermal and e-beam evaporation

PVD forms thin films by converting a solid target into a vapor under high vacuum and condensing it on a cooler substrate. The vacuum level (typically $\leq 10^{-5}$ mbar) ensures a long mean free path so that atoms travel ballistically from source to substrate. In this thesis, we use three PVD variants, **thermal evaporation**, **electron beam (e-beam) evaporation**, and **sputtering** to deposit metals (eg. Au, Cr) and dielectrics (eg. SiO_2, TiO_2). E-beam evaporation is preferred for refractory metals and some dielectrics, whereas thermal evaporation is convenient for materials with moderate vapor pressure. While PVD may yield films of somewhat lower density than chemical routes, its low substrate temperature enables deposition without heating the device area, which helps avoid stress and deformation from thermal-expansion mismatch in multilayer assemblies. The schematic of thermal and e-beam PVD is shown in Figure 3.3.

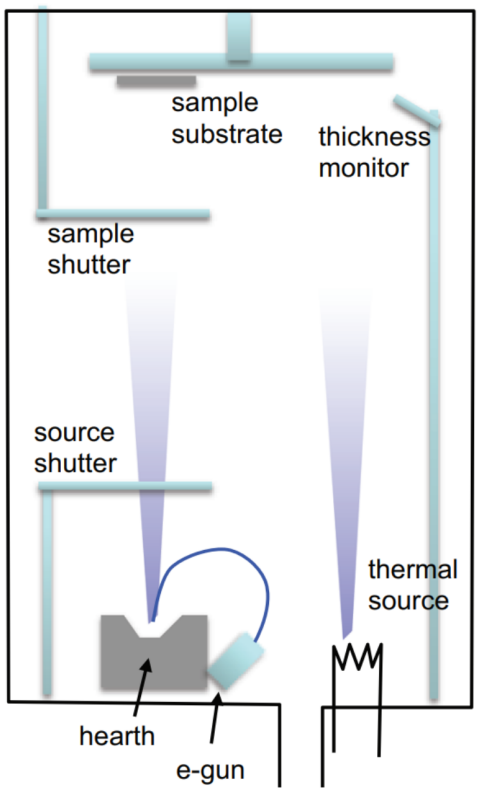

Figure 3.3: Schematic of the thermal and e-beam physical vapor deposition system. High vacuum is maintained by a turbomolecular or diffusion pump, and the deposition rate is monitored by a quartz crystal monitor. The source can be a thermal evaporation source or an electron beam source to accommodate different target materials. Adapted from[45].

In this dissertation, Cr and Au mask layers were deposited by thermal and e-beam evaporation. The deposition rate was regulated by source current (thermal) or beam power (e-beam) and monitored with a quartz-crystal sensors A rate of $0.5\,\text{Å}\,\text{s}^{-1}$ to $1.0\,\text{Å}\,\text{s}^{-1}$ was used to promote uniform morphology and adhesion. A mechanical shutter enabled precise start/stop control and rate stabilization before opening to the substrate. Film uniformity across the wafer was tuned by substrate rotation: continuous rotation averages the angular flux for uniform thickness, whereas for lift-off processes, rotation was intentionally disabled to maintain directional deposition and avoid coating resist sidewalls, ensuring clean pattern transfer.

Sputtering

Sputtering is another PVD technique in which a low-pressure noble gas (typically Ar) is ionized to form a plasma near a solid target. Energetic ions are accelerated toward the target and transfer momentum to surface atoms, which are ejected

and condense on the substrate. DC sputtering is commonly used for conductive targets (metals), while RF sputtering enables deposition from insulating targets.

In our work, amorphous TiO_2 thin films were deposited by reactive sputtering using a Ti target in an Ar/O_2 plasma environment. During the process, sputtered Ti atoms react with oxygen near the substrate to form TiO_2, which condenses as a uniform thin film. The film thickness was controlled by adjusting the deposition time and sputtering power, while the O_2:Ar flow ratio was tuned to regulate the oxygen stoichiometry. Substrate rotation was employed throughout the process to enhance thickness uniformity and improve overall film quality.

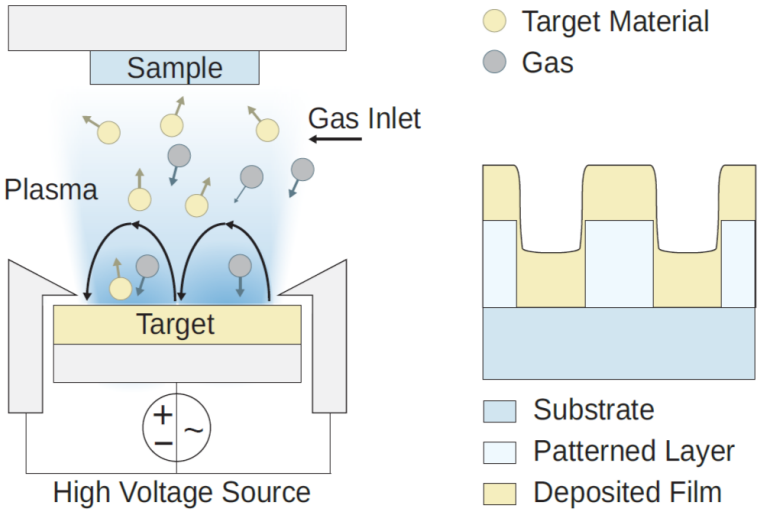

Figure 3.4: Schematic of the sputtering deposition system. A process gas is introduced into a vacuum chamber and ionized into a plasma using either DC or RF power. The resulting ions are accelerated toward the target, ejecting atoms that propagate toward the substrate to form a thin film. Scattering events in the plasma lead to a deposition profile that is not purely line-of-sight, enabling relatively uniform coverage across the substrate surface. Adapted from[46]

Figure 3.4 illustrates the sputtering process used for thin-film deposition. A process gas is introduced into a vacuum chamber and ignited into a plasma using either a direct-current (DC) or radio-frequency (RF) power source, depending on the target material. The ionized gas species are accelerated toward the target, ejecting atoms through momentum transfer. These atoms travel through the plasma and condense on the substrate to form a thin film. Due to scattering during propagation, the sputtered atoms are not strictly deposited in a line-of-sight manner, resulting in conformal films with partial sidewall coverage, as shown in Figure 3.5, which is advantageous for uniform coatings but less suitable for liftoff processes.

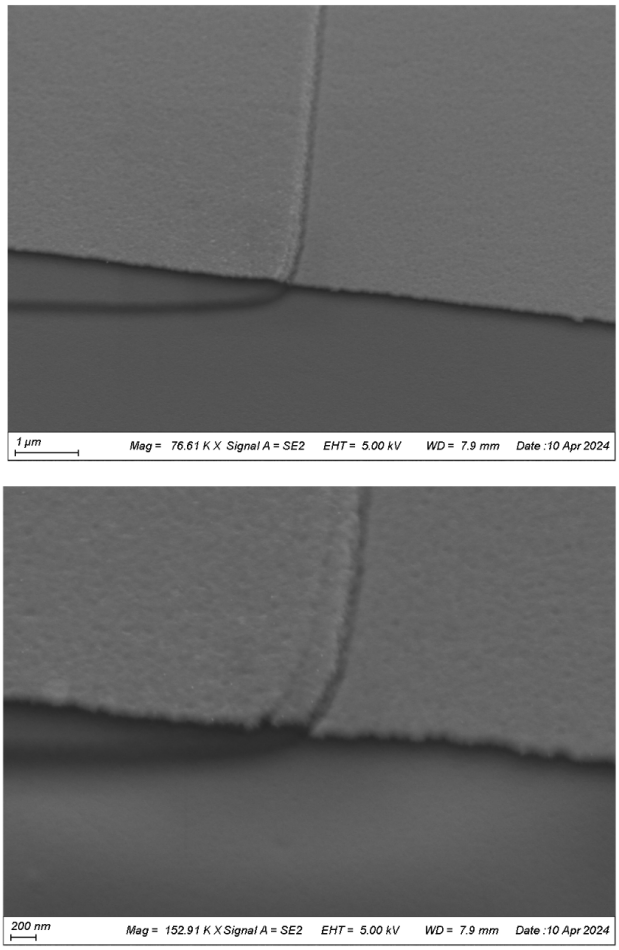

Figure 3.5: SEM image after sputtering deposition. The deposited material is clearly visible not only on the top surface but also along the sidewalls of the patterned features, confirming the non-directional nature of the sputtering process and its ability to provide conformal coverage on vertical surfaces.

Chemical vapor deposition

CVD forms solid films by delivering gaseous precursors to a heated substrate, where they react and form a solid layer. In this thesis, we employ the plasma-enhanced CVD (PECVD), in which the chemical reactions are activated by a low-pressure RF plasma rather than relying solely on high substrate temperature.

In PECVD, as shown in Figure 3.6, a mixture of carrier and precursor gases (e.g., SiH_4 with N_2O or NH_3 for SiO_2/SiN_x) is introduced into the reaction chamber at pressures of a few hundred millitorr. An RF field sustains a partially ionized plasma. Electrons in the plasma energize the precursor molecules and generate reactive radicals, which adsorb on the substrate surface and form the thin film. Because the reaction is plasma-driven, film growth can proceed at relatively low

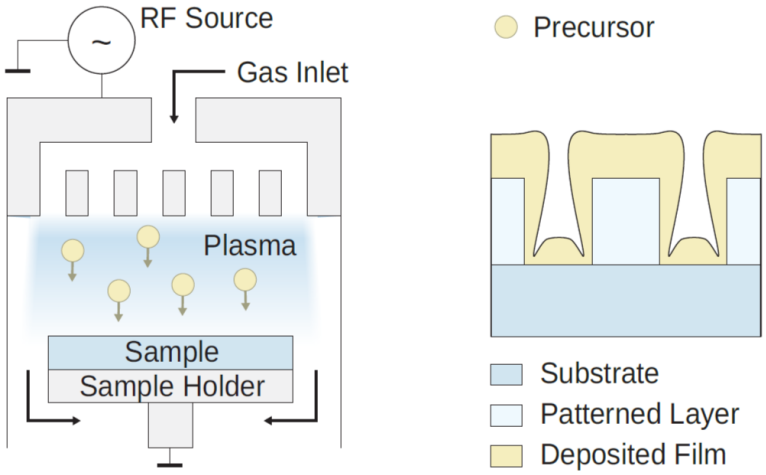

Figure 3.6: Schematic of the plasma-enhanced chemical vapor deposition process and the resulting film profile. Process gases enter the chamber through a showerhead electrode connected to an RF power source, where a low-pressure plasma is generated to activate the precursor molecules. These reactive species diffuse toward the heated substrate and undergo surface reactions, forming a thin film. By-products are continuously removed via vacuum pumping to maintain a stable environment. The deposition proceeds isotropically, coating both horizontal and vertical surfaces. Adapted from[46]

substrate temperatures (approximately 150–350 °C), which is advantageous for deposition on temperature-sensitive layers.

Process control in PECVD relies on a set of adjustable parameters, including RF power, chamber pressure, gas flow rates and mixing ratios, substrate temperature, and DC bias. Increasing RF power or bias generally enhances ion energy, leading to higher film density. Higher chamber pressure improves step coverage by enhancing scattering, though it may reduce directionality. The gas flow ratios determine film composition and influence the optical constants. Substrate temperature and post-deposition annealing help form better film quality.

In this thesis, PECVD (PlasmaPro 100, Oxford Instruments) is employed to deposit dielectric spacer layers and amorphous silicon (a-Si) films for the nanoresonators. For the a-Si deposition, the sample is loaded into the reaction chamber and silane (SiH_4) is introduced at a flow rate of 500 sccm, resulting in a chamber pressure of 1000 mTorr. An RF power of 10 W is applied to ignite a plasma between the substrate and the RF electrode. The plasma activates surface reactions that lead to the formation of amorphous silicon directly on the substrate, enabling thin-film growth. Owing to the plasma activation, the deposition process can be performed at a reduced substrate temperature of approximately 180 $^{\circ}C$, which is beneficial for avoiding thermal expansion problem among multilayer substrate.

PECVD provides excellent thickness uniformity and sufficient film density across nanostructured surfaces. These process choices ensure stable optical properties and reproducible performance in the metasurface stacks investigated in this thesis.

3.3.2 Electron beam lithography

Electron beam lithography (EBL) is the core technique for nanofabrication, enabling the direct transfer of computer-designed nanoscale patterns onto the substrate. The design is typically stored in a `GDSII` file format, which is the industry standard for representing hierarchical layout structures with nanometer precision. Layouts can be created and modified using software such as `KLayout`, which provides an intuitive graphical interface, or generated programmatically using `Python` libraries (e.g., `gdstk`) for rapid design iterations and parametric pattern generation.

The fundamental working principle of EBL is based on scanning a focused beam of high-energy electrons over an electron-sensitive resist layer according to the predefined pattern. When a positive resist (such as PMMA) is used, the exposed regions undergo chain scission, reducing their molecular weight. These regions are subsequently removed in the development step, leaving behind the nanoscale pattern. Conversely, for negative resists, the exposed areas become crosslinked and remain after development. The resulting resist pattern serves either as a mask for etching or as a stencil for lift-off processes to define the final nanostructures.

As illustrated in Figure 3.7, the system scans a focused electron beam across a resist-coated substrate according to a computer-defined pattern, enabling the direct writing of arbitrary nanostructures with high spatial resolution.

The accuracy of EBL depends critically on several preparatory alignment and calibration steps. Each step is essential to ensure pattern fidelity, overlay accuracy, and dose control:

1. **Beam alignment:** The electron beam must be precisely focused and centered to minimize aberrations. Astigmatism correction and beam centering are performed to ensure that the beam profile is circular and stable, which directly influences the resolution and edge sharpness of the written features.

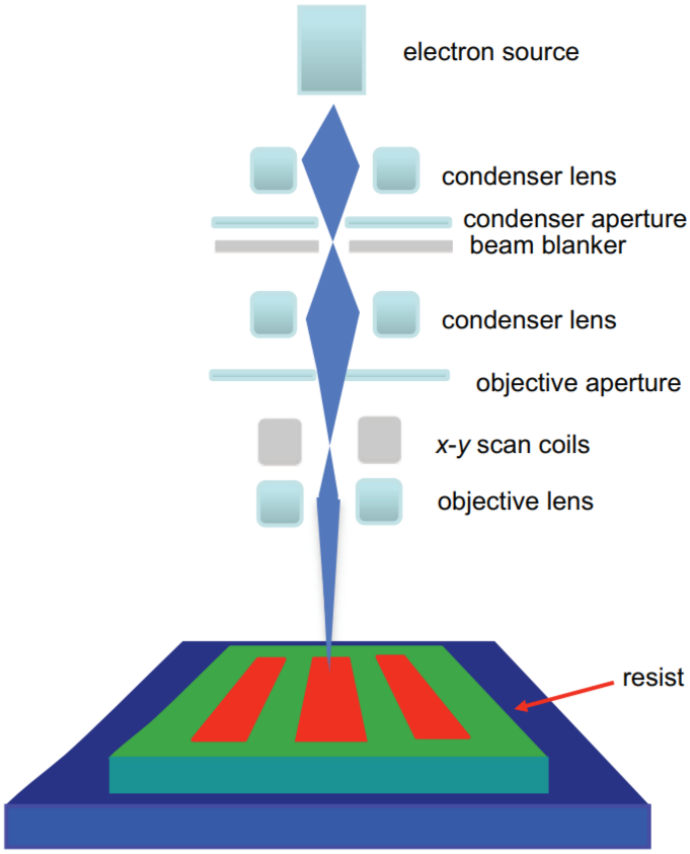

Figure 3.7: Schematic of an electron beam lithography system. An electron beam generated from a thermionic or field-emission source is focused and shaped by a series of condenser and objective lenses. The x–y scan coils deflect the beam to follow a predefined pattern over the resist-coated substrate, while a beam blanker prevents unwanted exposure during repositioning. The interaction between the electron beam and the resist enables nanoscale pattern transfer with sub-10 nm precision. Adapted from[45].

2. **Write-field alignment:** Large-area exposures are divided into multiple write fields. To ensure seamless stitching between fields, the system aligns the stage coordinates with the beam deflection coordinates. Accurate write-field alignment prevents pattern displacement and is crucial when fabricating periodic metasurfaces over millimeter-scale areas.

3. **Beam current measurement:** The beam current drifts on the timescale of hours due to source (column) instabilities. We therefore measure the current I_{meas} immediately before exposure and treat it as the fixed reference.

4. **Beam step size and field calculation:** The exposure area is discretized into a grid of pixels or steps. The beam step size is calculated based on the desired resolution and writing strategy (e.g., raster or vector scan). Proper step size selection ensures high pattern fidelity while minimizing writing

time. Using I_{meas}, a target areal dose D, we convert the dose into either dwell time or scan speed.

5. **Dose factor:** The electron dose, defined as the charge per unit area, must be optimized according to the resist type, thickness, substrate, and desired feature size. An incorrect dose can cause over- or incomplete development, failing to transfer target nano shape. Dose tests are often performed to determine the optimal parameters for each specific design.

   In practice we define a nominal dose D_0 (e.g., $100\ \mu\mathrm{C/cm}^2$) and apply a multiplicative *dose factor* f (typically 0.3–1.5) to compensate for proximity effects, resist thickness, substrate backscattering, and development conditions, i.e., $D = f\,D_0$. This procedure makes the exposure robust to slow current drift while keeping feature dimensions reproducible.

In summary, electron beam lithography provides the flexibility and precision required for the fabrication of high-quality metasurfaces. Its ability to write arbitrary nanoscale geometries with sub-10 nm accuracy makes it indispensable for fabrication in this thesis.

3.3.3 Inductively coupled plasma reactive ion etching

Inductively Coupled Plasma Reactive Ion Etching (ICP-RIE) is a widely used dry etching technique that enables the fabrication of high-aspect-ratio nanostructures with nanometer-scale precision. It combines the advantages of chemically reactive plasmas and directional ion bombardment, allowing for both high etch selectivity and strongly anisotropic profiles. In contrast to conventional RIE, ICP-RIE employs two independent RF power sources: an inductively coupled RF coil to generate a high-density plasma, and a separately applied RF bias on the substrate stage to control the incident ion energy. This decoupled configuration enables precise tuning of the etching conditions, such as etch rate, selectivity, and sidewall angle.

The etching chemistry is determined by the target material. Fluorine-based gases such as SF_6 or CHF_3 are commonly used for silicon and silicon dioxide, while chlorine-based chemistries (e.g., Cl_2, BCl_3) are used for metals. In the plasma, reactive neutral species form volatile reaction byproducts with the substrate material, while inert ions provide directional momentum transfer to achieve

vertical sidewalls. By carefully adjusting process parameters such as chamber pressure, gas ratio, ICP power, and substrate bias, ICP-RIE can produce smooth sidewalls, minimize surface damage, and achieve high etch fidelity with respect to the designed pattern.

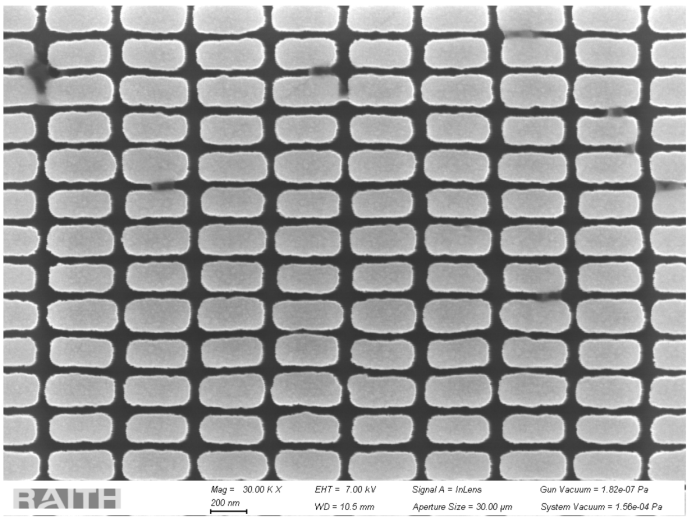

Figure 3.8: SEM image of nanostructures after ICP-RIE etching. The etched features exhibit sharp edges, indicating excellent anisotropy and high etch fidelity. This confirms that the ICP-RIE parameters were properly optimized to preserve the designed geometry at the nanoscale.

Figure 3.8 presents a SEM image of the fabricated metasurface after the ICP-RIE process. The nanostructures show clearly defined edges with minimal footing, demonstrating the high anisotropy of the etching process. Such feature quality is crucial for achieving the designed optical response, as deviations in sidewall angle or surface roughness can significantly alter the resonance behavior.

At this stage, the nanostructures defined in the GDS layout have been successfully transferred from the computer design into the physical sample. This marks the completion of the patterning step, where the virtual geometry is realized on the substrate with nanoscale accuracy.

3.4 Optical characterization

After completing the nanofabrication process, the optical response of the metasurface must be experimentally characterized to verify the designed resonant features. In this thesis, two primary measurement platforms are employed: a confocal microscope for characterizing resonances in the visible to near-infrared range, and a quantum cascade laser (QCL) based infrared microscope for probing

the mid-infrared spectral region. These two systems enable high-resolution spectral acquisition under normal or oblique incidence, allowing direct observation of qBIC resonances.

3.4.1 Optical characterization in the visible range

Optical transmission measurements in the visible range were performed using a confocal white-light microscopy system (WITec alpha300 R). A broadband halogen lamp (Thorlabs OSL2) was used as the illumination source, emitting linearly polarized light that is collimated and directed vertically through the transparent substrate onto the metasurface. The transmitted light is then collected using either a $10\times$ (NA = 0.25) or $50\times$ (NA = 0.80) objective, depending on the desired spatial resolution and collection efficiency.

As shown in Figure 3.9, above the objective, the collected light is focused and coupled into a multimode optical fiber, which ensures confocal detection and efficient coupling into the spectrometer. Inside the spectrometer, the light is dispersed by a diffraction grating and recorded by a CCD detector, yielding the transmission spectrum of the metasurface. To isolate the resonant response of the nanostructure, all measured spectra are normalized to the transmission through the bare substrate (typically SiO_2). This configuration allows the selective probing of qBICs and other resonances under normal-incidence excitation.

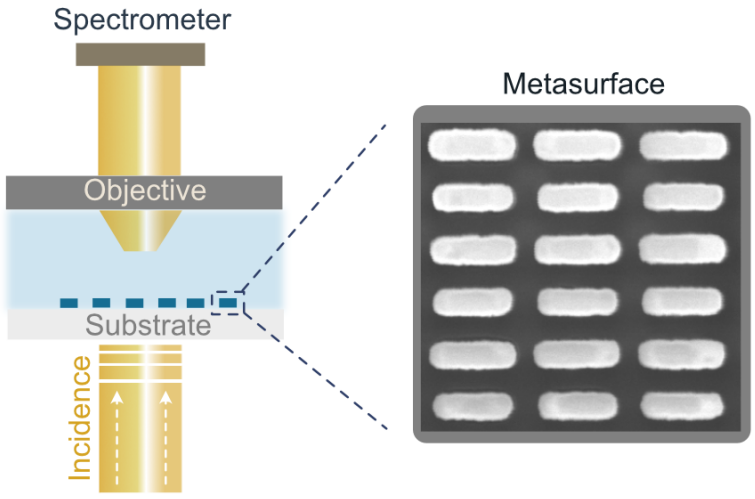

Figure 3.9: Experimental setup for transmission measurement using WITec. A linearly polarized white-light beam is collimated and directed vertically through the substrate. The transmitted field is collected by a microscope objective and coupled into a fiber-connected spectrometer for high-resolution spectral analysis.

3.4.2 Optical characterization in the Mid-IR range

In the mid-infrared regime, optical measurements were performed using a wide-field spectroscopic imaging microscope (Spero, *DRS Daylight Solutions Inc.*), which employs an external-cavity quantum cascade laser as its illumination source. Unlike the broadband white-light excitation used in the WITec system, the QCL provides spectrally narrowband, tunable radiation with a linewidth of approximately $1\ \mathrm{cm}^{-1}$, covering a continuous wavenumber range from 950 to $1800\ \mathrm{cm}^{-1}$. This spectral window corresponds to the so-called molecular fingerprint region, where many vibrational resonances of biomolecules, proteins, and polymers are located. As a result, the Spero microscope is of particular interest for chemical sensing and bio-detection applications, where qBICs can be exploited to enhance light–matter interaction at these characteristic absorption frequencies.

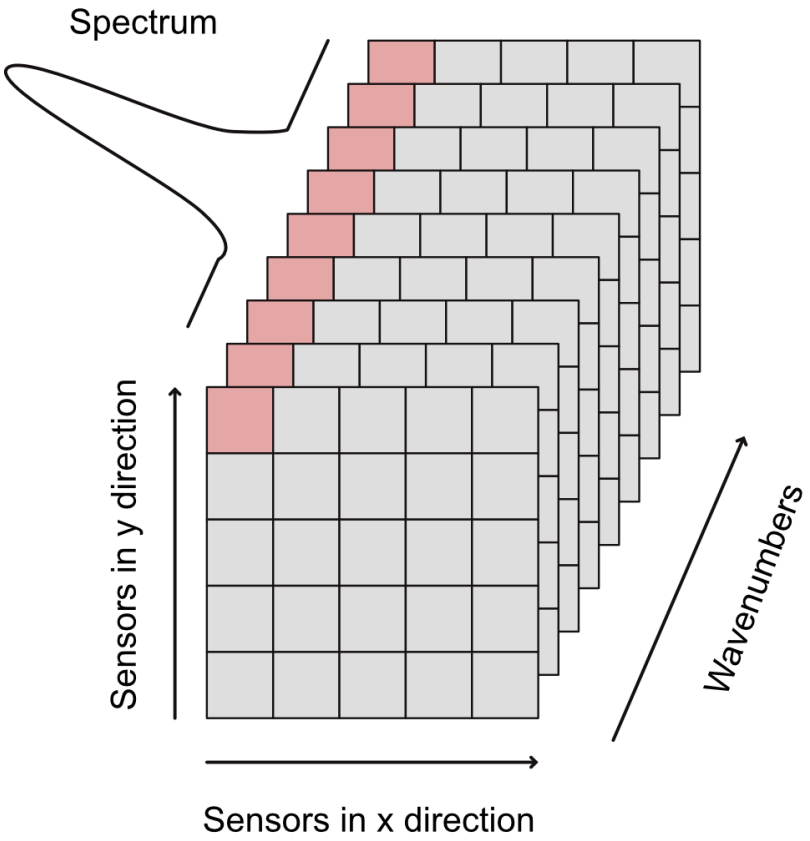

Figure 3.10: Hyperspectral data cube acquired with a QCL-IR microscope. At each wavenumber, a two-dimensional image is recorded across the sample. By tuning the QCL source, a stack of images is formed along the spectral dimension, resulting in a three-dimensional data cube. Each spatial pixel therefore contains a complete infrared spectrum, enabling spatially and spectrally resolved investigation of resonant phenomena such as qBICs.

For each discrete wavenumber, the microscope records a two-dimensional image using an uncooled focal plane array (FPA) detector based on micro-bolometer technology with a matrix of 480 $\times$ 480 pixels, as illustrated in Figure 3.10. By sequentially tuning the laser across the spectral range, a hyperspectral data cube is constructed, where each pixel in the field of view contains a full transmission or reflection spectrum along the spectral axis.

Depending on the selected objective, the corresponding pixel size is either 1.3 μm (high-magnification objective, NA = 0.7) or 4.3 μm (low-magnification objective, NA = 0.3), resulting in spatial resolutions better than 5 μm and 12 μm at a wavelength of 5.5 μm. The resulting field of view (FOV) covers either 650 $\times$ 650 μm^2 or 2 mm $\times$ 2 mm, enabling both high-resolution mode profiling and large-area mapping[47].

This data format provides both spatial and spectral information simultaneously, enabling the direct visualization of resonance dispersions, mode profiles, and refractive-index-dependent shifts across the metasurface.

To ensure measurement accuracy, the optical chamber is continuously purged with dry nitrogen to eliminate atmospheric absorption (such as water vapour and CO_2), and the raw data is normalized using a background reference.

4

Permittivity-asymmetric qBICs for refractive index sensing

The content of this chapter is published in the scientific journal Nanophotonics (Xingye Yang, Alexander Antonov, Haiyang Hu, Andreas Tittl. Permittivity-asymmetric qBIC metasurfaces for refractive index sensing. Nanophotonics, vol. 14, no. 27, 2025, pp. 5311-5321. see ref.[48]). As the foundation of the chapter, the peer-reviewed manuscript is used and text elements such as words, sentences, full passages, as well as graphic content and figures, are drawn directly from the publication in accordance with the open-access Wiley publication guidelines that allows the reprinting of own contributions in theses and in accordance with the terms of the CC-BY Creative Commons Attribution 4.0 International license http://creativecommons.org/licenses/by/4.0/.

4.1 Research background

Among the various optical resonances in nanophotonics, bound states in the continuum stand out for their ability to confine light without radiative loss, enabled by symmetry or interference that decouples them from free-space modes[25,37]. In particular, if the coupling constants vanish due to symmetry, such BIC are symmetry-protected BICs[26,49,50]. To make these idealized, non-radiative states accessible in practical devices, a slight symmetry-breaking is typically introduced, transforming them into quasi-BICs that retain high quality factor, which is suitable for compact devices[32,33,51,52]. Conventional implementations usually achieve this by introducing minor geometrical asymmetries, such as tilted elliptical rods[29], nanodisks with off-centered holes[53], or asymmetric split-rings[54], among other structures[55–57].

Among the many emerging applications, refractive index (RI) sensing based on symmetry-protected BIC metasurfaces has recently attracted growing interest. Compared to other types of metasurfaces[14,58–60], qBIC resonances offer the advantage that their Q factor can be tuned simply by adjusting the geometrical asymmetry[16,61–64]. However, like most resonance-based sensing platforms, the readout method for the environmental RI changes relies on tracking the spectral shift of an optical resonance due to changes in the surrounding medium[65,66]. It typically requires high-resolution spectrometers and stable broadband light sources, which add cost and complexity[67,68].

To address these practical constraints, recent efforts have explored single-wavelength intensity variation, where the sensing signal is extracted from the intensity modulation at a fixed probe wavelength near the resonance[67,69,70]. Such an approach simplifies the hardware and enables integration into compact, low-cost platforms.

However, for conventional geometry-asymmetric qBIC (g-qBIC) metasurfaces, the radiative loss is essentially fixed during sensing. In low-loss environments, changes in the surrounding refractive index do not alter the radiative loss, and thus mainly induce a lateral spectral shift with minimal impact on the vertical modulation depth of the resonance[13,71–74].

In contrast, permittivity-asymmetric qBIC metasurfaces can offer a fundamentally different mechanism for interacting with the RI environment. It is well known that radiative coupling of qBICs with far-fields is governed by the asymmetry

factor, which is conventionally defined by the structure's geometrical asymmetry as mentioned before[16,64]. However, according to our previous research, based on the permittivity-asymmetric qBIC (ε-qBIC) metasurfaces, we can encode the environmental RI into the asymmetry factor of the system[75]. As a result, the qBIC becomes highly responsive to RI variations, resulting not only in a shift of resonance position, but also in a pronounced modulation of its amplitude in the low-loss system. This response improves the linearity of the sensing signal in single-wavelength analysis, which, while not strictly required for all sensing approaches, facilitates simpler and more robust signal interpretation compared to nonlinear sensing data distributions with environmental RI, thereby enhancing sensing stability.

In this chapter, the sensing performance of ε-qBIC metasurfaces is demonstrated, and the concept of an environment-accessible restored BIC enabled by permittivity asymmetry is proposed through simulations. Simulations and experiments first confirm that the ε-qBIC metasurface exhibits not only resonance wavelength shifts but also additional resonance modulation with changes in the RI, in contrast to the purely wavelength-shift response of g-qBIC's spectrum, using commercially available refractive index oils ($\Delta n = 0.02$). To evaluate the relative quality of signals between wavelength shift and single-wavelength intensity modulation, sensing experiments were further conducted with smaller RI intervals ($\Delta n = 0.004$). The intensity variation signal (ΔT_{s}) at a probe wavelength achieved a higher signal-to-noise ratio (SNR $\approx$ 17 dB) compared to the wavelength-shift signal ($\Delta \lambda_{\mathrm{s}}$) (SNR $\approx$ 5 dB).

Consequently, the intensity variation signal (ΔT_{s}) was further analyzed, and the experimental responses of ε-qBIC and g-qBIC metasurfaces were compared. Comparable sensitivities were obtained for both metasurfaces ($\sim$5000%/RIU). However, the ε-qBIC metasurface exhibited a markedly improved linearity of the sensing response, with a linear window, defined as the wavelength range where the extracted linearity parameter exceeds the preset threshold, whose integrated area is approximately 104 times larger than that of the g-qBIC. This wider window indicates lower noise across a broader wavelength range, thereby improving robustness and stability for practical sensing applications.

Finally, from a fundamental perspective, numerical results reveal that geometric asymmetry, which typically converts BICs into qBICs, can be compensated by precisely tailoring the environmental permittivity profile within the unit cell.

This enables the recovery of BICs with radiative losses approaching zero. Notably, the restored symmetry-protected BICs (RSP-BIC[76]) become optically accessible to changes in the surrounding environment, an interaction that is otherwise forbidden for conventional BICs. These findings suggest a broader design strategy: radiative channels in BIC systems can be tuned not only through geometry but also via environmental permittivity engineering, enabling new possibilities in high-performance photonic platforms for practical sensing applications.

4.2 RI-controlled asymmetry factor in ε-qBIC metasurfaces

To construct the ε-qBIC resonance mode in our metasurface, the design follows two steps. First, the unit cell is composed of two identical TiO_2 nanorods, which support a symmetry-protected BIC due to their structural symmetry. Second, a dielectric cover layer is selectively applied to one of the rods, introducing a difference in permittivity between the surroundings of the nanorods. This breaks the symmetry in the permittivity distribution and transforms the original BIC into a qBIC, accompanied by a radiative resonance and a distinct electric field profile (Figure 4.1a–b).

The asymmetry in permittivity leads to unequal dipole strengths between the two out-of-phase electric dipoles, resulting in a nonzero net dipole moment. This enables the resonance to couple to the far field and become observable in the transmission spectrum. Specifically, the two TiO_2 nanorods have dimensions of $l = 320\ \mathrm{nm}$ in length, $d = 105\ \mathrm{nm}$ in width, and $h = 110\ \mathrm{nm}$ in height. One of the rods is fully encapsulated in a dielectric medium with refractive index n_{cov}, while the other remains exposed to an external medium with refractive index n_{env}.

For example, this can be implemented using a PMMA layer ($n_{\mathrm{cov}} = 1.49$) with height H of 300 nm as the cladding material. The prepared metasurface is then placed in the sensing environment (Figure 4.1c). Unlike conventional qBIC designs, such as those involving tilted elliptical rods or rods with different lengths, where the structural asymmetry, and thus the radiative loss, is fixed after fabrication, the ε-qBIC structure introduces asymmetry through the refractive index contrast between the cladding and the environment. This contrast is

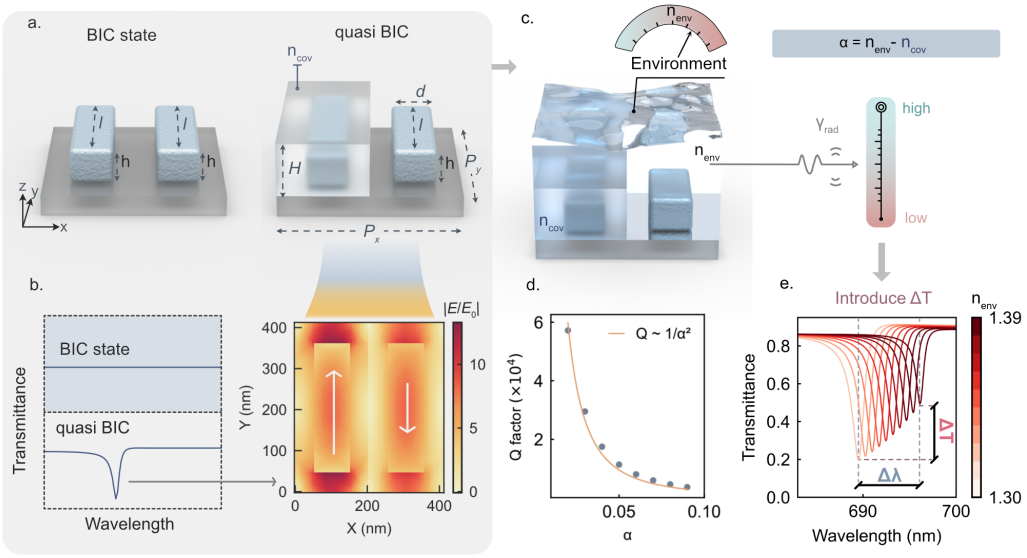

Figure 4.1: The concept of environmental permittivity-asymmetric qBIC metasurfaces for refractive index sensing. a. Illustrating the unit cell of the ε-qBIC metasurfaces, consisting of two identical dielectric nanorods made of TiO_2 with periodicities $P_x = P_y = 410$ nm. The length l, width d, and height h of the nanobar are 320 nm, 105 nm, and 110 nm respectively. One of the resonators is encapsulated in a dielectric medium with refractive index of n_{cov} and the height of H. **b.** Transition from BIC to ε-qBIC by adding a cladding layer on one of the nanobars, and corresponding electric field distribution of the ε-qBIC. **c.** Asymmetry factor defined by $\alpha = n_{\text{env}} - n_{\text{cov}}$, where $n_{\text{cov}} = 1.49$ and n_{env} represent the refractive index of the dielectric medium covering on one of the nanorods, and the global environment of the whole ε-qBIC metasurfaces respectively. **d.** The Q factor exhibits an inverse-square dependence on the asymmetry factor, indicating that the asymmetry factor can modulate the radiative loss. **e.** Spectral response under varying environmental refractive index, where changes in radiative loss additionally induce variations in transmittance intensity.

quantified by the asymmetry factor $\alpha = n_{\text{env}} - n_{\text{cov}}$, allowing the radiative loss to vary dynamically with the surrounding medium.

This chapter first demonstrates RI sensing where environmental changes are directly translated into both the asymmetry factor and the associated radiative loss. As shown in Figure 4.1d, the Q-factor exhibits an inverse-square dependence on the asymmetry factor (related with environment RI), consistent with the characteristic behavior of qBIC modes.

This dependence is also reflected in the optical spectra: as the refractive index of the environment varies (from 1.30 to 1.39), the system exhibits not only a shift in resonance wavelength but also a modulation in resonance strength (Figure 4.1e). This feature improves the linearity of the sensing signal readout, resulting in better stability over a broader wavelength range. We will return to this point later. Before that, we experimentally verify the simulation results, as discussed in the next section.

In addition, it is worth noting that, PMMA, while convenient for proof-of-concept demonstrations, suffers from poor durability in practical applications such as biosensing environments[77]. In particular, it is soluble in many common organic solvents such as acetone and chloroform, and is easily removed during plasma cleaning processes[78]. Moreover, although PMMA can remain stable in aqueous buffer solutions, it shows limited resistance to strong acidic or basic regeneration steps that are often required in biosensing protocols[79]. These limitations indicate that more durable polymers (e.g., SU-8[80]) or inorganic coatings (e.g., SiO_2) should be considered for future applications.

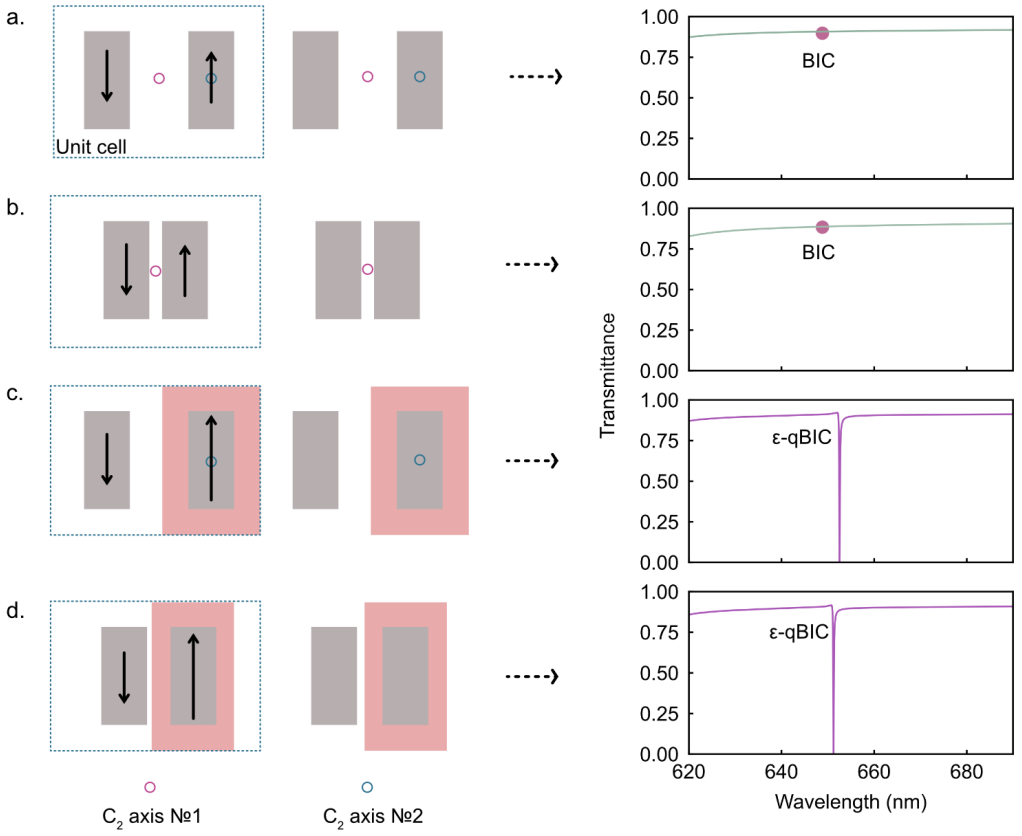

Figure 4.2: Mechanism of the ε-qBIC. a. Metasurface from the main text with equally spaced nanorods exhibiting a symmetry-protected antiparallel dipole BIC. **b.** Shifting each rod by 10 nm each doubles the period and breaks the C_2 axis No. 2, while the BIC at the Γ-point remains preserved. **c.** Introducing a 20 nm-thick PMMA layer to the structure with equally spaced nanorods breaks the C_2 axis No. 1 and transforms the symmetry-protected BIC into an ε-qBIC, as indicated by the transmittance spectrum. **d.** The same transition from BIC to ε-qBIC is observed for the structure with shifted nanorods lacking both C_2 axes.

A more detailed discussion of the ε-qBIC origin is presented in the Figure 4.2. We interpret ε-qBIC as a resonance originating from a symmetry-protected BIC. The original mode is an antiparallel dipole resonance and can be described by

a pair of nanorods (Figure 4.2a), where the corresponding structure possesses multiple C_2 rotational symmetries. We focus on the two axes marked as red (axis No. 1) and blue circle (axis No. 2) in Figure 4.2. By shifting the nanorods we double the period, break the C_2 axis No. 2 and introduce Brillouin zone folding (BZF). However, we still cannot access the mode at the Γ-point (Figure 4.2b), as it remains protected by the remaining C_2 rotational symmetry described by the axis No. 1. In our work, it is crucial to break exactly this particular rotational symmetry, which we achieve by introducing a PMMA coverage. The mechanism responsible for transforming symmetry-protected antiparallel dipole BIC into a qBIC does not depend on whether the rotational symmetry associated with the C_2 axis No. 2 is preserved (Figure 4.2c) or broken (Figure 4.2d). However, the mechanism for the metasurface shown in Figure 4.2c can also be interpreted using the BZF framework[34,81], since introducing the PMMA coating both breaks the necessary C_2 axis No. 1 and doubles the period.

4.3 Experimental validation of both resonance wavelength shift and intensity modulation

To experimentally validate the refractive index sensing capabilities of both g-qBIC and ε-qBIC metasurfaces, we performed transmittance measurements (Figure 4.3a) in a controlled aqueous environment using commercial index-matching oils with well-defined refractive indices (details in Methods). Both metasurfaces share the similar Q factor measured in the air to ensure the fair comparison (Figure 4.5). Their fabrication have been confirmed through the SEM images (Figure 4.3b). The fabrication process of ε-qBIC can be found in Methods.

The transmittance spectra of g-qBIC metasurfaces are shown in Figure 4.3c, measured across a series of index-matching oils with refractive indices $n_i = 1.30$, 1.32, 1.34, 1.36, and 1.38, with a refractive index step size of $\Delta n = 0.02$. As expected, the resonance wavelength exhibits a monotonic redshift with increasing environmental index, consistent with the behavior of conventional single-parameter high-Q RI sensing platforms, with a sensitivity of 118 nm/RIU.

The centroid analysis provides the wavelength centroid of a resonance within a half-wavelength range, enabling a clearer tracking of its wavelength shift under different refractive indices (Method of centroid analysis is shown in Figure 4.4).

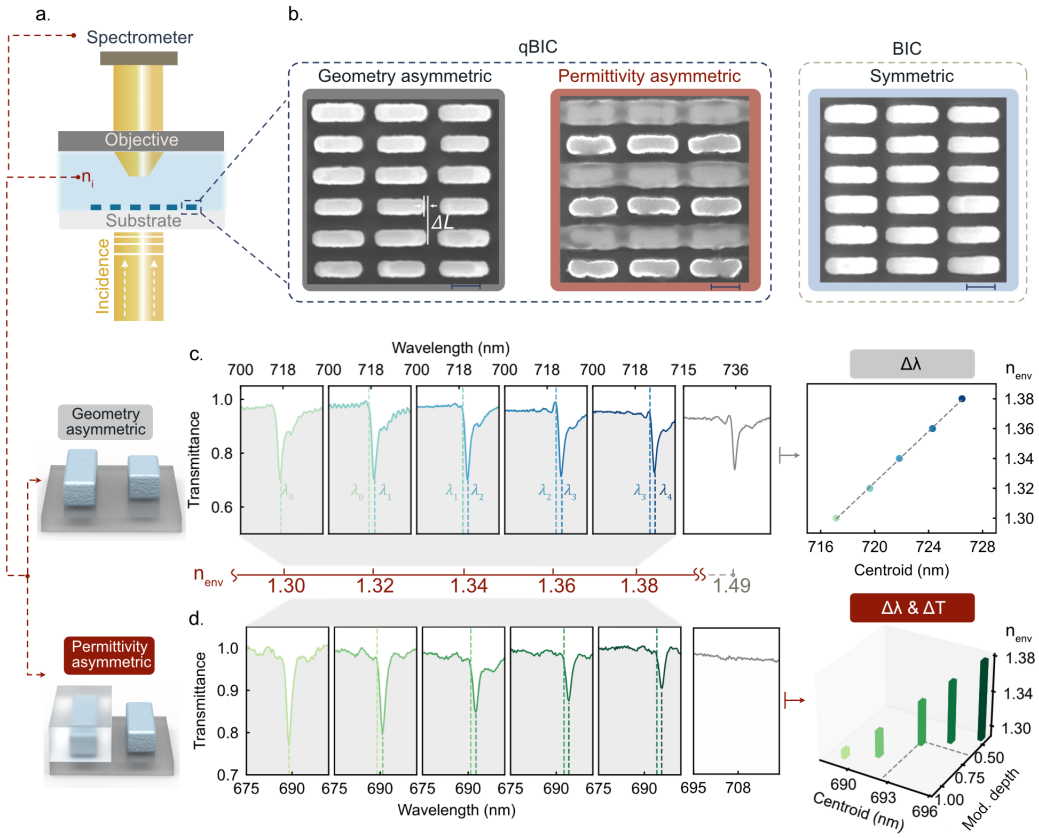

Figure 4.3: Experimental characterization of the qBIC metasurfaces for refractive index sensing. a. Schematic of the experimental setup for transmittance measurement for g-qBIC and ε-qBIC metasurfaces in an aqueous environment. **b.** The SEM images for the g-qBIC metasurfaces, ε-qBIC metasurfaces, and BIC metasurfaces. **c.** Measured transmittance spectra of g-qBIC metasurfaces immersed in commercial index-matching oils with refractive indices $n_i = 1.30, 1.32, 1.34, 1.36, 1.38$. The PMMA ($n_{\text{cov}} = 1.49$) serves as the cladding material. The corresponding resonance shifts are analyzed using a centroid method, shown on the right, where λ_0 to λ_4 denote the centroid wavelengths of the transmission dips, highlighting a clear monotonic wavelength shift as the RI increases. **d.** Measured transmittance spectra of ε-qBIC metasurfaces under the same set of environmental refractive indices. In addition to the spectral shift, the modulation depth of the resonance also varies with n_i. The right panel presents changes in both centroid wavelength and normalized modulation depth.

The centroid analysis on the right of Figure 4.3c confirms a linear trend, with the spectra shift of around 2 nm per RI step. Notably, the resonance modulation depth remains nearly constant, even at $n_i = 1.49$, indicating that the optical response is primarily governed by phase effects rather than radiative coupling changes.

In contrast, Figure 4.3d demonstrates the spectral response of ε-qBIC metasurfaces under the same set of environmental refractive indices. The resonance wavelength shows a redshift of approximately 2 nm with increasing n_i, similar to the g-qBIC case. Specifically, the sensitivity in terms of wavelength shift is 85 nm/RIU. It is slightly lower than that of g-qBIC because the initial Q-factors

of the two samples are not exactly the same but comparable, with the Q-factor of ε-qBIC ($Q = 124$) being slightly smaller than that of g-qBIC ($Q = 131$) (see in Figure 4.5). This results in a slightly lower sensitivity for ε-qBIC. Nevertheless, it can be seen that the sensing capability in terms of wavelength shift remains in the same order of magnitude for both. In addition, ε-qBIC provides an extra modulation of the resonance intensity, which can be further exploited in single-wavelength sensing to achieve improved sensing linearity.

In Figure 4.3d, the modulation depth gradually decreases and eventually disappears at $n_i = 1.49$. This critical point corresponds to a fully permittivity-symmetric configuration, where the system reverts to a BIC. The complete disappearance of the resonance provides a distinct optical signature, highlighting the strong potential sensing capability enabled by permittivity-induced asymmetry. This variation in modulation depth reflects the dependence of the Q-factor on the asymmetry factor α, as previously discussed in Figure 4.1c–e. The right panel of Figure 4.3d provides a quantitative analysis of both the resonance centroid and the modulation depth, clearly showing that ε-qBIC metasurfaces exhibit not only a resonance wavelength shift but also a change in resonance intensity.

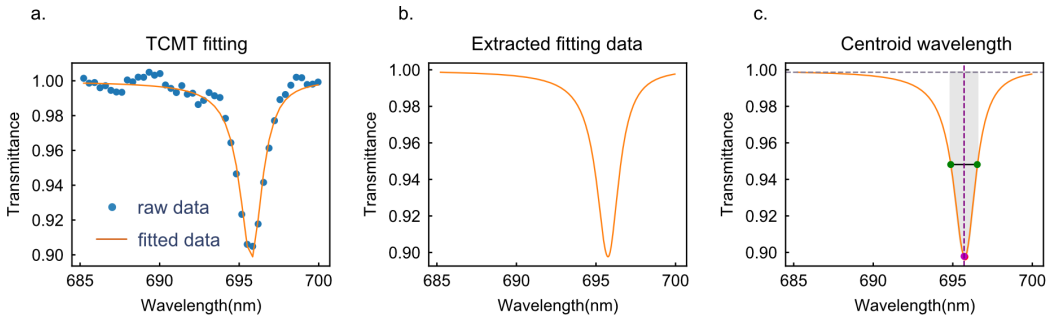

Figure 4.4: Centroid wavelength calculation. a. Raw discrete transmittance data fitted using TCMT to fit for the raw discrete spectral data. **b.** Clean fitted curve extracted from the TCMT model, applied for subsequent analysis. **c.** Illustration of centroid wavelength extraction from the fitted spectrum. The shaded gray area represents the integration region, and the vertical dashed line marks the calculated center of mass. This method follows established procedures reported in prior studies.

To accurately determine the spectral shift of the resonance, the centroid wavelength of each transmittance spectrum was extracted following the procedure illustrated in Figure 4.4. The raw discrete spectral data were first fitted using the TCMT model to obtain a smooth and continuous resonance curve. The fitted curve was then used for the centroid wavelength calculation, where the center of mass of the transmittance dip was evaluated within the integration region, as indicated by the shaded gray area in Figure 4.4c. The resulting centroid

wavelength values provide a robust and noise-insensitive measure of the spectral shift, ensuring reliable comparison among different refractive indices and experimental conditions.

In practice, the centroid wavelength λ_c is calculated as the weighted average of the spectral wavelength λ with respect to the transmittance variation. Specifically, the fitted transmittance spectrum $T(\lambda)$ is first normalized within the resonance region. The integration limits are defined by the FWHM of the fitted curve to ensure that only the resonant feature is included in the calculation. The centroid wavelength is then obtained according to

$$\lambda_c = \frac{\int_{\lambda_1}^{\lambda_2} \lambda\,[1 - T(\lambda)]\,d\lambda}{\int_{\lambda_1}^{\lambda_2} [1 - T(\lambda)]\,d\lambda}, \tag{4.1}$$

where λ_1 and λ_2 denote the lower and upper wavelength bounds corresponding to the FWHM of the resonance dip. The term $[1 - T(\lambda)]$ serves as the weighting function, representing the local absorption or reflection strength. This method effectively minimizes errors introduced by measurement noise or slight baseline fluctuations. Compared to the conventional peak-position method, centroid analysis provides a more stable and quantitative metric for tracking the resonance shift, especially when the line shape becomes asymmetric or broadened under varying environmental conditions.

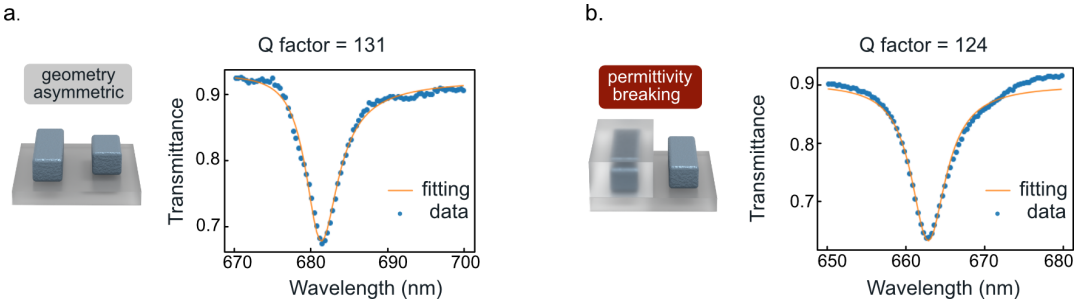

Figure 4.5: Measured transmittance spectra of metasurfaces in the air environment. **a.** The transmittance spectra of g-qBIC metasurface with Q factor of 131. **b.** The transmittance spectra of ε-qBIC metasurface with Q factor of 124.

To compare the intrinsic radiative characteristics of the metasurfaces without environmental influences, transmittance measurements were first conducted in air, as shown in Figure 4.5. The g-qBIC metasurface, featuring geometric asymmetry, exhibits a resonance with a Q factor of 131, while the ε-qBIC metasurface, obtained by permittivity breaking, shows a slightly smaller Q factor of 124. Both spectra were fitted using the TCMT, yielding good agreement

between the experimental data and the fitted curves. The small difference in the Q factors mainly arises from minor variations in the fabricated dimensions and surface roughness, which affect the coupling strength between the resonant mode and free-space radiation. These measurements establish the baseline optical performance in the air environment, providing a direct comparison for the refractive-index-dependent results presented in Figure 4.3.

After validation of the simulation results, the next step is to assess two common sensing readouts: the resonance wavelength shift and the transmittance change at a fixed wavelength. The analysis focuses on determining which signal provides a stronger and more robust response under background noise for the ε-qBIC metasurface.

4.4 Signal robustness of single-wavelength intensity modulation

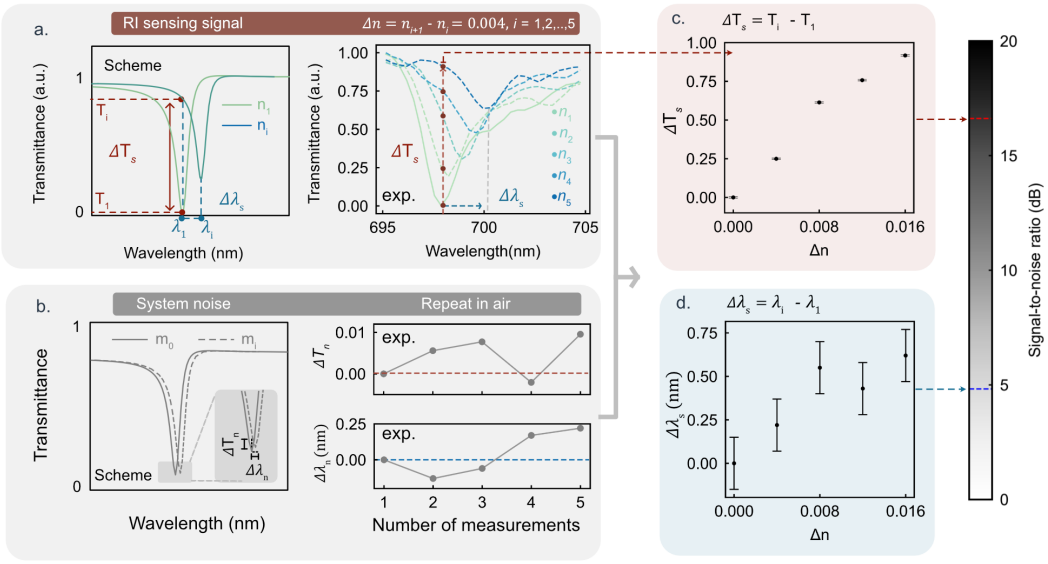

Figure 4.6: Comparative analysis of signal quality between wavelength shift and intensity variation in RI fine sensing. a. Schematic representation of two types of signals used in RI fine sensing, along with normalized experimental spectra. The intensity variation ΔT_s refers to the transmittance difference at a fixed wavelength, while $\Delta\lambda_\mathrm{s}$ denotes the shift in resonance wavelength. Experiments were conducted in five refractive index environments (n_1 to n_5), ranging from 1.386 to 1.402, stepsize $\Delta n = 0.004$. **b.** Illustration of system noise, showing small variations in transmittance (ΔT_n) and resonance position ($\Delta\lambda_\mathrm{n}$) based on repeated measurements (m_0 to m_i) under identical air conditions. Quantitative evaluation of noise levels was performed across five repeated measurements on the same ε-qBIC metasurface. **c.–d.** Signal-to-noise ratio (SNR) analysis for ΔT_s and $\Delta\lambda_\mathrm{s}$ based on the extracted signals in (a). Error bars represent the experimentally determined system noise. The signal ΔT_s exhibits a significantly higher SNR, indicating better robustness for sensing applications.

To evaluate which of the two available signal channels in the ε-qBIC metasurface, resonance wavelength shift or intensity variation at a fixed wavelength, offers better performance in RI sensing, we conducted a set of high-resolution sensing experiments, by narrowing the refractive index step, to extract the signal-to-noise ratio (SNR) under system noise conditions.

In this experiment, glycerol–water mixtures with refractive indices from 1.386 to 1.402 were prepared in increments of $\Delta n = 0.004$. These five RI values (n_1 to n_5) correspond to the spectra presented in Figure 4.6a. To highlight the relative changes between spectra, the transmission spectrum from the first measurement (n_1) was taken as a reference. Its maximum and minimum values were normalized to 1 and 0, respectively, so that all subsequent spectra could be compared on the same scale. This normalization preserves the overall spectral shape while enabling the relative variations to be clearly observed. For each RI, the transmission spectrum was recorded, and two sensing parameters were extracted. The intensity variation signal ΔT_{s} is defined as the change in transmittance at a fixed probe wavelength, $\Delta T_{\mathrm{s}} = T_i - T_1$, where T_i is the normalized transmittance for the i-th RI. The resonance shift signal $\Delta\lambda_{\mathrm{s}}$ is defined as the change in resonance wavelength, where λ_i represent resonance wavelength extracted from the i-th measurement.

To evaluate the system noise, five repeated measurements in air were performed after each sensing step. Prior to each repetition, the sample was rinsed, dried, and measured under identical conditions, simulating practical scenarios involving sample reuse and capturing typical instrumental and operational fluctuations. The corresponding variations in transmittance (ΔT_{n}) and resonance wavelength ($\Delta\lambda_{\mathrm{n}}$) are presented in the right panel of Figure 4.6b, with a conceptual illustration provided in the left. These repeated measurements were used to quantify the noise levels, which were then incorporated as error bars in the analysis of ΔT_{s} and $\Delta\lambda_{\mathrm{s}}$. As shown in Figure 4.6c, the intensity variation signal exhibits consistently higher SNR values across the tested RI range, exceeding 15 dB. By contrast, the resonance shift signal $\Delta\lambda_{\mathrm{s}}$ also, although above the noise threshold, displays greater fluctuations and a lower average SNR (Figure 4.6d). These results indicate that, when accounting for measurement repetition and associated operational fluctuations, the intensity variation channel provides a more robust signal. In the following section, the advantages of using ΔT_{s} for RI sensing with ε-qBIC metasurfaces are examined in comparison with g-qBIC.

4.5 Higher linearity of ε-qBIC sensing data distribution under single-wavelength detection

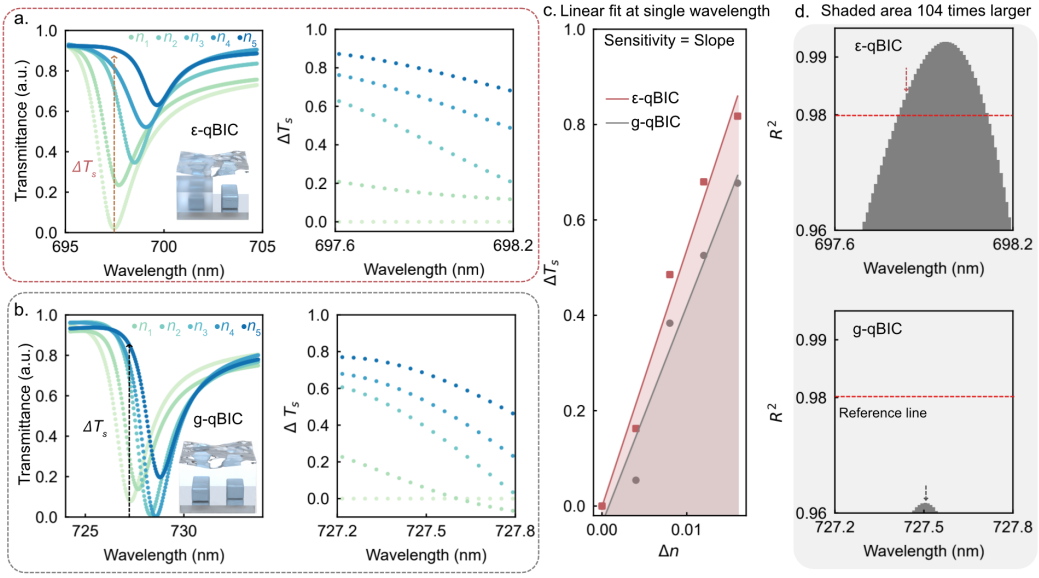

Figure 4.7: Comparison of sensing performance between ε-qBIC and g-qBIC metasurfaces under identical RI conditions. Refractive indices n_1 to n_5 range from 1.386 to 1.402, with a step size of $\Delta n = 0.004$. **a.** Experimental transmittance spectra of the ε-qBIC metasurface under different RI environments, along with the extracted intensity variation signals. **b.** Transmittance spectra and corresponding intensity variation signals for the g-qBIC metasurface under the same RI conditions. **c.** Linear fitting of intensity variation signals at a single representative wavelength, comparing the responses of ε-qBIC and g-qBIC. **d.** R^2 values obtained from linear fitting across multiple wavelengths, used to evaluate the linearity of the intensity variation response. Higher R^2 values indicate better linearity and lower fitting residuals. The ε-qBIC metasurface shows consistently higher R^2 values across a broader wavelength range, indicating enhanced linearity.

To further evaluate the sensing performance of ε-qBIC metasurfaces based on intensity variation signals, we conducted a direct comparison with g-qBIC under identical refractive index conditions (n_1 to n_5, ranging from 1.386 to 1.402 with a step size of $\Delta n = 0.004$). Figure 4.7a and Figure 4.7b show the transmittance spectra and extracted intensity variation signals for ε-qBIC and g-qBIC, respectively.

Linear fitting of the intensity variation ΔT_s across the five RI values at each wavelength was performed. Figure 4.7c compares the fitted results for both metasurfaces at a selected representative wavelength. The slope of each fit corresponds to the sensitivity ($\Delta T_\mathrm{s}/\Delta n$), while the coefficient of determination

R^2 is used to evaluate the fitting quality. The R^2 value is defined as

$$R^2 = 1 - \frac{S_{\mathrm{res}}}{S_{\mathrm{tot}}}, \tag{4.2}$$

where $S_{\mathrm{res}} = \sum(y_i - \hat{y}_i)^2$ is the residual sum of squares between the measured values y_i and the fitted values $\hat{y}_i$, and $S_{\mathrm{tot}} = \sum(y_i - \bar{y})^2$ is the total sum of squares with respect to the mean $\bar{y}$ of all y_i. y_i is the corresponding sensing data ΔT_{s}. A higher R^2 value for a fitting indicates better linearity and lower noise in the signal.

As shown in Figure 4.7c, both ε-qBIC and g-qBIC exhibit high sensitivity in the range of $\sim 5000\%$ / RIU. While some recent studies using metallic sensing structures have demonstrated extremely high spectral resolution[82], the sensitivity values reported in recent works based on dielectric metasurfaces, particularly those employing single-wavelength transmittance variation readout, are typically around 2000% / RIU[69,83,84].

For the g-qBIC, the maximum R^2 observed across the wavelength range is 0.9617, at 727.5 nm. Since none of the wavelengths for g-qBIC reach $R^2 = 0.98$, which is the commonly referenced benchmark[85–87], we selected the highest R^2 point for comparison. In contrast, ε-qBIC achieves a competitive sensitivity ($\sim 5382\%$ / RIU) at a wavelength where $R^2 = 0.9813$, exceeding the 0.98 threshold. This indicates that ε-qBIC not only offers excellent sensitivity but also delivers improved signal quality and linearity.

Moreover, simulations in Figure 4.8 suggest that the sensitivity of ε-qBIC can be further enhanced by adjusting the cladding index n_{cov} to closely match the refractive index of the sensing environment. In such high-Q regimes, even a small RI change can significantly alter the radiative loss channel to zero and restore the ε-qBIC resonance to a BIC, as the metasurface effectively exhibits symmetry both in geometry (identical rods) and in the surrounding dielectric environment. This leads to a sharp transition from a resonant to a non-resonant state. This results in a unity intensity modulation at a fixed wavelength, representing an ideal condition for signal readout in RI sensing applications.

Beyond individual points, we further compared the R^2 distribution across the wavelength range (Figure 4.7d). While g-qBIC fails to exceed the threshold within the range, ε-qBIC consistently maintains R^2 values above it. To quantify the effective linearity window, we applied a relaxed threshold of $R^2 = 0.96$ and

calculated the integrated area between the R^2 curve and the threshold line. The ε-qBIC shows an area approximately 104 times larger than that of the g-qBIC, clearly demonstrating its much broader and more stable sensing window with reduced sensitivity to noise.

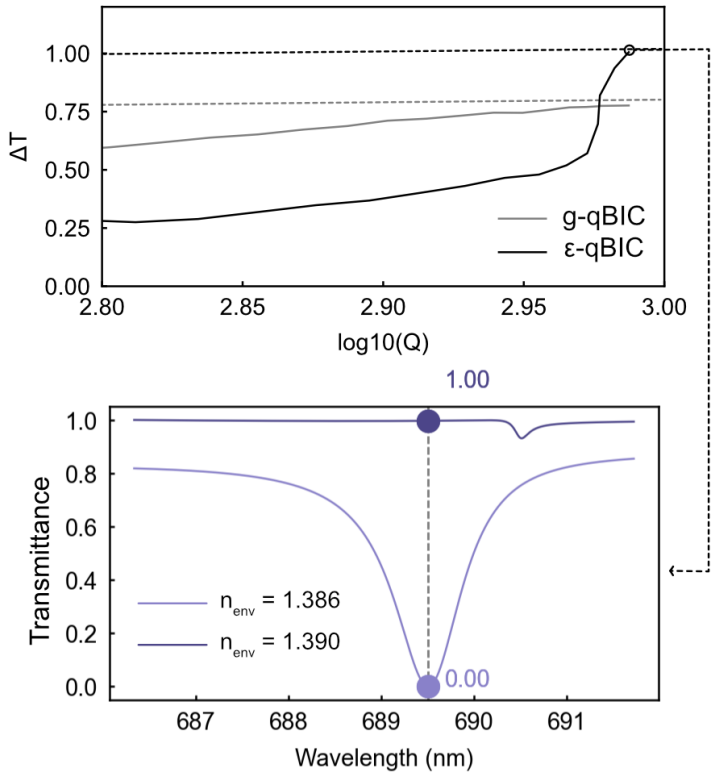

Figure 4.8: Simulation of Q-factor vs intensity modulation response for g-qBIC and ε-qBIC. Simulations were performed to analyze the sensitivity performance of g-qBIC and ε-qBIC structures by sweeping the geometric asymmetry in g-qBIC and the cladding refractive index (n_{cov}) in ε-qBIC. For each configuration, the Q-factor was extracted from the simulated transmittance spectra. Subsequently, the environmental refractive index was varied from 1.386 to 1.390 ($\Delta n = 0.004$) to evaluate the corresponding intensity modulation signal ΔT at a fixed wavelength. The results show that in ε-qBIC, when n_{cov} is tuned to closely match the surrounding environment, the system enters a high-Q regime where even a small RI change can strongly affect the radiative loss channel. When n_{cov} equals the environmental index, the ε-qBIC resonance can be even restored into a BIC. This leads to an abrupt transition from a resonant to a non-resonant state, producing a unity modulation depth. In contrast, the ΔT signal in g-qBIC saturates at approximately 0.77.

To further investigate the ultimate sensitivity limit of the ε-qBIC metasurface, we performed numerical simulations as illustrated in Figure 4.8. In this analysis, the goal was to explore how the radiative loss channel and intensity modulation depth evolve as the system approaches the high-Q regime. The simulations were carried out by systematically varying the geometric asymmetry in g-qBIC and the cladding refractive index n_{cov} in ε-qBIC structures. For each configuration, the

corresponding Q-factor was extracted from the simulated transmittance spectra, and the environmental refractive index n_{env} was subsequently tuned from 1.386 to 1.390 ($\Delta n = 0.004$) to evaluate the resulting transmittance modulation ΔT at a fixed wavelength.

The results reveal that the ε-qBIC configuration exhibits an extraordinary sensitivity enhancement when the cladding index n_{cov} is tuned to closely match the surrounding refractive index. In this critical condition, the system transitions into a high-Q regime where even a minute variation in n_{env} drastically alters the radiative coupling, effectively restoring the ε-qBIC to a BIC. This transition produces a near-unity intensity modulation at a single probe wavelength, corresponding to a complete suppression of radiative loss. In contrast, the g-qBIC shows only a limited modulation depth that saturates around 0.77, even under the same environmental perturbation. These findings indicate that the ε-qBIC metasurface possesses a tunable path toward zero-radiation coupling, representing an intrinsic upper limit of sensitivity defined by the critical condition of permittivity-matched symmetry restoration.

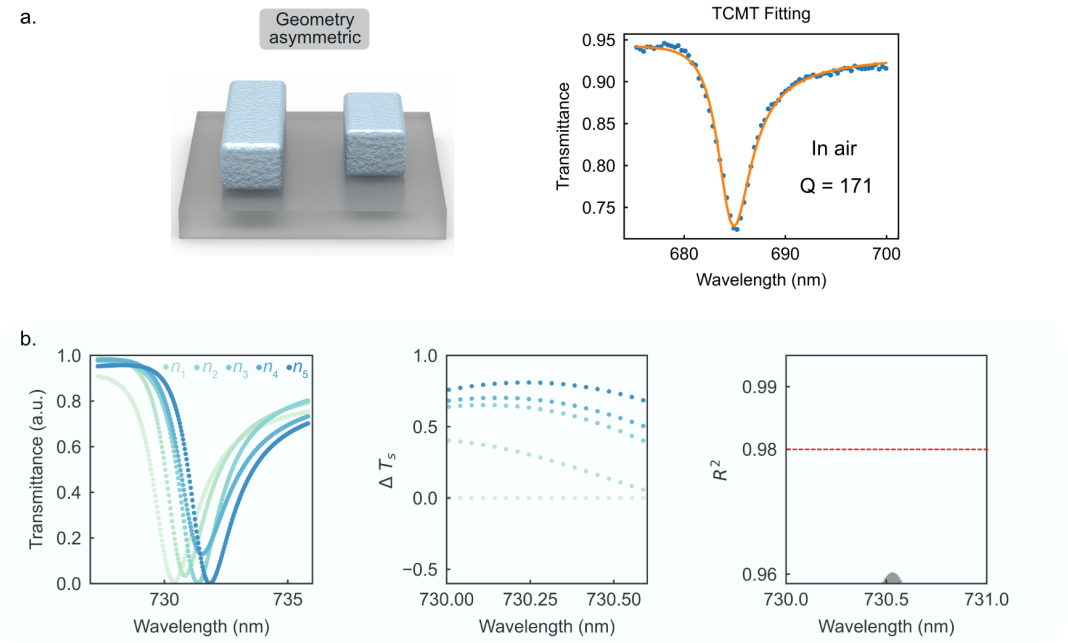

Figure 4.9: RI sensing with a g-qBIC metasurface of initial Q-factor 171 in air. a. Left: schematic of the geometry-broken metasurface. Right: experimental spectrum in air with TCMT fitting, yielding a Q-factor of 171. **b.** Left: transmission spectra measured under different refractive indices (n_1 to n_5, ranging from 1.386 to 1.402 with a step size of $\Delta n = 0.004$). Middle: spectral differences relative to the first spectrum, processed in the same way as in the main text. Right: R^2 values obtained from linear fitting across multiple wavelengths, used to evaluate the linearity of the single-wavelength intensity variation response.

To further verify the conclusions drawn from Figure 4.7, we performed an additional experiment using a g-qBIC metasurface with a higher initial Q-factor to determine whether the R^2 value of the g-qBIC response remains below 0.98. This additional experiment was conducted to further examine the spectral fluctuations observed in Figure 4.7b. While the spectra in Figure 4.7b exhibited noticeable fluctuations that may originate from disturbances in the measurement process (e.g., light source intensity variations), the spectra here show a relatively more stable response. Nevertheless, after applying the same data processing procedure, single-wavelength differential analysis followed by linear fitting, the R^2 distribution still reaches only about 0.96 at maximum, consistent with the result of g-qBIC in Figure 4.7d of the main text and well below 0.98. This confirms that the limited R^2 values are mainly related to the intrinsic behavior of the g-qBIC response under single-wavelength differential sensing.

4.6 Permittivity-restored symmetry-protected BIC

We demonstrate that g-qBIC can be optically restored to a close-to-BIC state by applying a compensating permittivity asymmetry. Specifically, the simulations start from a structure with the same period, resonator height, and width as used in Figure 4.1. The initial configuration is a symmetric geometry with equal rod lengths ($L_1 = L_2 = 320$ nm), as shown on the right side of Figure 4.10a. In this case, the effective dipole moments (p_1 and p_2) cancel each other, resulting in a decoupled state with no resonance observable in the transmittance spectrum.

Next, by decreasing the length of L_1, we break the in-plane symmetry, resulting in a nonzero net dipole moment. This leads to a radiative qBIC mode that becomes observable as a resonance peak in the spectrum.

We then fix the short rod length ($L_1 = 209$ nm) and gradually add a PMMA cladding layer ($n = 1.49$) over that rod, increasing the coverage height H from 0 to 110 nm. This dielectric coating selectively enhances the local permittivity around the short rod, effectively increasing its effective dipole moment p_1. As p_1 approaches p_2 in magnitude but out of phase, the effective total dipole moment of the system approaches zero once again, restoring the destructive interference condition. As a result, the system transitions to a new RSP-BIC, and the resonance disappears in the spectrum, as shown in the bottom panel of Figure 4.10a.

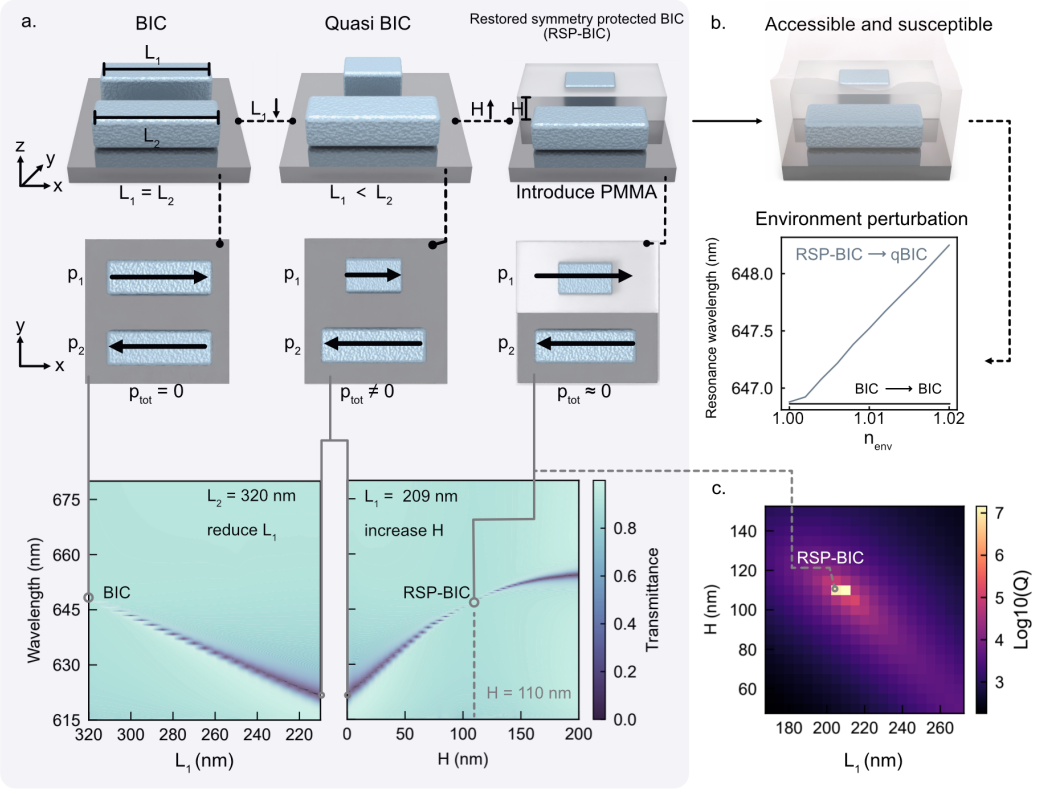

Figure 4.10: Permittivity-controlled restoration of symmetry-protected BICs. a. Conceptual illustration of transformation of g-qBIC into RSP-BIC via environmental permittivity control. Starting from a symmetric structure supporting a BIC (left), introducing a geometric perturbation (shorter L_1) breaks the in-plane symmetry and produces a g-qBIC. By selectively covering the shorter resonator with a dielectric layer of refractive index n_{cov}, the permittivity asymmetry compensates the geometric imbalance, restoring the BIC (right) with radiative losses approaching zero. The middle panel illustrates the corresponding electric dipole distributions, while the bottom panel shows the associated transmittance spectra during this process. Simulated transmittance spectra showing the evolution of a BIC under geometric perturbation (L_1) and its recovery via covering the shorter rod ($L_1 = 209$ nm) with growing height H of a dielectric layer ($n_{\mathrm{cov}} = 1.5$). **b.** Transforming of RSP-BIC into radiative qBIC due to immersing the metasurface into environment with n_{env}. In contrast, conventional BICs are optically inaccessible and remain completely isolated from the environment with n_{env}. **c.** Calculated Q-factor map as a function of rod length L_1 and dielectric cover layer height H, demonstrating the condition for RSP-BIC characterized by a Q factor $> 10^7$. This indicates the compensation point where the permittivity asymmetry cancels the geometric perturbation.

To quantify this transition, we extracted the Q-factors from the spectra across a range of L_1 and H values. Figure 4.10c shows the Q-factor map, clearly indicating the region where a RSP-BIC emerges. At this RSP-BIC condition, the Q-factor exceeds 10^7, substantially higher than surrounding regions, confirming that a permittivity-induced compensation can effectively reestablish the BIC condition from a geometrically asymmetric structure.

Crucially, unlike conventional BICs, which are isolated from the external environment and remain intrinsically stable, the RSP-BIC is environmentally accessible. Small changes in the surrounding refractive index can significantly perturb this

balance, driving a transition from the RSP-BIC back to a qBIC. This approach, which leverages environmental RI to reversibly tune the system between RSP-BIC and qBIC, offers a novel mechanism that has not been addressed in prior studies and may open new directions in metasurface-based sensing.

Potential application of the metasurfaces with reversibility between RSP-BIC and qBIC

The reversibility between RSP-BIC and qBIC is essentially achieved by tuning γ_{rad}, which controls the coupling of the resonance to the far field. Compared with the conventional approach of damping resonances through γ_{int}, this mechanism allows direct on/off switching of resonances under conditions of strong field enhancement. Based on this control scheme, several potential applications can be considered.

On/Off Switchable Filters. By tuning γ_{rad}, the mode can be either fully decoupled from the far field ($\gamma_{\mathrm{rad}} \approx 0$, resonance-free state) or strongly coupled ($\gamma_{\mathrm{rad}} > 0$, resonant state). This enables an optical filter with a clear on/off behavior: in the "off" state, the system remains transparent with minimal crosstalk and absorption, while in the "on" state, a strong resonance appears. Such a capability is useful for active optical filtering in photonic circuits.

Simple and practical sensing devices. Permittivity-asymmetry-induced RSP-BIC represents a non-stationary state with respect to the surrounding refractive index. Any change in the environment can induce a transition between RSP-BIC and qBIC, which can be detected as a clear switching of the resonance. When the refractive index of the environment is varied, the permittivity asymmetry between the two rods in the unit cell is modified, directly affecting γ_{rad}. As a result, the system undergoes a transition from a transparent state (RSP-BIC, $\gamma_{\mathrm{rad}} \approx 0$, no coupling to the far field) to a resonant state (qBIC, $\gamma_{\mathrm{rad}} > 0$), leading to a distinct spectral on/off contrast. In the visible regime, for example, the sensor appears transparent in the RSP-BIC regime, while a noticeable color change occurs once the environment drives the system into the qBIC regime. Since this transition is governed by radiative coupling rather than intrinsic loss (γ_{int}), the contrast is stronger than conventional resonance shifts, while still maintaining high Q-factors and strong near-field enhancement.

4.7 Methods

4.7.1 Numerical simulations

Simulations were performed using CST Studio Suite, a commercial finite-element-based solver. The model was configured in the frequency domain with periodic boundary conditions and employed adaptive mesh refinement to ensure convergence. The dielectric functions of TiO_2 and PMMA used in the simulations were obtained from spectroscopic ellipsometry measurements and subsequently imported into CST. For sensing simulations, the background refractive index was varied to simulate changes in the surrounding environment.

4.7.2 Nanofabrication processes

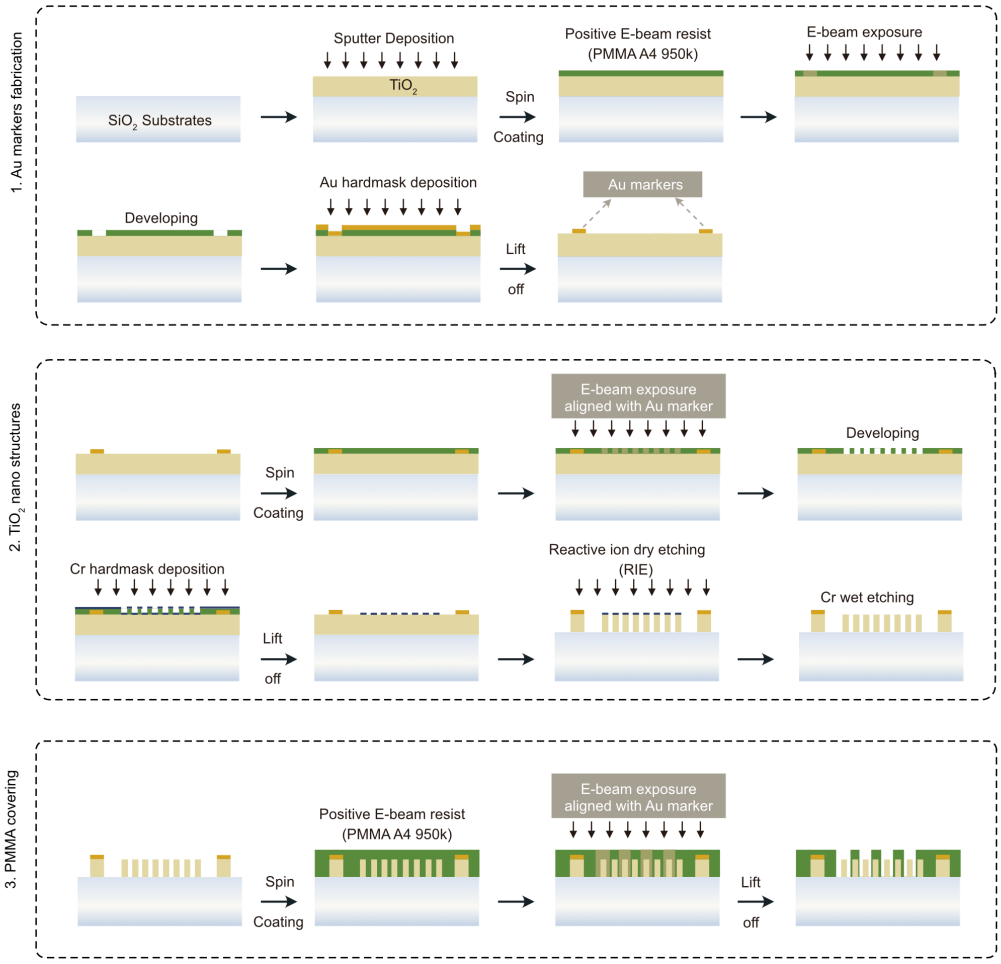

Figure 4.11: Schematic overview of nanofabrication for ε-qBIC metasurface. It includes three main steps, the fabrication of Au marker systems, TiO_2 nanostructures, and selective patterning on PMMA.

Fused silica substrates were first cleaned in an ultrasonic acetone bath, then rinsed with isopropanol (IPA) and treated with oxygen plasma to remove any remaining contaminants. A 110 nm TiO_2 layer was then deposited by sputtering a titanium target in an oxygen-containing plasma (Angstrom Engineering). A layer of PMMA 950k A4 resist was spin-coated and baked at 180 °C for three minutes. To avoid charging during electron beam lithography, a conductive polymer (E-Spacer 300Z) was spin-coated on top of the PMMA.

In the initial patterning step, a 30 nm gold marker system was defined on the TiO_2 film for alignment in the following processes. Using these markers, the second patterning step positioned two-rod nanostructure metasurfaces. After exposure, the sample was developed for 135 s in a 3:1 IPA–MIBK solution. A 50 nm chromium layer was then deposited by e-beam evaporation to serve as a hard mask, and lift-off took place in Microposit Remover 1165 at 80 °C overnight.

The structures were transferred into the TiO_2 layer by RIE in a PlasmaPro 100 ICP-RIE (Oxford Instruments), and the chromium mask was then removed in a wet Cr etchant. In the final patterning step, another PMMA layer was spin-coated and patterned onto the fabricated BIC metasurfaces using the same marker system. The patterned regions were cleaned using the same development protocol.

4.7.3 Optical characterization

Transmittance spectra were measured using a white-light transmission microscope (Witec Alpha Series 300). The samples were illuminated with linearly polarized white light, and the transmitted signal was collected using a $20\times$ immersion objective with a numerical aperture of 0.5. The collected light was coupled into a multimode fiber and directed to a grating-based spectrometer equipped with a silicon CCD detector. All measurements were normalized to their corresponding signal from a bare fused silica substrate.

For the initial sensing experiments in Figure 4.3, commercial refractive index liquids from Cargille Labs (Series: AAA) were used, with refractive indices ranging from $n = 1.30$ to 1.39 in steps of 0.01. To further evaluate the sensing performance in Figure 4.6 and Figure 4.7, additional refractive index liquids were prepared by mixing water and glycerol to obtain a finer range of indices between $n = 1.386$ and 1.414, with an increment of $\Delta n = 0.004$.

4.8 Conclusion

In this chapter, a permittivity-driven qBIC metasurface design is presented, where the environmental refractive index is directly encoded into the system's asymmetry factor, enabling not only the resonance wavelength but also the resonance intensity to vary systematically with the surrounding medium. Under a single-wavelength condition, the intensity variation response with fine RI steps is analyzed. Although both ε-qBIC and g-qBIC exhibit high sensitivity, ε-qBIC demonstrates a considerably broader and more stable linear window across the spectrum, suggesting enhanced robustness and reliability. Importantly, numerical results reveal that permittivity asymmetry can be used not only to generate a qBIC from a symmetric BIC, but also to optically restore a geometrically symmetry-broken qBIC into a new state approaching to BIC with $Q > 10^7$ that remains accessible to environmental changes. Unlike conventional BICs, this RSP-BIC is responsive to RI variations and represents an optical state between non-radiative and radiative regimes, broadening the design space for BIC-based photonics, offering a versatile framework for high-Q devices that merge fundamental control over light–matter interaction with practical sensing capabilities.

5

Polarization-independent BIC metasurfaces with high Q-factor and resonance modulation

*The content of this chapter is published in the scientific journal Optics Express (Xingye Yang, Alexander Antonov, Andreas Aigner, Thomas Weber, Yohan Lee, Tao Jiang, Haiyang Hu and Andreas Tittl. Polarization-independent metasurfaces based on bound states in the continuum with high Q-factor and resonance modulation. Optics Express **33**, 15682-15689 (2025), see ref.[88]). As the foundation of the chapter, the peer-reviewed manuscript is used and text elements such as words, sentences, full passages, as well as graphic content and figures, are drawn directly from the publication in accordance with the open-access Optica Publishing Group publication guidelines that allows the reprinting of own contributions in theses and in accordance with the terms of the CC-BY Creative Commons Attribution 4.0 International license http://creativecommons.org/licenses/by/4.0/.*

5.1 Research background

Metasurfaces represent a significant step forward in optical manipulation[10,89]. Traditionally, optical control has relied on bulky lenses and components, however, the advent of metasurfaces has revolutionized this field. With their subwavelength thickness and the use of engineered nanostructures, they allow for precise control over the phase, amplitude, and polarization of light[12,90]. This transition from conventional to flat optics offers distinct advantages, such as compactness, flexibility, and the potential for on-chip integration, expanding the possibilities of optical devices[91–94].

In the field of metasurfaces, the concept of symmetry-protected bound states in the continuum has emerged as a powerful tool for manipulating light[25,30,31,37]. They provide a unique mechanism for manipulating light, offering high-quality resonances that can be leveraged in various optical applications such as strong coupling, sensing, and optical filtering[21,29,75,95–97].

However, most qBIC designs and applications are polarization-dependent, which limits their efficiency in applications where the incident beam is unpolarized. For instance, in sensing and filtering scenarios with unpolarized light sources, polarization-dependent designs waste nearly half of the incident light energy or impose strict conditions on the polarization of incident light[97–100]. This inefficiency highlights the need for polarization-independent qBIC designs, which can more effectively harness light across all polarization states, thereby facilitating the transition from academic research to industrial applications.

Currently, there are two prominent approaches to design polarization-independent qBIC resonances. The first approach places the resonators supporting the qBIC mode in a circular arrangement to obtain polarization invariance and large quality factors (Q factors) exceeding 200[97]. However, these metasurface designs typically exhibit a resonance modulation of only around 10% and face challenges related to their innately low filling factors. Consequently, such radial structures can produce low signal-to-noise ratios in sensing experiments, leading to issues for molecular differentiation. Likewise, their low total absorption compared to 2D arrays may limit their efficiency in harnessing light source energy, e.g., for energy conversion applications.

The most widely used approach for obtaining polarization independence in qBIC systems is based on C_4 symmetric metasurfaces[98–105]. Such C_4-symmetric struc-

tures exhibit polarization invariance due to their four-fold rotational symmetry, ensuring identical responses to all incident polarization states. However, so far, many experimental realizations of polarization-independent qBIC metasurfaces have either focused on obtaining large resonance modulations at the cost of Q factor in the terahertz band[106,107], or have provided generally low resonance modulations, especially when operated in the more fabricationally challenging visible spectrum[98].

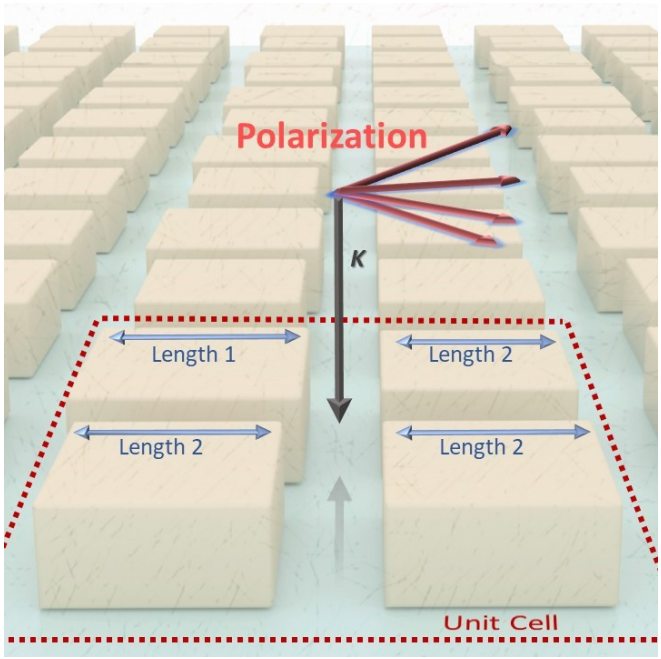

Figure 5.1: Illustration of the metasurface under linearly polarized illumination. Schematic of the metasurface structure investigated in this chapter under different incident linear polarizations.

In this chapter, we present an approach based on C_4 symmetry for achieving a polarization-independent metasurface by simply altering the length difference of square elements within the unit cell (Figure 5.1). This alters the structural periodicity and results in Brillouin zone folding, which changes the distribution of photonic modes in the momentum space, converting a BIC into a qBIC at the Γ point[34,98]. In this way, we realize a qBIC metasurface that simultaneously achieves a high experimental Q factor of approximately 100 and a resonance modulation of around 50%. Our design strikes a balance between Q factor and resonance modulation. The high Q factor offers strong field confinement, making it highly sensitive to the surrounding environment. The strong resonance modulation allows the metasurface to respond effectively to external changes like refractive index without being subjected to noise or minor fluctuations. This well-balanced performance suggests that the resonator could be suitable

for applications such as sensors, modulators, or filters, where sensitivity and stability against loss or noise are both essential.

5.2 Numerical design and analysis to verify qBIC resonances

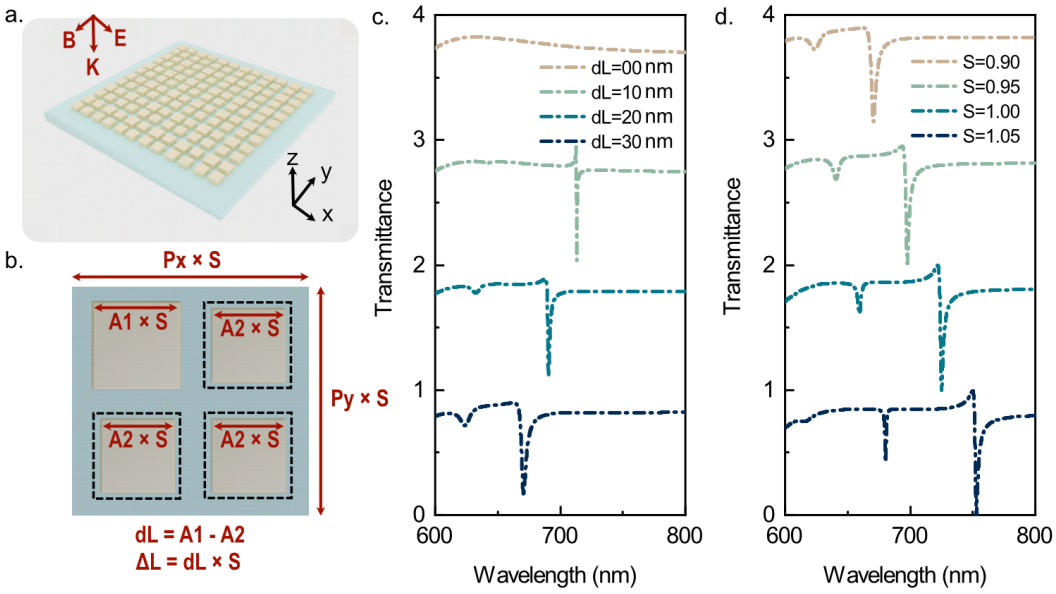

Figure 5.2: Metasurface design and simulated optical response. a. Three-dimensional schematic of the metasurface, showing the Si-based resonators placed on a silica substrate. **b.** Top-view of the unit cell structure, with square-shaped elements having dimensions $P_x = P_y = 430$ nm. The squares are initially identical with side length $A_1 = 185$ nm. To achieve the qBIC resonance, the side lengths of three squares are reduced to A_2, which is smaller than A_1. **c.** Simulated transmittance spectra of the metasurface for varying dL, showing the broadening of the resonance peak with increasing length difference. S is set to 0.9. **d.** Simulated spectra as a function of the scaling factor S with $dL = 30$ nm, demonstrating resonance shift across the spectrum by adjusting the structure size.

Initially, we identified a suitable structure through simulations that achieves the qBIC resonance within the wavelength range accessible for subsequent experimental characterization using CST Studio Suite (*Simulia*). A three-dimensional (3D) illustration of the metasurface is shown in Figure 5.2a, where Si-based resonators are positioned on a silica substrate. Each unit cell has periodicities of $P_x = P_y = 430$ nm and comprises four rectangular blocks, all of which are square-shaped in the top view (Figure 5.2b). In the BIC configuration, these blocks have identical side lengths, denoted as $A_1 = 185$ nm, as indicated by the dashed lines. To achieve the qBIC resonance, we reduce the side lengths of three squares to A_2, thereby introducing an in-plane perturbation, leading to a Brillouin zone folding, which transforms the nonradiative BIC into a qBIC mode.

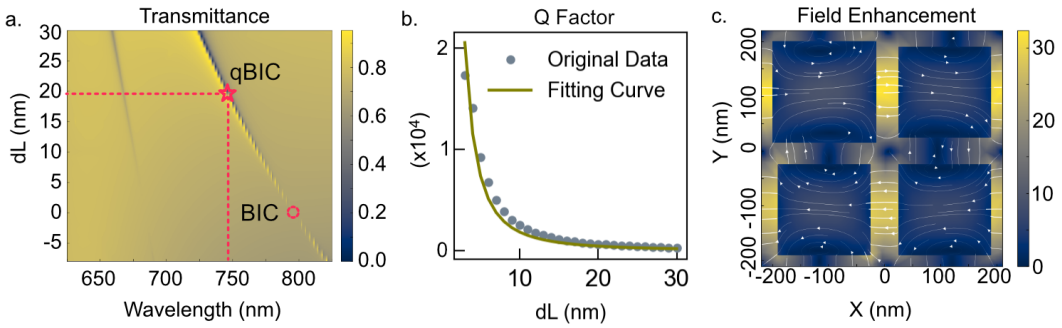

Figure 5.3: Simulated transmittance spectra and field distributions of the metasurface. a. Simulated transmittance spectra for $S = 1$ with dL varying from -10 to 30 nm. **b.** Q factor of the resonance peak as a function of dL, showing the characteristic inverse square relationship with dL. **c.** Electric field distribution in the xy-plane at the middle cut of the bricks, illustrating the field distribution and enhancement, corresponding to the qBIC resonance with $S = 1$ and $dL = 20$ nm marked by red star shape in Figure 5.3a.

Meanwhile, the whole metasurface retains C_4 symmetry, making the resonance polarization-independent.

The perturbation parameter dL represents the difference $dL = A_1 - A_2$, and its range is set from 0 nm to 30 nm. Building on this, we can scale the size of dL by multiplying it with a scaling factor $\Delta L = dL \times S$, which is the final length difference at different scaling parameters. The scaling factor S is introduced to uniformly adjust the size of the structure in the xy-plane. When the scaling factor S is adjusted, it is applied to multiple structural parameters, including the periods P_x and P_y, as well as the dimensions A_1, A_2, and dL, ensuring that the structure in the xy-plane scales uniformly. The resonator height is fixed at 80 nm. Here, for example, in Figure 5.2c, the scaling factor S is 0.9, meaning the actual length difference, as shown in Figure 5.2b, is calculated as $\Delta L = dL \times 0.9$. For the sake of convenient parameter comparison, we use dL for labeling in the figures and the text. At the same time, we provide the corresponding S values to ensure rigor and clarity. The same way is applied in the subsequent sections as well.

By introducing dL, we change the metasurface period from $P_x/2$ to P_x. First, we introduce the perturbation of length difference and obtain the qBIC resonance (Figure 5.2c). Here clearly illustrate the characteristics of the qBIC: S is set to 0.9. As dL increases, more energy couples into the radiation channel, resulting in a broader linewidth. With dL fixed at 30 nm, adjusting the scaling factor allows us for flexible tuning of the resonance position in the spectrum (Figure 5.2d). These simulations in Figure 5.2 successfully demonstrate the desired qBIC resonance.

Next step is to analyze our qBIC resonance. We clearly observe how BIC (red dashed circle) turns into qBIC when changing perturbation parameter dL. Transmittance spectra for $S = 1$ and dL varying from -10 to 30 nm are simulated (Figure 5.3a). An additional resonance feature can be observed at a wavelength of 675 nm. However, due to its weak amplitude and spectral separation from the main BIC resonance, we will not focus on this mode in our subsequent analysis. For the resonance peak with the greater modulation, we extracted the Q factor for each dL using TCMT[41,108], as shown in Figure 5.3b.

The corresponding equations can be seen in chapter 3. The Q factor exhibits an inverse square relationship with the perturbation parameter dL, according to the general rule of qBIC resonance (Figure 5.3b)[37]. We then select a representative resonance peak at $dL = 20$ nm for further analysis (marked by the red star shape in Figure 5.3a), performing a multipolar expansion with the incident light polarized in the x-direction (see in the following mechanism section Figure 5.4)[40,109–111]. We can also choose other parameters, since this doesn't influence the following analysis.

The expansion of the coupling parameter includes electric dipole, magnetic dipole, electric quadrupole, magnetic quadrupole, and electric octupole moments. By evaluating each term of the expansion we revealed that the magnetic quadrupole contributes predominantly, which is consistent with the simulation from previous work[99]. Last, electric field distribution in the xy-plane and the field enhancement factor are analyzed for the representative resonance (marked by the red star shape in Figure 5.3a). The analysis reveals an enhancement exceeding 30 times, indicating the structure's potential for sensing applications (Figure 5.3c). The direction of the electric field of the upper and lower parts are in different directions. Due to the introduction of in-plane perturbation of the adjacent length difference of the squares, they can no longer compensate each other, resulting in a qBIC resonance accessible from the far field.

5.3 Investigation of eigenmode and polarization independence mechanism

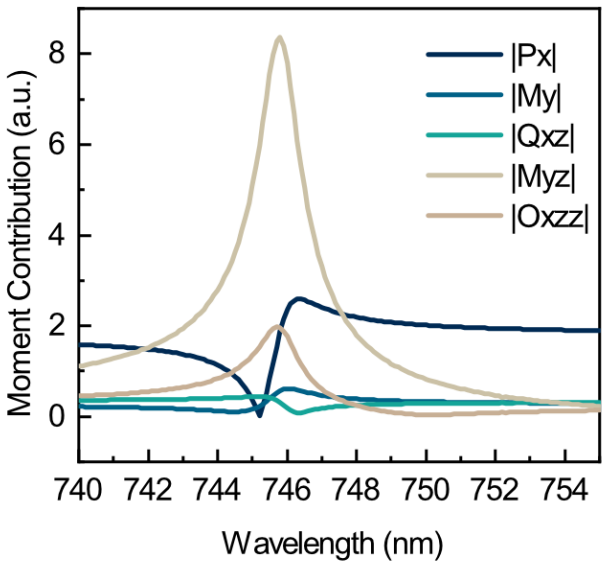

Figure 5.4: Multipolar expansion analysis. Multipolar expansion analysisof the resonance at $S = 1$ and $dL = 20$ nm for the x-polarized incident light, including contributions from electric dipole (P_x), magnetic dipole (M_y), electric quadrupole (Q_{xz}), magnetic quadrupole (M_{yz}), and electric octupole moments (O_{xzz}).

To gain deeper insight into the qBIC resonance (shown in Figure 5.3a), we performed a multipole decomposition analysis, as illustrated in Figure 5.4. This analysis allows us to identify the dominant contributions from various multipolar components, including the electric dipole, magnetic dipole, electric quadrupole, and magnetic quadrupole moments.

The coupling coefficient of the eigenstate with the normally incident light along the z-direction, having a wave vector $\mathbf{k} = \omega/c$ and a linear polarization along $\mathbf{e} = \mathbf{e_x}$, can be evaluated through an overlap integral[40,110]. It can be expressed as

$$m_e \propto \int_V \mathbf{J}(\mathbf{r}) \cdot \mathbf{e}\, e^{i\mathbf{k}\cdot\mathbf{r}}\, dV \propto P_x + \frac{1}{c} M_y - \frac{i\omega}{6c} Q_{xz} - \frac{i\omega^2}{2c} M_{yz} - \frac{\omega^2}{6c^2} O_{xzz}, \qquad (5.1)$$

where P_x, M_y, Q_{xz}, M_{yz}, and O_{xzz} represent the electric dipole, magnetic dipole, electric quadrupole, magnetic quadrupole, and electric octupole moments, respectively. These multipole moments are introduced in a standard way[111] as

$$\mathbf{P} = \frac{i}{\omega}\int_V \mathbf{J}(\mathbf{r})\,dV, \tag{5.2}$$

$$\mathbf{M} = \frac{1}{2}\int_V \mathbf{r}\times\mathbf{J}(\mathbf{r})\,dV, \tag{5.3}$$

$$Q_{\alpha\beta} = \frac{3i}{\omega}\int_V \left[r_\alpha J_\beta(\mathbf{r}) + r_\beta J_\alpha(\mathbf{r}) - \frac{2}{3}\delta_{\alpha\beta}\mathbf{r}\cdot\mathbf{J}(\mathbf{r})\right] dV, \tag{5.4}$$

$$M_{\alpha\beta} = \frac{1}{3}\int_V \left[(\mathbf{r}\times\mathbf{J}(\mathbf{r}))_\alpha\, r_\beta - r_\alpha\,(\mathbf{r}\times\mathbf{J}(\mathbf{r}))_\beta\right] dV, \tag{5.5}$$

$$O_{\alpha\beta\gamma} = \frac{i}{\omega}\int_V \left[\nu_\alpha r_\beta\gamma_\gamma + r_\alpha r_\beta\gamma_\gamma\right] dV - \delta_{\alpha\beta}V_\gamma - \delta_{\beta\gamma}V_\alpha - \delta_{\alpha\gamma}V_\beta, \tag{5.6}$$

$$V_\alpha = \frac{1}{5}\int_V \left[2(\mathbf{r}\cdot\mathbf{J}(\mathbf{r}))r_\alpha + r^2 J_\alpha\right] dV. \tag{5.7}$$

The absolute value of each term in Equation 5.1 is calculated to evaluate and compare the relative contribution of each multipolar component to the overall coupling strength. This quantitative multipolar analysis provides insights into the dominant physical mechanism responsible for the observed qBIC resonance shown in Figure 5.3a. We can see that the magnetic quadrupole contributes predominantly at the resonance position, confirming that the qBIC mode is mainly governed by magnetic-type multipolar excitation. After gaining a deeper understanding of the qBIC resonance, we next clarify the origin of the polarization-independent response observed in our metasurface design.

Polarization independence mechanism

To elucidate the origin of the polarization-independent response observed in our metasurface, we analyze the transmission behavior using the $\hat{T}$-matrix formalism. The $\hat{T}$ matrix connects the complex amplitudes of the incident wave $a^T = [a_i, a_j]$ and the transmitted wave $b^T = [b_i, b_j]$, which propagate along the z-axis and possess orthogonal linear polarizations i and j[112]. It can be expressed as

$$\begin{pmatrix} b_i \\ b_j \end{pmatrix} = \begin{pmatrix} t_{ii} & t_{ij} \\ t_{ji} & t_{jj} \end{pmatrix} \begin{pmatrix} a_i \\ a_j \end{pmatrix}, \tag{5.8}$$

where the first and last subscripts of t_{ij} represent the final and initial polarization states, respectively. This matrix effectively describes how the metasurface couples two orthogonal polarization channels during transmission.

For a metasurface exhibiting C_N ($N = 2\pi/\phi$) rotational symmetry around the z-axis, the $\hat{T}$ matrix transforms according to the rotational operation R_ϕ:

$$\hat{T}' = R_\phi^{-1}\hat{T}R_\phi, \tag{5.9}$$

where the rotational matrix R_ϕ is defined as

$$R_\phi = \begin{pmatrix} \cos\phi & -\sin\phi \\ \sin\phi & \cos\phi \end{pmatrix}. \tag{5.10}$$

For the metasurface investigated in this chapter, which possesses C_4 rotational symmetry, substituting $\phi = \pi/2$ yields the transformed transmission matrix:

$$\hat{T}' = R_{\frac{\pi}{2}}^{-1}\hat{T}R_{\frac{\pi}{2}} = \begin{pmatrix} t_{jj} & -t_{ji} \\ -t_{ij} & t_{ii} \end{pmatrix}. \tag{5.11}$$

By equating the original $\hat{T}$ matrix from Equation 5.8 and its transformed version in Equation 5.11, we obtain the general form of the polarization-independent transmission matrix:

$$\hat{T}_0 = \begin{pmatrix} A & B \\ -B & A \end{pmatrix}, \tag{5.12}$$

where $A = t_{ii}$ and $B = t_{ij}$. This symmetric form ensures that the transmission properties remain unchanged under any rotation of the incident polarization state. In other words, for any linearly polarized wave described by the vector $\mathbf{e}_x \cos\theta - \mathbf{e}_y \sin\theta$, the corresponding transmission response remains invariant:

$$\hat{T}_0 = R_\theta^{-1}\hat{T}_0 R_\theta. \tag{5.13}$$

Therefore, the $\hat{T}$-matrix analysis clearly demonstrates that the C_4 rotational symmetry of the metasurface inherently guarantees polarization-independent transmission. This conclusion provides a solid theoretical foundation for understanding the robustness of our qBIC resonance under varying polarization

conditions, which will be further validated through experiments in the next section.

5.4 Experimental realization of qBIC metasurfaces

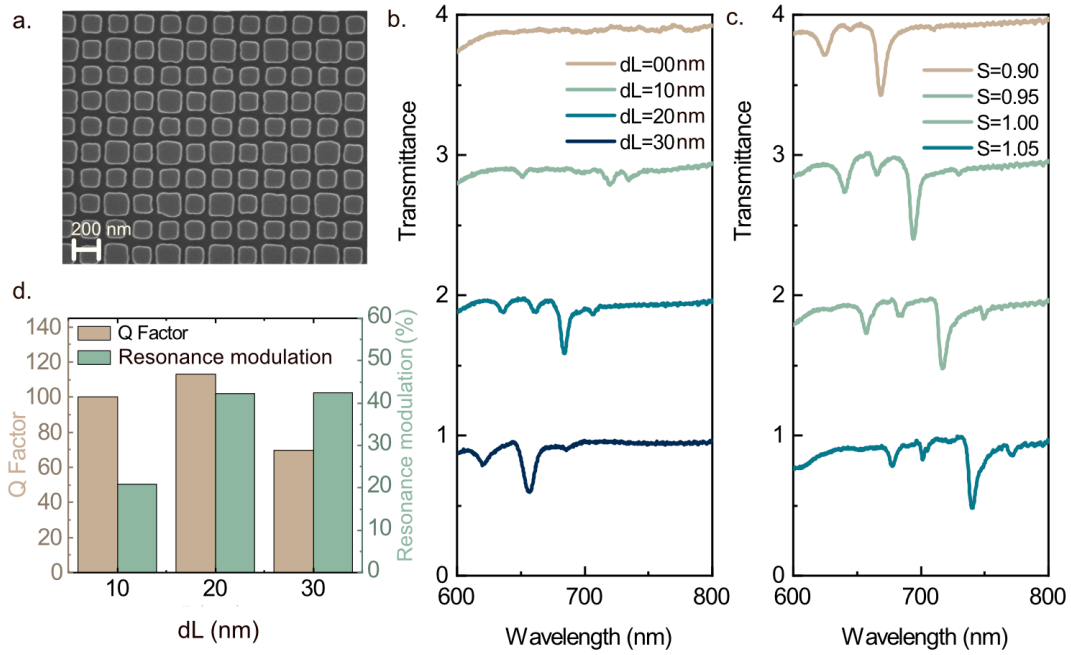

Figure 5.5: Experimental characterization of the fabricated metasurface. a. Scanning Electron Microscope (SEM) image of the fabricated metasurface structure with $S = 0.9$ and $dL = 30$ nm. **b.** Experimental transmittance spectra for $S = 0.9$ and dL ranging from 0 to 30 nm. **c.** Experimental transmittance spectra for $dL = 30$ nm varying scaling factors S from 0.9 to 1.05, demonstrating the redshift of the resonance as the structure size increases, consistent with simulation results. **d.** Q factors and corresponding resonance modulations for resonances with $S = 0.9$ and dL varies from 10 to 30 nm.

We fabricated the designed nanostructures using a top-down approach with E-beam lithography and characterized the fabrication results, transmittance spectra, and Q factors. The fabricated structure with $dL = 30$ nm and $S = 0.9$ was examined under SEM imaging, where the expected structure is clearly shown in Figure 5.5a. We measured the transmittance spectra for dL ranging from 0 to 30 nm with $S = 0.9$. As dL increases, the transmittance exhibits a spectral shift similar to that observed in simulations (Figure 5.2c and Figure 5.5b). We noticed that, in the experiment, two additional resonances with smaller amplitudes appeared on either side of the main resonance peak. This phenomenon is attributed to a slight deviation in the incident angle within our experimental setup, which will be discussed in the next section. We focused on the second

resonance peak from the right in the spectrum, as its resonance modulation varies significantly with changes in dL.

When the scaling factor S is adjusted from 0.9 to 1.05, the structure enlarges, and the transmittance dip redshifts (Figure 5.5c), which aligns well with the simulation trends. Consequently, we successfully fabricated a metasurface with C_4 symmetry, and the experimental results are consistent with the simulated data. Additionally, using the TCMT model, we extracted the Q factor and resonance modulation for the resonance peak at $S = 0.9$ and dL varying from 10 to 30 nm. Theoretically, the Q factor should become higher at $dL = 10$ nm; however, due to fabrication-induced variations in resonator geometry and surface roughness, further enhancement of the Q factor was limited, stabilizing around 100. At $dL = 20$ nm, the Q factor reached 110 with a resonance modulation exceeding 40%. As dL increased further, the Q factor decreased, consistent with the trend observed in simulation (Figure 5.5d).

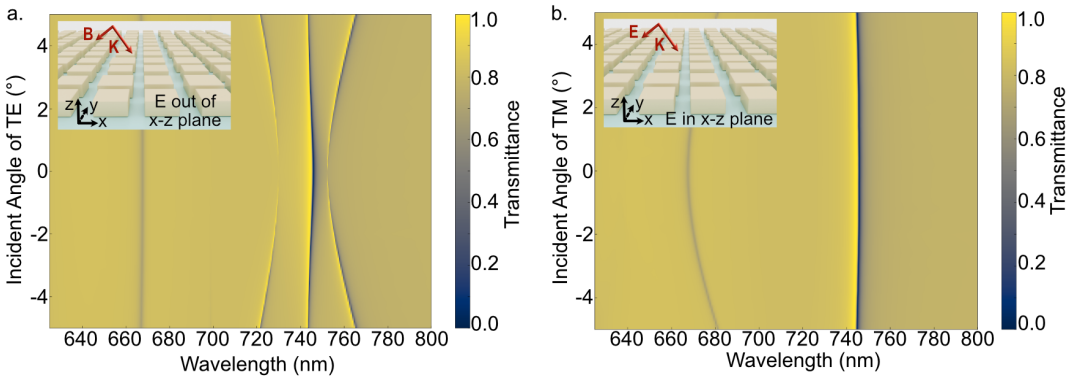

Figure 5.6: Transmittance spectra of oblique incidence for TE and TM polarizations. **a.** Transmittance spectra of oblique incident TE-polarized plane waves for polarization-independent qBIC metasurface with $S = 1$ and $dL = 20$ nm. **b.** Transmittance spectra of oblique incident TM-polarized plane waves for the same structure. The continuous redshift of the resonance peak at 660 nm and its broadening are observed for TM-polarized oblique incident waves. Oblique incidence of the TE-polarized light leads to revealing two off-Γ qBIC modes on either side of the main peak at 740 nm.

Intriguingly, we observe that in addition to the resonance of interest, two small additional resonances appeared on either side, which were not present in the simulation results. Through simulations, we determined that this phenomenon was caused by partial oblique incidence of light during the experiment.

To verify this, we simulated the transmittance spectra of TE and TM modes incident at angles ranging from $-5°$ to $+5°$ with $S = 1$ and $dL = 20$ nm. The TM mode under oblique incidence leads to a continuous redshift of the resonance

peak at 660 nm (Figure 5.6b). In the experiment, this continuous shift results in the broadening of the resonance peak. For the TE mode, under oblique incidence, new qBIC modes are introduced off the Γ-point, appearing on either side of the main spectral peak at 740 nm (Figure 5.6a)[27,28]. The combined spectrum of TE and TM modes under oblique incidence causes the mode at 660 nm to broaden and introduces two new qBIC modes around 720 nm and 760 nm, located symmetrically on either side of the main peak at 740 nm.

5.5 Polarization-independent resonances

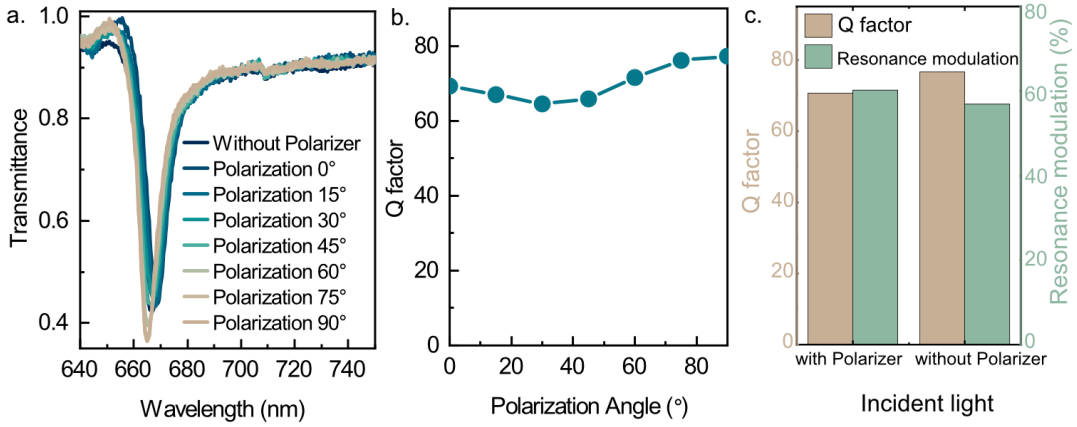

Figure 5.7: Experimental polarization-independent resonance analysis. a. Experimental transmittance spectra of the metasurface with geometry $S = 0.9$ and $dL = 30$ nm, measured for polarization angles from $0°$ to $90°$ in $15°$ increments, along with the spectrum measured without a polarizer. **b.** Q factors extracted from the spectra of different polarization angles. **c.** Comparison of Q factor and resonance modulation with and without the polarizer, showing a Q factor between 70 and 80 and a resonance modulation of approximately 60%, highlighting the high Q factor and strong resonance modulation of the polarization-independent resonance.

Following our numerical and experimental analysis, we conducted polarization-dependent measurements. We selected a metasurface with a geometry of $S = 0.9$ and $dL = 30$ nm, corresponding to the $S = 0.9$ curve in Figure 5.5c. Alternatively, any other experimental spectrum could have been chosen; this particular one only serves as a demonstration of polarization-independent results.

We measured the spectra with the polarization angle ranging from $0°$ to $90°$, in $15°$ increments, as well as the spectrum without a polarizer. The resulting spectra are shown in Figure 5.7a. First, we observe that under different polarization angles, the resonance peak remained fixed around 670 nm, with consistent linewidth and resonance modulation, indicating that both the resonance modulation and Q factor remained stable when polarization changes. The resonance

frequency shows a slight shift of around $5\ \mathrm{nm}$ between 0° and 90°, which may be attributed to fabrication imperfections. However, a more possible factor contributing to this shift is the potential oblique incidence during the measurement process, as discussed in the next figure.

The Q factors of the measured spectra with different polarization angles are extracted and shown in Figure 5.7b. We can see a stable Q factor along different polarization angles. Then we extracted the Q factor and resonance modulation with and without the polarizer (Figure 5.7c). The Q factors range between 70 and 80, with a resonance modulation of approximately 60%. Similarly, depending on specific requirements, we can also select an experimental curve with $dL = 20\ \mathrm{nm}$, where the Q factor is around 110 and the resonance modulation is approximately 40%.

This suggests that our polarization-independent resonance exhibits a high Q factor, indicating good light confinement, and a distinct resonance modulation, offering a better signal-to-noise ratio. Such characteristics could be practically effective in applications like filtering and sensing. Additionally, removing the polarizer allows us to utilize energy from both x- and y-polarized light, thereby improving the ability to efficiently capture the energy incident on the device.

To further investigate the slight resonance shift observed in the polarization-independent resonance during the experiment, we carried out numerical simulations under varying polarization and incidence conditions. Firstly, we performed simulations of the transmittance spectra under normal incidence with varying polarization angles, as shown in Figure 5.8a. The results confirm that the resonance peaks remain fixed, consistent with theoretical expectations for our metasurface design. This supports the conclusion that the design itself does not induce polarization-dependent shifts under ideal conditions.

However, in the experimental spectra, we observed a shift of approximately $5\ \mathrm{nm}$ (Figure 5.7a). While fabrication imperfections could contribute to this, a more reasonable explanation is the influence of slightly tilted incidence. To investigate this, we simulate the transmittance spectra of TE-polarized light incident at angle θ. As shown in Figure 5.8b, for θ varying from 0° to 3°, a resonance shift of around $5\ \mathrm{nm}$ occurs. This result indicates that even a small deviation from normal incidence can induce noticeable spectral shifts. In the experimental setup, if the optical beam is not perfectly aligned and has angular

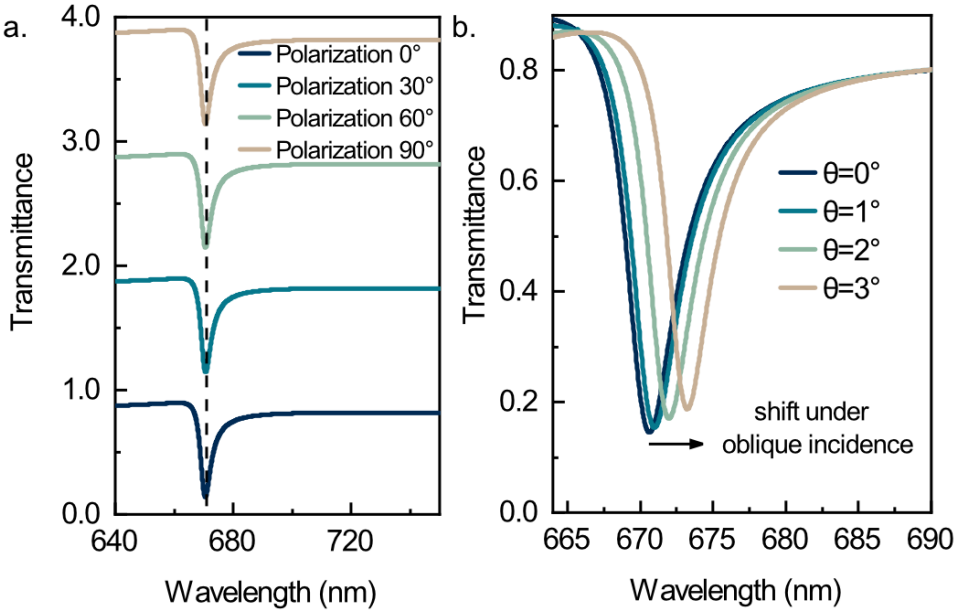

Figure 5.8: Analysis of polarization-independent resonances. a. Transmittance spectra under normal incidence for different polarization angles, that show polarization-independent resonance at a fixed wavelength. **b.** Transmission spectra of TE-polarized light incident at angle θ. Introducing oblique incidence leads to a shift in the resonance position.

spreading, rotating the polarizer changes the effective projection of the beam onto the sample. This can lead to a modest resonance shift, consistent with the experimental observations.

5.6 Methods

5.6.1 Fabrication

The fabrication process began with the thorough cleaning of fused silica substrates. These substrates were subjected to an ultrasonic bath in acetone, followed by rinsing with isopropanol (IPA). To ensure the substrates were free of contaminants, an additional oxygen plasma etching step was performed. Subsequently, an 80 nm thick layer of amorphous silicon (a-Si) was deposited onto the silica substrate at 250°C using plasma-enhanced chemical vapor deposition (PECVD). A resist layer of PMMA 950k A4 was then applied and baked at 180°C for 3 minutes. To prevent charge accumulation during electron beam lithography (EBL), a conductive polymer (E-Spacer 300Z) was deposited on top of the PMMA layer. The nanostructure pattern was defined in the resist using EBL, operating

with an acceleration voltage of 20 kV. After exposure, the resist was developed in a solution of 3:1 isopropanol (IPA) to methyl isobutyl ketone (MIBK) for 2 minutes and 15 seconds. A 50 nm chromium (Cr) layer was subsequently deposited via electron beam evaporation, serving as a hard mask. The metal structures were then lifted off by immersing the substrate in Microposit Remover 1165 at 80°C overnight. The hard mask pattern was transferred into the underlying silicon layer using inductively coupled plasma reactive ion etching (ICP-RIE) with chlorine and fluorine chemistry. The fabrication process was finalized by removing the Cr hard mask through a chromium wet etching.

5.6.2 Optical characterization

The optical characterization of our structures was performed using a commercial white-light transmission microscopy setup (WITec alpha300 series). In this setup, the samples were illuminated with collimated white light from the backside, and the transmitted light was collected using a 50$\times$ objective lens (NA = 0.8). During the measurements, a rotating polarizer was used to cover all polarization directions by adjusting it from 0° to 90°.

5.7 Conclusion

Metasurfaces offer a powerful platform for effective light manipulation, which is crucial for advanced optical technologies. While designs of polarization-independent structures have reduced the need for polarized illumination, they are often limited by either low Q factors or low resonance modulation. Here, we design and experimentally demonstrate a metasurface with polarization-independent qBIC, where the unit cell consists of four silicon squares arranged in a two-dimensional array, and the resonance properties can be controlled by adjusting the edge length difference between different squares. Our metasurface experimentally achieves a Q factor of approximately 100 and a resonance modulation of around 50%. This chapter addresses a common limitation in previous designs, which either achieved high Q factors exceeding 200 with a resonance modulation of less than 10%, leading to challenging signal-to-noise ratio requirements, or achieved strong resonance modulation with Q factors of only around 10, limiting light confinement and fine-tuning capabilities. In contrast, our metasurface ensures that the polarization-independent signal is

sharp and distinct within the system, reducing the demands on signal-to-noise ratio and improving robustness. Experiments show the consistent performance across different polarization angles. This chapter contributes to the development of versatile optical devices, enhancing the potential for the practical application of BIC-based designs in areas such as optical filtering and sensing.

6

Polarization-independent dielectric gradient near-perfect absorbers for aqueous mid-infrared molecular sensing

The content of this chapter is under submission.

6.1 Research background

Biochemical sensing is essential for environmental monitoring, biological research, and pharmaceutical development[14,113,114]. Mid-infrared vibrational spectroscopy provides molecule-specific fingerprint signatures, but the wavelength of these fingerprints is much larger than the molecular dimensions, which weakens the light–matter interaction[29]. Nanophotonic cavities can bridge this mismatch by providing strong, localized field enhancement and spectral overlap with molecular resonances, thereby boosting the sensitivity of label-free detection schemes[115].

For most biologically relevant systems, water is the natural medium: biochemical reactions take place in aqueous environments, cell membranes operate in water, and envisioned point-of-care devices need to work in aqueous backgrounds[116]. However, liquid water exhibits a strong absorption band centered at $\sim 1650\,\mathrm{cm}^{-1}$, which damps nearby molecular vibrational features and optical resonances. This makes sensing with nanophotonic devices in water, especially in the mid-IR range where many important vibrational fingerprints lie, particularly challenging.

To circumvent this issue, several strategies have been explored. One approach is to perform sensing in dry conditions[117–119] or to replace $\mathrm{H_2O}$ with $\mathrm{D_2O}$[120,121], whose main absorption band is red-shifted and thus less overlapping with key molecular fingerprints in the mid-IR. However, these methods compromise the natural physiological environment. Dry sensing precludes the study of dynamic processes, while $\mathrm{D_2O}$ exchange can perturb native hydrogen-bonding networks and reaction kinetics, potentially altering the biological system's functionality[122]. Another route is to use metallic nanoresonators[123–125], whose near fields are confined to very small, highly localized volumes. In this case, only a limited fraction of the mode interacts with water. Furthermore, illuminating the structures from the substrate side shortens the optical path through the water layer, thereby reducing the detrimental influence of water absorption[121]. Such metallic platforms have enabled the detection of molecules such as PMMA and even real-time amide I and II signals in $\mathrm{H_2O}$ environments[116].

However, the intrinsic ohmic losses of metals introduce two fundamental limitations. First, they restrict the maximally achievable quality factors (Q, defined as resonance frequency divided by linewidth), leading to broad resonances that are spectrally much wider than the narrow molecular absorption features[126]. In

this case, a single broad resonance is typically aligned to a target vibrational line, and the analyte-induced changes in the integrated spectral response are small and thus require spectrometers and careful normalization, which reduces usability and increases system complexity and cost[29]. Second, ohmic dissipation leads to local thermal heating, with temperatures possibly rising above $\sim 60^{\circ}\mathrm{C}$. Such near-field heating is undesirable for thermally sensitive biomolecules and dynamic reactions that require high powers and long illumination times, limiting the compatibility of metallic nanophotonic platforms with biological systems.

Dielectric nanophotonic sensing platforms can address these limitations. Mie-resonant dielectric resonators are free of ohmic loss, which significantly reduces the intrinsic loss of the photonic cavity and enables high Q factors[48,76,88]. These high Q modes provide strong near-field enhancement and exhibit narrow resonance linewidths. In contrast to metallic platforms that often rely on a single broad resonance as a probe, dielectric metasurfaces can support a series of narrow resonances that span across the molecular fingerprint region. Because of their high Q factors, these resonances are highly sensitive to small changes in the molecular absorption spectrum: vibrational spectrum at different frequencies modulate different resonances with different amplitudes, giving rise to spectral selectivity. The large Q factors also mean that analyte-induced changes in the resonances lead to pronounced variations in the overall spectrum integrated intensity. By spatially distributing these detection resonances, one can form a "barcode", where each pixel encodes the local spectral response through its total intensity. This concept enables image-based spectrometer-less sensing, which greatly improves usability and reduces system complexity[14]. In addition, dielectric cavities avoid the thermal issues associated with ohmic heating, allowing the local temperature to remain essentially constant. Thus, dielectric platforms are preferred when thermal stability of the sensing environment is critical[127], such as temperature-sensitive DNA-RNA hybridization in SARS-CoV-2 virus detection[128], single-molecule thermodynamics[129] and conformational changes of proteins[130].

However, dielectric resonators tend to exhibit more spatially extended near field distributions compared to highly localized plasmonic hotspots, rendering them susceptible to environmental loss. When water is introduced into a dielectric metasurface platform, the strong absorption of water can significantly reduce the resonance strength or even completely wash out the resonances, making sensing in water extremely difficult[131]. To the best of our knowledge, there has

been no demonstration of dielectric metasurface-based sensing in the mid-IR range under an H_2O background.[132133]

In this chapter, we realize a compact dielectric perfect-absorber metasurface by combining a C_4-symmetric unit cell that support qBICs with a dual-gradient design concept[96]. The C_4-symmetric unit cells provide polarization-independent resonances, which can efficiently utilize arbitrary polarizations of incident light and relaxes the illumination requirements[98,100,104]. Within the qBIC framework, a small in-plane perturbation factor (α) offers a convenient mechanism to tune the radiative loss of the dielectric metasurface and thus the Q factors, while a global scaling factor (S) is used to adjust the resonance wavelength. The dual-gradient concept enables us to encode a large number of resonances within a compact footprint[134]. Specifically, we introduce a gradient in radiative loss along the y direction and a resonance wavelength shift along the x direction. On the one hand, this enables our spectral resonances to cover the entire range of molecular vibrational absorption features through the S-factor. On the other hand, a single compact metasurface can incorporate multiple coupling regions simultaneously, including the critical coupling($\gamma_{\mathrm{rad}} = \gamma_{\mathrm{int}}$, maximum absorbance) and under coupling ($\gamma_{\mathrm{rad}} < \gamma_{\mathrm{int}}$) regimes[96]. Among them, the under-coupling region is observed to exhibit the largest analyte-induced absorbance modulation, and is therefore beneficial for molecular sensing[117]. The coexistence of all these regimes on one metasurface significantly simplifies the fabrication process for the subsequent sensing procedure.

Experimentally, we achieve very high absorbance, reaching 0.8 across the wavenumber range 1720 to 1800 cm^{-1}. Surprisingly, the modes are observed to remain robust even at the edge of metasurface, which can be attributed to the more complex near-field distribution of a unit cell[99,102,103,135], whose resonance is collectively supported by y-direction unit cells even when illuminated along x direction. Next, by rotating the incident polarization from 0° (along the x-axis) to 90°, we obtain the same absorbance around 0.8, confirming the polarization-independent response of the metasurface. Analyte sensing further show that the metasurface can detect poly(methyl methacrylate) (PMMA) in air at different polarization angles, resolving its characteristic absorption feature around 1730 cm^{-1} with an absorbance envelope modulation approaching 20%. Finally, we investigate analyte sensing in a H_2O background. Instead of completely immersing the metasurface in water, where the large water volume would strongly absorb and obscure the resonant signal, we allowed the water to recede, measuring the

metasurface response under a thin residual water film. By comparing experimental data with simulations, we estimate the thickness of this residual water layer to be approximately 700 nm. Under this condition, the qBIC resonances persist due to the significantly reduced optical path length through the thin water film. In previous work[121], when the qBIC resonance was placed at around 1800 cm^{-1}, 100 cm^{-1} away from the water absorption, the resonance amplitude was below 0.25 and upon approaching the region of high water absorption, the qBIC resonance was almost completely suppressed, making molecular sensing in H_2O background impossible. By contrast, due to the thin residual water film, resonance signal can be maintained near 0.5 across 1675–1792 cm^{-1} near the prominent water absorption peak. As a result, PMMA-induced spectral selective modulation remains sufficient, enabling the identification of the characteristic PMMA absorption resonance. Interestingly, this thin residual water film does not disappear immediately but remains stable for around 180 s on the surface of the sample, which gives a time window to perform sensing in a water background. For a PMMA layer of about 7 nm thickness, we demonstrate, for the first time to our knowledge, sensing with dielectric metasurface under a water absorption background spectrum. By normalizing the absorbance spectral envelope to a reference envelope (without PMMA), we obtain a clear PMMA characteristic resonance with its modulation exceeding 30%.

Our work extends the applicability of dielectric metasurfaces and proposes a new approach that can be further explored. In future implementations, this approach could be combined with microfluidics to achieve more stable control of the system, for example, by flowing humidified N_2 after the formation of the residual film to slow down evaporation and thereby obtain a more stable and better-defined water layer on the surface. At the same time, the dual-gradient dielectric metasurface, with its spatially distributed resonances and spectral selectivity, can in principle be interfaced with image-based spectrometer-less readout schemes, which can open up opportunities for combining such sensors with AI-based molecular pattern recognition. The polarization-independent design is beneficial for relaxing illumination requirements and may help reduce the overall complexity and cost of the sensing system.

6.2 Design of dielectric polarization-independent gradient near-perfect-absorber metasurfaces

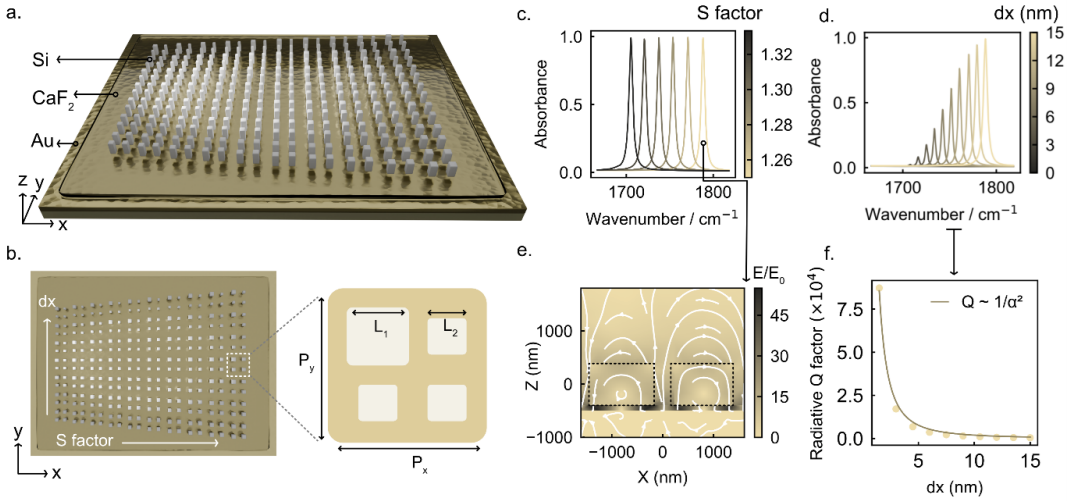

Figure 6.1: Design of the polarization-independent dual-gradient Si metasurface perfect absorber. a. Schematic of the multilayer structure consisting of a 200 nm Au back reflector, a 100 nm CaF_2 spacer, and Si nanoresonators (height: 800 nm). **b.** Unit cell geometry featuring four dielectric square blocks, with one block defined by L_1 and the remaining three by L_2, where $d_x = L_1 - L_2$ denotes the geometric perturbation. A scaling factor S is applied to in-plane dimensions to shift the resonance frequency. The dual-gradient arrangement varies S from 1.00 to 1.33 along the x axis and d_x from 0 to 90 nm along the y axis. **c.** Simulated absorbance spectra $(1 - \text{Reflectance})$ for $d_x = 90$ nm, showing narrowband dielectric resonances with very high absorbance and uniform spectral coverage from 1700 to 1800 cm^{-1}. **d.** Spectra for $S = 1.25$, with d_x varying from 0 to 90 nm with step size 9 nm. **e.** Near-field electric-field distribution $|E/E_0|$ in the X–Z plane for $S = 1.25$ in (c), indicating strong field confinement near the Si resonators and the spacer layer. **f.** Radiative quality factor Q_{rad} as a function of α ($\alpha = d_x \times S$), exhibiting an inverse-quadratic dependence characteristic of qBIC resonances.

We first validated the design of the gradient Si metasurface perfect absorber using CST simulations. As shown in Figure 6.1a, the device is composed of three layers on a substrate: a 200 nm thick Au back reflector, a 100 nm thick CaF_2 spacer layer, and an array of dielectric nanoresonators made of Si with a height of 800 nm. The unit cell design is illustrated in the right panel of Figure 6.1b. The periodicity is $p_x = p_y = 2580$ nm, and each unit cell consists of four blocks. One block has a side length $L_1 = 1020$ nm, while the other three blocks have a side length L_2. The asymmetry is introduced through a perturbation parameter $\alpha = d_x \times S = (L_1 - L_2) \times S$. A scaling factor S is applied to all in-plane dimensions (excluding the height), enabling a uniform spectral shift of the resonance wavelength.

This unit cell is implemented in a dual-gradient configuration, as shown in Figure 6.1b: d_x increases from 0 to 90 nm along the y-axis, while S increases from 1.00 to 1.33 along the x-axis. Despite the weakly perturbed quasi-periodic arrangement, a well-defined resonance is maintained at each unit-cell position, and the variation of geometric parameters results in multiple distinct resonances in a compact footprint. For instance, selecting the row with $d_x = 90\ \mathrm{nm}$ and scanning S from 1.25 to 1.33 yields a series of narrow spectral resonances (with a total Q factor 368), as shown in Figure 6.1c. Due to the absence of ohmic loss in the dielectric resonators, the linewidth remains narrow and the absorbance (defined as $1 - \mathrm{reflectance}$) approaches unity. With increasing S, the resonance wavenumber shifts uniformly from 1700 to 1800 cm^{-1}, indicating effective coverage of the characteristic vibrational band of the target analytes. The near-field distribution of the $S = 1.25$ resonance is shown in Figure 6.1e, where the electric-field enhancement $|E/E_0|$ in the X–Z plane reaches values exceeding 45 times near the resonators and spacer layer, suggesting strong light–matter interaction.

Along with the y-axis gradient, the variation of d_x can be understood within the framework of bound states in the continuum. When $d_x = 0$, the structure supports a BIC with negligible radiative loss. Introducing finite d_x folds the guided modes into the Γ point via Brillouin zone folding, enabling radiation leakage and forming qBIC resonances. As d_x increases, the radiative loss increases, resulting in a lower Q factor and higher mode amplitude, as shown in Figure 6.1d. Extracted radiative Q factors follow an inverse-quadratic dependence on α, consistent with the characteristic behavior of qBICs.

Through this dual-gradient design, we achieve a Si perfect absorber that provides both: (i) spectral coverage of the desired molecular absorption band via in-plane scaling along the x-direction, and (ii) tunable radiative coupling along the y-direction, enabling the coexistence of critical-coupling (perfect absorption) and under-coupled regions on the same metasurface. The latter exhibits stronger analyte-induced absorbance modulation, making it particularly suitable for molecular sensing applications[117].

6.3 Experimental validation of the gradient polarization-independent absorber

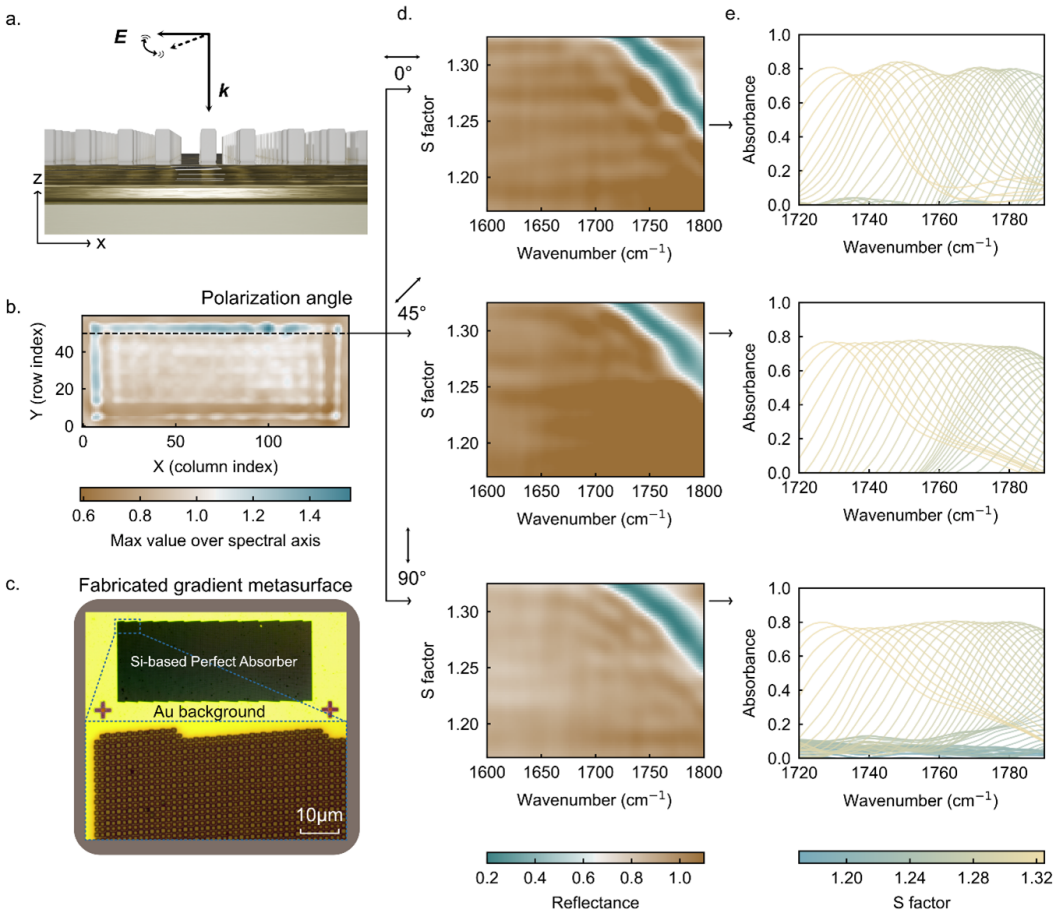

Figure 6.2: Experimental validation of polarization-independent perfect absorption in the dual-gradient Si metasurface. a. Schematic of mid-infrared measurement with normal incidence illumination. **b.** Metasurface in the microscope from an overview. **c.** Microscope image of the fabricated metasurface with a zoom in on the edge area where slight unit-cell misalignment appears due to in-plane scaling. **d.** Two-dimensional reflectance map extracted along the dashed line in (b), where each pixel corresponds to a different scaling factor S. **e.** Experimental absorbance spectra at resonant positions for polarization angles of $0°$, $45°$, and $90°$, demonstrating stable resonances with ~ 0.8 absorbance within 1720–1800 cm^{-1}, confirming polarization-independent near-perfect absorption. The smoother envelopes under $45°$ and $90°$ polarization are attributed to improved unit-cell alignment along the y-direction, enabling better collective mode excitation.

We experimentally fabricated the proposed metasurface using a standard electron-beam lithography process (see Methods) and characterized its response with a mid-infrared hyperspectral microscope (Spero). As illustrated in Figure 6.2a, normally incident light is projected onto the metasurface along the $-z$ direction. The Spero system records an image at each wavenumber using a tunable quantum cascade laser source and reconstructs a hyperspectral datacube (described in chapter 3) containing the full spectral information for each pixel. Figure 6.2b

shows the measured metasurface area, where every pixel provides a complete reflectance spectrum. We extracted spectra along the black dashed line, where each pixel corresponds to a different S factor, and present the results as a two-dimensional (2D) reflectance map in Figure 6.2d. The corresponding absorbance spectra at resonant positions are plotted in Figure 6.2e.

Across the 1720–1800 cm^{-1} range, all extracted spectra reach an absorbance level of 0.8, confirming the experimental realization of a near-perfect absorber. We note that the spectral envelope exhibits slight fluctuations, which we attribute to misalignment near the upper boundary of the gradient metasurface. The applied in-plane scaling introduces position mismatch near the top boundary of the metasurface, where the alignment between adjacent unit cells along the x-direction becomes increasingly difficult to preserve (Figure 6.2c).

Given the C_4 symmetry of the unit cell, we further measured the device response under different polarization angles, including $0°$, $45°$, and $90°$ (upper, middle and bottom panels in Figure 6.2d,e). Under all polarization states, the resonances retain stable amplitudes around 0.8, validating the polarization-independent behavior of the absorber and reducing complexity requirements for the illumination optics in practical deployment and increasing the illumination efficiency by utilizing the full energy of the incident light regardless of polarization angle. We also observe that the spectral envelopes under $45°$ and $90°$ polarization appear smoother. This can be attributed to the high unit-cell alignment along the y-direction, where no positional mismatch is introduced by the perturbation factor α. As a result, resonators within each column couple more efficiently and form a stronger collective mode. Even at the top boundary of the metasurface, the unit cells maintain high absorbance values (~ 0.8) together with improved envelope uniformity.

The preservation of high absorbance near the boundary also indicates a strong robustness of the supported resonance mode. This can be attributed to the excitation of a higher order of magnetic quadrupole eigen mode[88], which exhibits a more complex field distribution and potentially leads to stronger inter-cell coupling compared to a simple anti-parallel dipole.

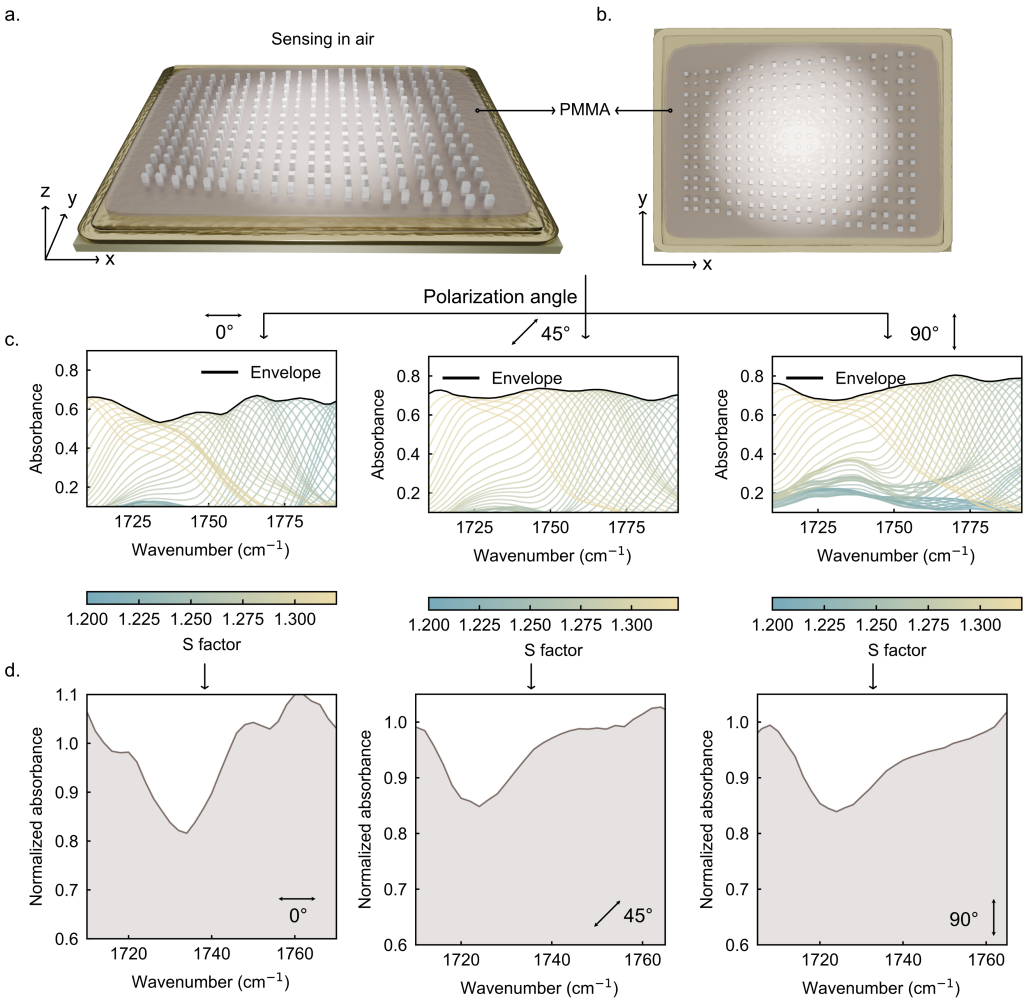

Figure 6.3: Polarization-independent molecular sensing performance of the dual-gradient Si metasurface absorber using PMMA as the analyte. a–b. Schematic of the measurement configuration with a ~ 4 nm PMMA overlayer deposited on the metasurface via spin coating. **c.** Experimental absorbance envelopes extracted along the S-gradient under incident polarization angles of $0°$, $45°$, and $90°$, showing clear perturbations near the PMMA vibrational resonance. **d.** Normalized absorbance envelopes obtained by dividing the PMMA-covered envelopes by their respective bare-device references, demonstrating consistent PMMA signatures with $\sim 20\%$ resonance modulation across all polarization states.

6.4 Polarization-independent sensing

To validate the polarization-independent sensing capability of the dielectric perfect absorber, we selected poly(methyl methacrylate) (PMMA) as an analyte due to its widespread adoption as a benchmark material in optical sensing[108,136,137] and the convenient control of film thickness via spin-coating solutions with different concentrations. A thin PMMA layer of approximately 4 nm was deposited on the metasurface, as illustrated in Figure 6.3a and Figure 6.3b. The structure was then measured in air under three different incident polarization angles ($0°$, $45°$, and $90°$), focusing on the resonance region that overlaps with the

characteristic absorption band of PMMA. Specifically, we extracted spectra from a pixel line slightly below the one used in Figure 6.2b, which corresponds to under-coupled pixels with a lower d_x (lower γ_{rad}) This selected region lies in the under-coupled regime where molecular sensing is more favorable[117] while still maintaining sufficiently strong resonance features. The absorbance spectra along the S-gradient were obtained for each polarization state, and their envelopes were plotted in Figure 6.3c. Pronounced perturbations in the envelopes appear at the PMMA vibrational absorption peak, indicating analyte-induced resonance modulation.

We then normalized these envelopes by referencing them to their respective polarization-matched bare-device envelopes (measured prior to PMMA deposition). The resulting normalized absorbance envelopes are shown in Figure 6.3d. Clear and consistent PMMA signatures with $\sim 20\%$ resonance modulation amplitudes are observed under all polarization angles, demonstrating robust sensing performance. It is noted that for 0°-polarized excitation, the extracted resonance positions and baseline fluctuations show larger deviations than those observed for 45° and 90° excitation. This behavior can be attributed to the geometric scaling inherent to the dual-gradient design, which gradually introduces unit-cell misalignment along the x-direction and therefore reduces the uniformity of inter-cell coupling. In contrast, resonances excited along the y-directed field component are supported by well-aligned unit-cell columns, resulting in more stable resonance positions and amplitudes. Additionally, the PMMA-related resonance retrieved under 45° and 90° excitation exhibit a small red-shift to $\sim 1723\ \mathrm{cm}^{-1}$. This slight variation in the spectral position of the PMMA signature is attributed to the small polarization-induced modulations of the near-field amplitudes associated with the qBIC resonance, which modifies the coupling with the PMMA vibrational mode and leads to a slight change in lineshape due to Fano interference[138]. Nevertheless, the distinct modulation of the normalized absorbance envelopes across all polarization states confirms the sensing potential of this metasurface in polarization-independent applications.

6.5 Sensing in an absorptive water background

We discovered that by immersing the metasurface in water and subsequently allowing the water layer to recede, a thin residual water film remained adsorbed

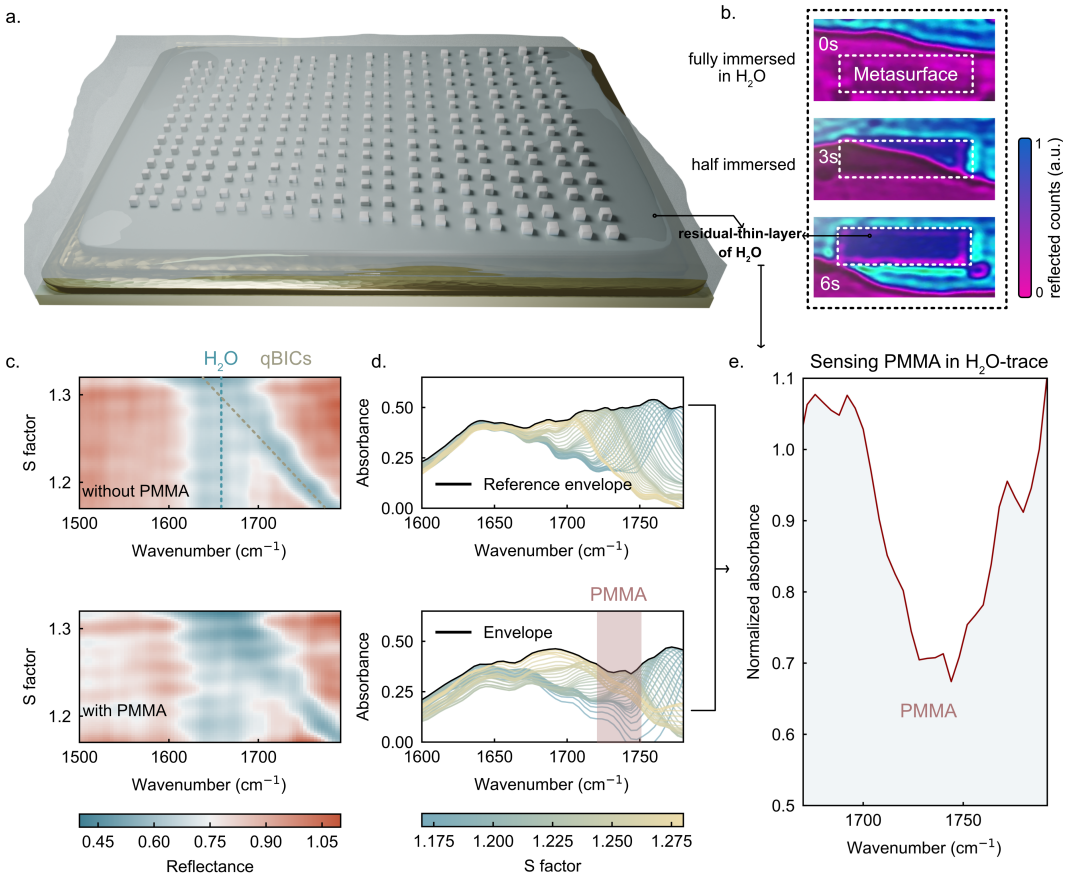

Figure 6.4: Demonstration of PMMA aqueous sensing enabled by a residual thin water film on the dual-gradient Si metasurface. a. Conceptual illustration of the sensing scheme: a bulk water layer is applied and subsequently flows over the metasurface, leaving behind a residual thin water film that enables sensing under a water-background condition. **b.** Top-view experimental snapshots showing the transition from full water immersion (0 s) to partial exposure (3 s) and final emergence (6 s), while a stable thin water film remains on the metasurface surface. **c.** Spectral reflectance colormaps along the S-gradient in the water-film-only reference case (upper panel) and PMMA-coated case (~ 7 nm, lower panel). **d.** Corresponding absorbance envelopes showing persistence of qBIC resonances near the water absorption band (~ 1650 cm^{-1}) with strong amplitude (~ 0.5) across 1675–1792 cm^{-1} and spectral selective modulation by PMMA. **e.** Normalized absorbance envelope obtained by dividing the PMMA-modulated envelope by the water-film-only reference envelope, revealing a clear analyte-induced resonance modulation ($> 30\%$) around the PMMA characteristic vibrational position, confirming mid-IR molecular sensing under a water background.

on the surface, enabling molecular sensing under a water background, as illustrated in Figure 6.4a. The top-view experimental configuration is shown in Figure 6.4b: a droplet of water was dispensed onto the metasurface (a CaF_2 slip was then placed on top to planarize the water layer). At 0 s, the metasurface was fully submerged; the strong water absorption suppressed all resonances. At 3 s, as water evaporated and the waterline receded, the metasurface gradually emerged until it became fully exposed (6 s), while still retaining a thin residual water film, visible through increased reflected counts (bluish purple). This thin film allows vibrational sensing in the presence of water.

We first examined the sensing behavior without PMMA. Figure 6.4c (upper panel) and Figure 6.4d (upper panel) show hyperspectral reflectance colormaps and absorbance envelopes across the S-gradient. Remarkably, the water absorption peak at $\sim 1650\ \mathrm{cm}^{-1}$ (indicated with blue dashed line) coexists with the qBIC resonances (indicated with gold dashed lines) which persist and shift from 1675 to 1800 cm^{-1} as S increases. This indicates that qBICs remain functional near the water-absorption band, maintaining strong resonance amplitude. A consistent absorbance amplitude of ~ 0.5 is maintained across 1675–1792 cm^{-1}, despite slight attenuation near 1650 cm^{-1}. Moreover, the water absorption peak exhibits highly consistent amplitude and spectral position across all S-factor locations, indicating that the residual water film is uniformly distributed over the metasurface. To the best of our knowledge, such coexistence of designed dielectric qBIC resonances with the H_2O absorption band in the mid-IR has not been reported previously.

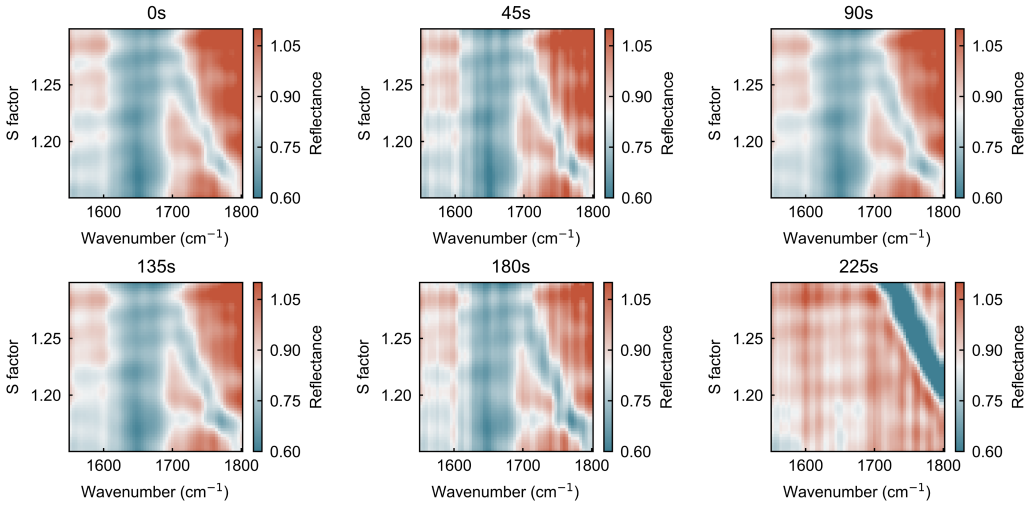

Figure 6.5: Time-resolved optical spectra recorded at different time delays following the formation of a thin water film adsorbed on the metasurface surface. Spectra were acquired at 0, 45, 90, 135, 180, and 225 s under identical experimental conditions. The spectral response shows minimal variation within the first 180 s, indicating that the surface-bound water layer persists over this time interval. At 225 s, the spectral features associated with the water film are no longer observed. These measurements indicate a practical temporal window for optical characterization in the presence of a surface-adsorbed water film.

To evaluate the temporal persistence of the thin water film remaining on the metasurface surface, time-resolved optical measurements were performed after the formation of the surface bound residual water layer. Following the establishment of the water film, optical spectra were repeatedly recorded at defined time intervals of 0, 45, 90, 135, 180, and 225 s under identical experimental conditions. The recorded spectra exhibit minimal variation during the initial

measurement period up to 180 s, indicating that the residual water layer remains present on the surface over this time interval. Later point of 225 s, the spectral response associated with the water film is no longer observed. These observations suggest that the surface bound residual water layer persists over a finite time window before complete evaporation. It should be noted that the persistence of a surface-bound water film depends on the surface properties of the underlying material. In this chapter, the surface properties are defined by the CaF_2 spacer layer employed in the metasurface structure. The existence of a stable surface water film over a time window of approximately 180 s provides sufficient duration for reliable optical measurements under aqueous background conditions. This temporal window enables repeated spectral acquisition and analysis before the complete evaporation of the water layer. The lifetime of the water film could in the future potentially be extended by integrating the metasurface with microfluidic approaches, e.g. by purging the cell chamber with humidified nitrogen, thereby reducing the evaporation rate. These strategies may allow for improved control over the persistence of the residual water layer.

To estimate the residual thin water-film thickness remaining on the metasurface during the experiment, we performed numerical simulations in which the water thickness was varied from 0 to 2400 nm (Figure 6.6a). The simulated absorbance spectra show that increasing water thickness strengthens the water absorption feature, while the qBIC resonance peak is progressively reduced, indicating increasing absorption loss introduced by the water layer. For a quantitative comparison, we extracted two peak amplitudes from each simulated spectrum: (i) the peak amplitude of the water absorption band and (ii) the peak amplitude of the qBIC resonance. The extracted peak amplitudes are plotted as a function of water thickness in Figure 6.6b. The water-absorption peak amplitude (blue curve) increases in an approximately two-regime manner, with a pronounced rise for water thickness below $\sim 1000\ \mathrm{nm}$, followed by a transition region and a continued increase at larger thicknesses. Given that the relevant illumination wavelength is $\sim 6\ \mu\mathrm{m}$, this behavior suggests a crossover from a thin-film regime where near-field interaction is dominant to a regime where the propagating components contribution becomes important as the water thickness grows. On the other hand, the qBIC peak amplitude (brown curve) decreases with increasing water thickness, and the resonance becomes effectively masked by strong water absorption when the water thickness exceeds 1000 nm. Finally, we compared the simulated spectra, together with the extracted peaks of the water-

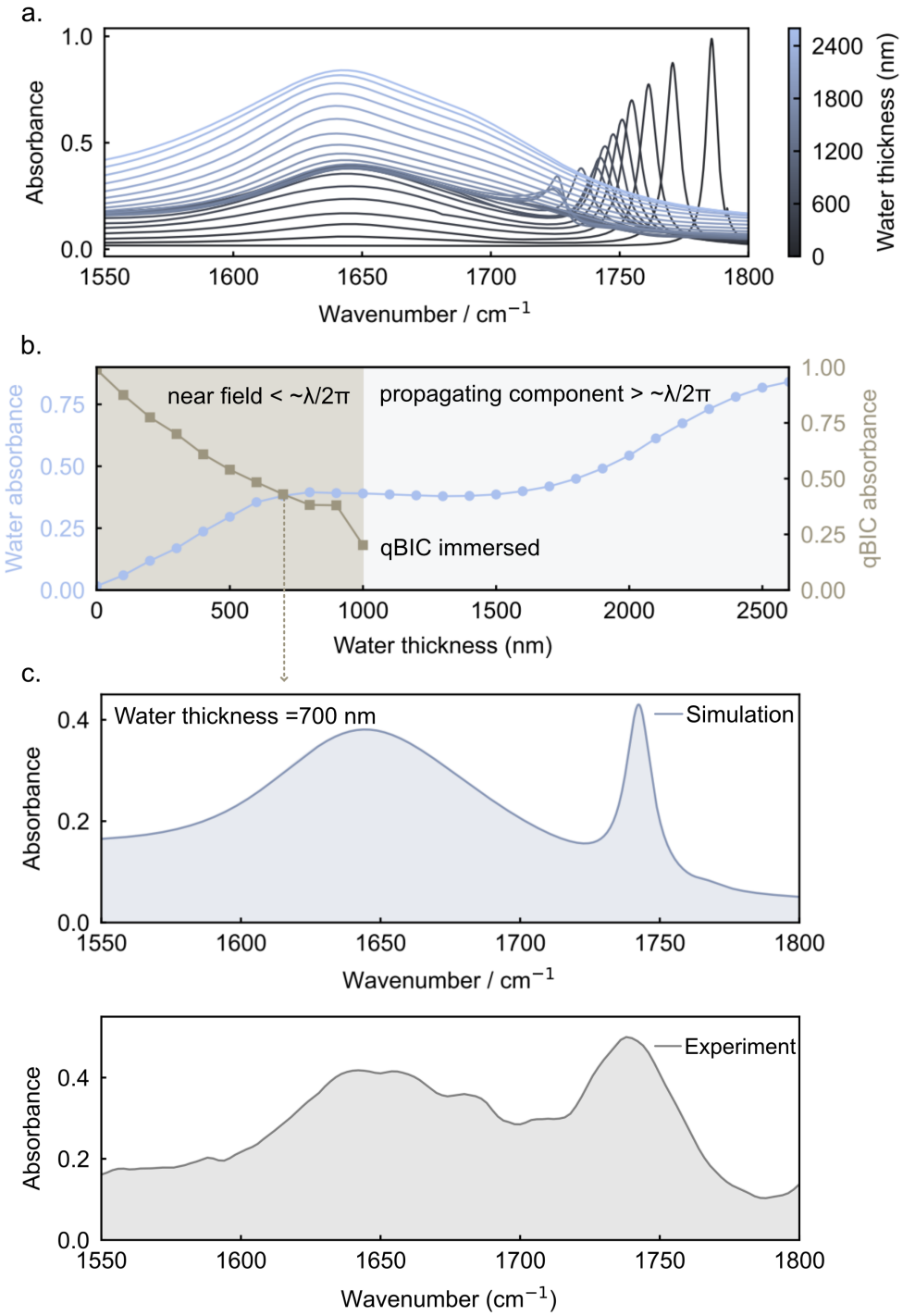

Figure 6.6: Estimation of the residual thin water film thickness on the metasurface. **a.** Simulated absorbance spectra for water thicknesses ranging from 0 to 2400 nm. With increasing water thickness, the water absorption feature becomes stronger, while the qBIC resonance peak is progressively suppressed. **b.** Extracted peak values of the water absorption feature (blue) and the qBIC resonance (brown) as a function of water thickness. The water-absorption peak increases with thickness, while the qBIC peak decreases and becomes strongly suppressed at larger thickness. A change in slope of the water-absorption trend is observed around 1000 nm. **c.** Comparison between the experimental spectrum and selected simulated spectra, indicating a residual water film thickness of $\sim 700\ \mathrm{nm}$ in the experiment.

absorption and the qBIC resonance, to the experimentally measured spectrum (Figure 6.6c). The agreement is obtained for a water thickness of $\sim 700\ \mathrm{nm}$, for which both the water-absorption peak and the remaining qBIC peak best reproduce the experimental observation. Based on this simulation-experiment matching, the residual water-film thickness on the metasurface in the experiment is estimated to be approximately 700 nm.

We then introduced PMMA as the analyte, depositing a $\sim 7\ \mathrm{nm}$ film followed by 10 min UV-ozone treatment to enhance hydrophilicity. The measurement is conducted under the 700 nm residual water film condition, as established earlier, rather than full immersion, producing the resonance signals shown in Figure 6.4c (lower panel) and Figure 6.4d (lower panel). Clear absorbance envelope perturbations appear at the PMMA absorption band (red-highlighted region) together with a clear water absorption band. Upon normalization by the water-only reference envelope, the normalized absorbance shown in Figure 6.4e reveals a strong analyte-induced modulation $> 30\%$ at the PMMA vibrational position. These signatures represent, to our knowledge, the mid-IR detection of PMMA using a dielectric metasurface under a water background, which has not been achieved in prior work.

Our approach expands the applicability of dielectric metasurfaces by enabling a new approach based on the residual thin water-film coverage. Future integration with precise surface hydrophilicity treatment and microfluidics could stabilize and control the water-layer thickness, for example, pumping water through the metasurface chamber leaving residual thin water film, using humidified N_2 to remove the bulky water and slow down the evaporation of residual water layer and thereby obtain a more stable and better-defined water layer on the surface. Furthermore, the spatially distributed resonances and spectral selectivity of dual-gradient architecture allow compatibility with image-based, spectrometer-less sensing platforms, with potential combination with AI-driven molecular identification. Finally, the inherent polarization-independent response reduces optical system complexity and enhances practicality for bio-chemical sensing environments.

6.6 Methods

6.6.1 Numerical simulations

Electromagnetic simulations were carried out using CST Studio Suite (Simulia), a commercial finite-element solver operating in the frequency domain. Periodic boundary conditions were applied and adaptive mesh refinement was enabled to ensure numerical convergence. The CaF_2 substrate was treated as lossless and non-dispersive over the wavelength range of interest, with a constant relative permittivity of $\varepsilon = 1.9$. The real part of the permittivity of amorphous silicon was set to $\varepsilon = 11.9$.

6.6.2 Sample fabrication

A 200 nm gold layer was first deposited onto a silica substrate, followed by the deposition of a 100 nm CaF_2 layer, both using thermal evaporation (Angstrom Engineering). Subsequently, an 800 nm amorphous silicon film was deposited on the CaF_2 layer via plasma-enhanced chemical vapor deposition (PECVD) using a PlasmaPro 100 system (Oxford Instruments). Nanostructuring was performed by spin-coating a 400 nm layer of positive electron-beam resist (ZEP520A, Zeon Corporation), followed by the application of a conductive polymer layer (ESPACER, Showa Denko K.K.). Electron-beam lithography was conducted using an eLINE Plus system (Raith) at an acceleration voltage of 20 kV with a $20\ \mu\mathrm{m}$ aperture. After exposure, the resist was developed in amyl acetate, followed by a methyl isobutyl ketone and isopropyl alcohol (1:9) rinse. A 60 nm chromium layer was then deposited, and lift-off was performed using Microposit Remover 1165 (Microresist). The remaining chromium pattern served as a hard mask for subsequent reactive ion etching, carried out using SF_6 and argon gases. Finally, the chromium mask was removed using TechniEtch Cr01 (MicroChemicals).

6.6.3 Molecular sensing

For molecular sensing experiments, the dual-gradient metasurface was coated with PMMA (495k molecular weight, diluted in anisole) via spin coating at 3000 rpm for 1 min, resulting in a uniform polymer layer. The coated samples were subsequently baked at $180^{\circ}\mathrm{C}$ for 3 min to fully solidify the PMMA film. Between

consecutive measurement cycles, the PMMA layer was removed by sequential immersion in acetone and isopropyl alcohol baths. The thickness of the PMMA films was estimated using a polynomial calibration curve[96]:

$$d = 1.237c^3 + 4.773c^2 + 10.88c + 0.9635,$$

where d denotes the PMMA thickness in nanometers and c represents the PMMA concentration in percent. For sensing measurements performed in air, a PMMA concentration of 0.25% was used, corresponding to a film thickness of approximately 4 nm. For measurements conducted in H_2O, the PMMA concentration was increased to 0.5%, yielding a thickness of approximately 7 nm. The higher concentration was selected to compensate for the reduced hydrophobicity of the PMMA layer following a 10 min UV–ozone treatment, which was applied to improve surface wettability while avoiding complete degradation of the polymer film.

6.7 Conclusion

This chapter presented a dielectric perfect-absorber metasurface platform that leverages qBIC resonances in a C_4-symmetric unit cell combined with a dual-gradient design. The C_4 symmetry ensures polarization-independent operation and thus simplifies the optical excitation configuration. The qBIC framework enables independent tuning of the radiative loss and Q-factor through a controllable in-plane geometric perturbation and the resonance wavelength is continuously shifted by applying a scaling factor within compact dual-gradient design. Experimentally, very high absorbance (> 0.8) is observed from 1720–1800 cm^{-1}. Under varying polarization states ($0°$–$90°$), stable absorption features and consistent sensing performance confirm the polarization-independent characteristics of the device, retrieving clear PMMA (4 nm thickness) absorption signatures near 1730 cm^{-1} with $\sim 20\%$ modulation. Interestingly, we demonstrate mid-infrared molecular sensing under a water-background condition. By utilizing a residual thin water film layer instead of full immersion where conventional dielectric metasurfaces lose spectral information due to strong H_2O absorption, the qBIC resonances remain discernible with an absorbance of ~ 0.5 across 1675–1792 cm^{-1}. This enables the first experimental detection of PMMA using a dielectric metasurface under H_2O absorption background, yielding $> 30\%$ modulation

in the normalized absorbance envelopes. Overall, our approach expands the applicability of dielectric metasurfaces for biochemical analysis, introducing a new approach based on residual thin film water backgrounds. The design is potentially compatible with microfluidics for more stabilized water-layer control, and the spectral selectivity of dielectric platform offer pathways toward imaging-based, spectrometer-less molecular detection with potential AI-assisted analysis. The polarization-independent nature of the device further reduces illumination complexity, suggesting its promise for highly integrated molecular sensing technologies.

7

Conclusion and outlook

This thesis studied qBIC metasurfaces with the aim of making BIC-inspired photonics more usable for practical sensing and mid-IR spectral applications.

In Chapter 3, a permittivity-driven qBIC was developed, where the surrounding refractive index contributes directly to the effective asymmetry factor of the system. This approach enables not only resonance wavelength shifts but also resonance intensity variations with the environment, which is suitable for single-wavelength intensity-based sensing. Experiments demonstrate that the permittivity-driven qBIC provides a broader and more stable linear response window than geometry-driven qBIC for single-wavelength detection. This result indicates a practical advantage of encoding the environment into the asymmetry factor when a simplified readout is desired. In addition, numerical studies indicate that permittivity asymmetry can restore a geometric symmetry breaking qBIC approaching to BIC state with extremely high Q while still remaining responsive to environmental RI changes, which expands the conceptual design space for BIC-related resonances.

Chapter 4 addressed the practical limitations imposed by polarization sensitivity. A polarization-independent qBIC metasurface was designed and experimentally demonstrated using a C_4-symmetric unit cell composed of four silicon squares. By tuning the edge-length difference among the squares, the resonance linewidth and resonance strength could be adjusted in a controlled manner. The device

achieved an experimental Q factor of about 100 together with a resonance modulation of around 50%, and it maintained consistent performance across polarization angles. This polarization-robust behavior reduces constraints on illumination and supports more stable measurements in compact optical systems.

In Chapter 5, the qBIC concept was extended to a dielectric perfect-absorber metasurface platform based on a C_4-symmetric unit cell and a compact dual-gradient design. The platform combines polarization-independent excitation with continuous spectral tuning within a small footprint, and experimentally shows high absorbance (> 0.8) across 1720–1800 cm^{-1}. It enables vibrational sensing of PMMA layers (4 nm) with clear absorption signatures near 1730 cm^{-1} and $\sim 20\%$ modulation. Beyond conventional dry measurements, the thesis further demonstrates mid-IR molecular detection under a water background by using a residual thin water film rather than full immersion, where dielectric metasurface spectra are often strongly obscured by H_2O absorption. In this condition, the qBIC resonances remain discernible and enable retrieval of PMMA (7 nm) signatures with $> 30\%$ modulation in normalized absorbance envelopes. This result suggests a feasible route to extend dielectric metasurface sensing toward water-related environments, while maintaining the key benefit of spectral selectivity.

Overall, the thesis establishes three connected building blocks for practical qBIC metasurface sensing: (i) an experimentally verified intensity-based sensing route with improved linearity enabled by permittivity-driven asymmetry, (ii) polarization-independent qBIC designs that relax illumination constraints and improve robustness, and (iii) a compact absorber platform that supports molecular detection even under strong background absorption by water. Together, these outcomes support qBIC metasurfaces as a versatile and practical dielectric platform for refractive index sensing and mid-IR spectral engineering.

While this thesis demonstrates experimentally practical qBIC metasurface routes for RI and mid-IR sensing, several directions remain open to improve practical applicability, reproducibility and controllability.

(1) Experimental access to the numerically predicted restored-BIC regime.

Chapter 3 numerically indicates that permittivity asymmetry can optically restore a geometric-symmetry breaking qBIC into a BIC-like state with extremely high Q while remaining responsive to environmental RI changes. A natural next step is to design experiments that make this regime accessible, including appropriate

fabrication strategies and measurement protocols that can distinguish linewidth narrowing from instrumental limitations.

(2) Development and deployment of single-wavelength intensity readout.

The thesis already shows, experimentally, that under matched Q conditions the permittivity-driven qBIC offers improved linearity for single-wavelength detection compared with geometry-driven qBIC. Future work can focus on practical aspects that determine usability: long-term drift characterization, referencing methods against source-power fluctuations, and calibration transfer across devices. These efforts would clarify the realistic sensing resolution and stability achievable with intensity-only readout.

(3) Q-factor optimization for application-specific sensing

For polarization-independent metasurfaces and absorber platforms, a key future task is to engineer radiative coupling so that the device remains in a regime that is experimentally readable rather than seeking arbitrarily high Q. This can be supported by systematic links between fabrication statistics and optical performance. Compact layouts that provide multiple usable resonances or multiple coupling regimes on a single chip (for example via gradient concepts) may help investigation under varying conditions.

(4) Stabilizing and quantifying thin-water-film conditions.

The residual thin-water-film approach demonstrated in Chapter 5 enables sensing under a water-absorption background, but further work is needed to make the water layer thickness and lifetime controllable and repeatable. Integrating microfluidics and surface engineering could provide better boundary conditions, while systematic characterization of film dynamics, spatial uniformity, and reproducibility would help turn the current concept into a standardized measurement protocol for water-related sensing.

(5) Broadening applications and strengthening sensing metrics.

Future studies can extend the platform beyond proof-of-principle molecules by introducing selective surface functionalization, testing a wider range of targets, and reporting metrics relevant to sensing deployment, such as repeatability and performance under complex backgrounds. Such work will help identify application scenarios where dielectric qBIC metasurfaces offer the most practical advantages.

(6) System-level integration and simplified readout.

The polarization-independent operation and compact designs motivate simplified optical setups. Future work could explore imaging-based readout and spectrometer-less concepts, potentially combined with data-driven analysis to extract molecular signatures from resonance patterns. In addition, image-based readout could be further combined with AI-assisted analysis to distinguish and categorize different molecular sensing responses.

In summary, this thesis establishes qBIC metasurfaces as a versatile platform for refractive-index and mid-IR sensing, enabling linear single-wavelength readout, polarization-independent operation, and measurements under absorptive water backgrounds. Continued progress in realizing permittivity-restored BIC states, together with more stable system designs and higher levels of integration, could further broaden the practical scope of qBIC-based dielectric photonic systems.

References

[1] A. V. Helden, "The Invention of the Telescope", Transactions of the American Philosophical Society **67**, 1–67 (1977), http://www.jstor.org/stable/1006276 (cited on page 1).

[2] J. C. Mauro and E. D. Zanotto, "Two Centuries of Glass Research: Historical Trends, Current Status, and Grand Challenges for the Future", International Journal of Applied Glass Science **5**, 313–327 (2014), https://ceramics.onlinelibrary.wiley.com/doi/abs/10.1111/ijag.12087 (cited on page 1).

[3] T. Young, "On the theory of light and colours", Philosophical Transactions of the Royal Society of London **92**, 12–48 (1997), https://doi.org/10.1098/rstl.1802.0004 (cited on page 1).

[4] J. C. Maxwell, "A dynamical theory of the electromagnetic field", Philosophical Transactions of the Royal Society of London **155**, 459–512 (1997), https://doi.org/10.1098/rstl.1865.0008 (cited on page 1).

[5] A. Einstein, "Über einen die Erzeugung und Verwandlung des Lichtes betreffenden heuristischen Gesichtspunkt", Annalen der Physik **322**, 132–148 (1905), https://doi.org/10.1002/andp.19053220607 (cited on page 1).

[6] M. Born and E. Wolf, *Principles of Optics: Electromagnetic Theory of Propagation, Interference and Diffraction of Light*, 7th ed. (Cambridge University Press, Cambridge, 1999), https://www.cambridge.org/core/product/D12868B8AE26B83D6D3C2193E94FFC32 (cited on page 1).

[7] E. Yablonovitch, "Inhibited Spontaneous Emission in Solid-State Physics and Electronics", Physical Review Letters **58**, 2059–2062 (1987), https://link.aps.org/doi/10.1103/PhysRevLett.58.2059 (cited on page 1).

[8] D. Gao, W. Ding, M. Nieto-Vesperinas, X. Ding, M. Rahman, T. Zhang, C. Lim, and C. W. Qiu, "Optical manipulation from the microscale to the nanoscale: fundamentals, advances and prospects", Light Sci Appl **6**, e17039 (2017), https://www.ncbi.nlm.nih.gov/pubmed/30167291 (cited on page 1).

[9] S. Jahani and Z. Jacob, "All-dielectric metamaterials", Nature Nanotechnology **11**, 23–36 (2016), https://doi.org/10.1038/nnano.2015.304 (cited on page 1).

[10] N. Yu and F. Capasso, "Flat optics with designer metasurfaces", Nat Mater **13**, 139–150 (2014), https://www.ncbi.nlm.nih.gov/pubmed/24452357 (cited on pages 1, 66).

[11] A. V. Kildishev, A. Boltasseva, and V. M. Shalaev, "Planar Photonics with Metasurfaces", Science **339**, 1232009 (2013), https://doi.org/10.1126/science.1232009 (cited on page 1).

[12] A. I. Kuznetsov, A. E. Miroshnichenko, M. L. Brongersma, Y. S. Kivshar, and B. Luk'yanchuk, "Optically resonant dielectric nanostructures", Science **354**, 2472 (2016), https://www.ncbi.nlm.nih.gov/pubmed/27856851 (cited on pages 1, 66).

[13]K. Lodewijks, W. Van Roy, G. Borghs, L. Lagae, and P. Van Dorpe, "Boosting the figure-of-merit of LSPR-based refractive index sensing by phase-sensitive measurements", Nano Letters **12**, 10.1021/nl300044a (2012) (cited on pages 1, 44).

[14]T. Chung, H. Wang, and H. Cai, "Dielectric metasurfaces for next-generation optical biosensing: a comparison with plasmonic sensing", Nanotechnology **34**, 10.1088/1361-6528/ace117 (2023) (cited on pages 1, 44, 82, 83).

[15]T. Wang, S. Liu, J. Zhang, L. Xu, M. Yang, D. Ma, S. Jiang, Q. Jiao, and X. Tan, "Dual high-Q Fano resonances metasurfaces excited by asymmetric dielectric rods for refractive index sensing", Nanophotonics **13**, 463–475 (2024) (cited on page 1).

[16]W. Chen, M. Li, W. Zhang, and Y. Chen, "Dual-resonance sensing for environmental refractive index based on quasi-BIC states in all-dielectric metasurface", Nanophotonics **12**, 1147–1157 (2023) (cited on pages 1, 44, 45).

[17]L. Ghirardini, G. Marino, V. F. Gili, I. Favero, D. Rocco, L. Carletti, A. Locatelli, C. De Angelis, M. Finazzi, M. Celebrano, D. N. Neshev, and G. Leo, "Shaping the Nonlinear Emission Pattern of a Dielectric Nanoantenna by Integrated Holographic Gratings", Nano Letters **18**, 6750–6755 (2018), https://doi.org/10.1021/acs.nanolett.8b02432 (cited on page 1).

[18]B. Reineke, B. Sain, R. Zhao, L. Carletti, B. Liu, L. Huang, C. De Angelis, and T. Zentgraf, "Silicon Metasurfaces for Third Harmonic Geometric Phase Manipulation and Multiplexed Holography", Nano Letters **19**, 6585–6591 (2019), https://doi.org/10.1021/acs.nanolett.9b02844 (cited on page 1).

[19]C. U. Hail, L. Michaeli, and H. A. Atwater, "Third Harmonic Generation Enhancement and Wavefront Control Using a Local High-Q Metasurface", Nano Letters **24**, 2257–2263 (2024), https://doi.org/10.1021/acs.nanolett.3c04476 (cited on page 1).

[20]X. Liu, T. Galfsky, Z. Sun, F. Xia, E.-c. Lin, Y.-H. Lee, S. Kéna-Cohen, and V. M. Menon, "Strong light–matter coupling in two-dimensional atomic crystals", Nature Photonics **9**, 30–34 (2015), https://doi.org/10.1038/nphoton.2014.304 (cited on page 1).

[21]P. Xie, Y. Deng, Q. Ding, X. Zheng, Z. Zhou, Y. Kivshar, and W. Wang, "Strong Coupling of Resonant Metasurfaces with Epsilon-Near-Zero Guided Modes", Nano Lett **24**, 9027–9033 (2024), https://www.ncbi.nlm.nih.gov/pubmed/38984823 (cited on pages 1, 66).

[22]T. Low, A. Chaves, J. D. Caldwell, A. Kumar, N. X. Fang, P. Avouris, T. F. Heinz, F. Guinea, L. Martin-Moreno, and F. Koppens, "Polaritons in layered two-dimensional materials", Nature Materials **16**, 182–194 (2017), https://doi.org/10.1038/nmat4792 (cited on page 1).

[23]D. N. Basov, M. M. Fogler, and F. J. García de Abajo, "Polaritons in van der Waals materials", Science **354**, aag1992 (2016), https://doi.org/10.1126/science.aag1992 (cited on page 1).

[24]S. Kruk and Y. Kivshar, "Functional Meta-Optics and Nanophotonics Governed by Mie Resonances", ACS Photonics **4**, 2638–2649 (2017), https://doi.org/10.1021/acsphotonics.7b01038 (cited on page 2).

[25]C. W. Hsu, B. Zhen, A. D. Stone, J. D. Joannopoulos, and M. Soljačić, "Bound states in the continuum", Nature Reviews Materials **1**, 1–13 (2016) (cited on pages 2, 8, 44, 66).

[26]M. Kang, T. Liu, C. T. Chan, and M. Xiao, *Applications of bound states in the continuum in photonics*, 2023 (cited on pages 2, 44).

[27]S. Joseph, S. Pandey, S. Sarkar, and J. Joseph, "Bound states in the continuum in resonant nanostructures: an overview of engineered materials for tailored applications", Nanophotonics **10**, 4175–4207 (2021) (cited on pages 2, 76).

[28]S. I. Azzam, V. M. Shalaev, A. Boltasseva, and A. V. Kildishev, "Formation of Bound States in the Continuum in Hybrid Plasmonic-Photonic Systems", Phys Rev Lett **121**, 253901 (2018), https://www.ncbi.nlm.nih.gov/pubmed/30608828 (cited on pages 2, 76).

[29]A. Tittl, A. Leitis, M. Liu, F. Yesilkoy, D.-y. Choi, D. N. Neshev, Y. S. Kivshar, and H. Altug, "Imaging-based molecular barcoding with pixelated dielectric metasurfaces", Science **1109**, 1105–1109 (2018) (cited on pages 2, 44, 66, 82, 83).

[30]C. W. Hsu, B. Zhen, J. Lee, S. L. Chua, S. G. Johnson, J. D. Joannopoulos, and M. Soljacic, "Observation of trapped light within the radiation continuum", Nature **499**, 188–191 (2013), https://www.ncbi.nlm.nih.gov/pubmed/23846657 (cited on pages 2, 66).

[31]J. Wang, P. Li, X. Zhao, Z. Qian, X. Wang, F. Wang, X. Zhou, D. Han, C. Peng, L. Shi, and J. Zi, "Optical bound states in the continuum in periodic structures: mechanisms, effects, and applications", Photonics Insights **3**, R01 (2024), https://doi.org/10.3788/PI.2024.R01 (cited on pages 2, 66).

[32]S. Li, C. Zhou, T. Liu, and S. Xiao, "Symmetry-protected bound states in the continuum supported by all-dielectric metasurfaces", Physical Review A **100**, 063803 (2019) (cited on pages 2, 44).

[33]C. Zhou, M. Zhou, Z. Fu, H. He, Z. L. Deng, H. Xiang, X. Chen, W. Lu, G. Li, and D. Han, "Ultrahigh-Q Quasi-BICs via Precision-Controlled Asymmetry in Dielectric Metasurfaces", Nano Letters, 10.1021/acs.nanolett.5c00967 (2025) (cited on pages 2, 44).

[34]W. Wang, Y. K. Srivastava, T. C. Tan, Z. Wang, and R. Singh, "Brillouin zone folding driven bound states in the continuum", Nature Communications **14**, 2811 (2023), https://doi.org/10.1038/s41467-023-38367-y (cited on pages 2, 16, 17, 49, 67).

[35]J. von Neumann and E. P. Wigner, "Über merkwürdige diskrete Eigenwerte", in *The collected works of eugene paul wigner: part a: the scientific papers*, edited by A. S. Wightman (Springer Berlin Heidelberg, Berlin, Heidelberg, 1993), pp. 291–293, https://doi.org/10.1007/978-3-662-02781-3_19 (cited on page 9).

[36]S. V. Gaponenko, *Introduction to Nanophotonics* (Cambridge University Press, Cambridge, 2010), https://www.cambridge.org/core/product/9DE2D2114FDA21AA8B8DB953917B496C (cited on page 10).

[37]K. Koshelev, S. Lepeshov, M. Liu, A. Bogdanov, and Y. Kivshar, "Asymmetric Metasurfaces with High-Q Resonances Governed by Bound States in the Continuum", Phys Rev Lett **121**, 193903 (2018) (cited on pages 13, 18, 19, 44, 66, 70).

[38]F. Alpeggiani, N. Parappurath, E. Verhagen, and L. Kuipers, "Quasinormal-Mode Expansion of the Scattering Matrix", Physical Review X **7**, 21035 (2017), https://link.aps.org/doi/10.1103/PhysRevX.7.021035 (cited on page 13).

[39]T. Weiss, M. Mesch, M. Schäferling, H. Giessen, W. Langbein, and E. A. Muljarov, "From Dark to Bright: First-Order Perturbation Theory with Analytical Mode Normalization for Plasmonic Nanoantenna Arrays Applied to Refractive Index Sensing", Physical Review Letters **116**, 237401 (2016), https://link.aps.org/doi/10.1103/PhysRevLett.116.237401 (cited on page 18).

[40]A. B. Evlyukhin, T. Fischer, C. Reinhardt, and B. N. Chichkov, "Optical theorem and multipole scattering of light by arbitrarily shaped nanoparticles", Physical Review B **94**, 205434 (2016), https://link.aps.org/doi/10.1103/PhysRevB.94.205434 (cited on pages 18, 70, 71).

[41]S. Fan, W. Suh, and J. D. Joannopoulos, "Temporal coupled-mode theory for the Fano resonance in optical resonators", J Opt Soc Am A Opt Image Sci Vis **20**, 569–572 (2003), https://www.ncbi.nlm.nih.gov/pubmed/12630843 (cited on pages 21, 70).

[42]S. Fan, "12 - Photonic crystal theory: Temporal coupled-mode formalism", in *Optical fiber telecommunications v a (fifth edition)*, edited by I. P. Kaminow, T. Li, and A. E. Willner (Academic Press, Burlington, 2008), pp. 431–454, https://www.sciencedirect.com/science/article/pii/B9780123741714000125 (cited on page 21).

[43]W. Suh, Z. Wang, and S. Fan, "Temporal coupled-mode theory and the presence of non-orthogonal modes in lossless multimode cavities", IEEE Journal of Quantum Electronics **40**, 1511–1518 (2004) (cited on page 21).

[44]T. Christopoulos, O. Tsilipakos, G. Sinatkas, and E. E. Kriezis, "On the calculation of the quality factor in contemporary photonic resonant structures", Optics Express **27**, 14505–14522 (2019), https://opg.optica.org/oe/abstract.cfm?URI=oe-27-10-14505 (cited on page 25).

[45]D. Natelson, *Nanostructures and Nanotechnology* (Cambridge University Press, Cambridge, 2015), https://www.cambridge.org/core/product/20961BB4BAA3F2B57373D9D614243440 (cited on pages 31, 32, 37).

[46]A. Aigner, "Spatial and temporal symmetry-breaking in bound states in the continuum metasurfaces.", PhD thesis (Apr. 2025) (cited on pages 33, 35).

[47]T. N. Gölz, *Advanced near-field microscopic studies of nanophotonic and complex biological samples*, Feb. 2025, http://nbn-resolving.de/urn:nbn:de:bvb:19-348585 (cited on page 42).

[48]X. Yang, A. Antonov, H. Hu, and A. Tittl, "Permittivity-asymmetric qBIC metasurfaces for refractive index sensing", Nanophotonics, doi:10.1515/nanoph-2025-0415, https://doi.org/10.1515/nanoph-2025-0415 (cited on pages 43, 83).

[49]M. S. Hwang, H. C. Lee, K. H. Kim, K. Y. Jeong, S. H. Kwon, K. Koshelev, Y. Kivshar, and H. G. Park, "Ultralow-threshold laser using super-bound states in the continuum", Nature Communications **12**, 10.1038/s41467-021-24502-0 (2021) (cited on page 44).

[50]H. Hu, A. K. Pal, A. Berestennikov, T. Weber, A. Stefancu, E. Cortés, S. A. Maier, and A. Tittl, "Surface-Enhanced Raman Scattering in BIC-Driven Semiconductor Metasurfaces", Advanced Optical Materials, 10.1002/adom.202302812 (2024) (cited on page 44).

[51]Z. Sadrieva, K. Frizyuk, M. Petrov, Y. Kivshar, and A. Bogdanov, "Multipolar origin of bound states in the continuum", Physical Review B **100**, 1–12 (2019) (cited on page 44).

[52]Z. Liu, Y. Xu, Y. Lin, J. Xiang, T. Feng, Q. Cao, J. Li, S. Lan, and J. Liu, "High- Q Quasibound States in the Continuum for Nonlinear Metasurfaces", Physical Review Letters **123**, 1–6 (2019) (cited on page 44).

[53]V. R. Tuz, V. V. Khardikov, A. S. Kupriianov, K. L. Domina, S. Xu, H. Wang, and H.-B. Sun, "High-quality trapped modes in all-dielectric metamaterials", Optics Express **26**, 10.1364/oe.26.002905 (2018) (cited on page 44).

[54]A. Forouzmand and H. Mosallaei, "All-Dielectric C-Shaped Nanoantennas for Light Manipulation: Tailoring Both Magnetic and Electric Resonances to the Desire", Advanced Optical Materials **5**, 10.1002/adom.201700147 (2017) (cited on page 44).

[55]R. Singh, I. A. I. Al-Naib, Y. Yang, D. Roy Chowdhury, W. Cao, C. Rockstuhl, T. Ozaki, R. Morandotti, and W. Zhang, "Observing metamaterial induced transparency in individual Fano resonators with broken symmetry", Applied Physics Letters **99**, 201107 (2011), https://doi.org/10.1063/1.3659494 (cited on page 44).

[56]S. Campione, S. Liu, L. I. Basilio, L. K. Warne, W. L. Langston, T. S. Luk, J. R. Wendt, J. L. Reno, G. A. Keeler, I. Brener, and M. B. Sinclair, "Broken Symmetry Dielectric Resonators for High Quality Factor Fano Metasurfaces", ACS Photonics **3**, 2362–2367 (2016), https://doi.org/10.1021/acsphotonics.6b00556 (cited on page 44).

[57]F. Zhang, X. Huang, Q. Zhao, L. Chen, Y. Wang, Q. Li, X. He, C. Li, and K. Chen, "Fano resonance of an asymmetric dielectric wire pair", Applied Physics Letters **105**, 172901 (2014), https://doi.org/10.1063/1.4900757 (cited on page 44).

[58]S. A. Khan, N. Z. Khan, Y. Xie, M. T. Abbas, M. Rauf, I. Mehmood, M. Runowski, S. Agathopoulos, and J. Zhu, *Optical Sensing by Metamaterials and Metasurfaces: From Physics to Biomolecule Detection*, 2022 (cited on page 44).

[59]H. Li, J. T. Kim, J. S. Kim, D. Y. Choi, and S. S. Lee, "Metasurface-Incorporated Optofluidic Refractive Index Sensing for Identification of Liquid Chemicals through Vision Intelligence", ACS Photonics **10**, 10.1021/acsphotonics.3c00057 (2023) (cited on page 44).

[60]L. La Spada, "Metasurfaces for advanced sensing and diagnostics", Sensors (Switzerland) **19**, 10.3390/s19020355 (2019) (cited on page 44).

[61]D. N. Maksimov, V. S. Gerasimov, A. A. Bogdanov, and S. P. Polyutov, "Enhanced sensitivity of an all-dielectric refractive index sensor with an optical bound state in the continuum", Physical Review A **105**, 10.1103/PhysRevA.105.033518 (2022) (cited on page 44).

[62]H. H. Hsiao, Y. C. Hsu, A. Y. Liu, J. C. Hsieh, and Y. H. Lin, "Ultrasensitive Refractive Index Sensing Based on the Quasi-Bound States in the Continuum of All-Dielectric Metasurfaces", Advanced Optical Materials **10**, 10.1002/adom.202200812 (2022) (cited on page 44).

[63]S. Romano, M. Mangini, E. Penzo, S. Cabrini, A. C. De Luca, I. Rendina, V. Mocella, and G. Zito, "Ultrasensitive surface refractive index imaging based on quasi-bound states in the continuum", ACS Nano **14**, 10.1021/acsnano.0c06050 (2020) (cited on page 44).

[64]K. Watanabe, T. Nagao, and M. Iwanaga, "Low-Contrast BIC Metasurfaces with Quality Factors Exceeding 100,000", Nano Letters, 10.1021/acs.nanolett.4c05880 (2025) (cited on pages 44, 45).

[65]X. Wang and J. L. Wang, "Refractive index sensing characteristics of electromagnetic metamaterial absorber in terahertz band", Wuli Xuebao/Acta Physica Sinica **70**, 10.7498/aps.70.20201054 (2021) (cited on page 44).

[66]Y. Xu, P. Bai, X. Zhou, Y. Akimov, C. E. Png, L. K. Ang, W. Knoll, and L. Wu, *Optical Refractive Index Sensors with Plasmonic and Photonic Structures: Promising and Inconvenient Truth*, May 2019 (cited on page 44).

[67]A. E. Cetin, A. F. Coskun, B. C. Galarreta, M. Huang, D. Herman, A. Ozcan, and H. Altug, "Handheld high-throughput plasmonic biosensor using computational on-chip imaging", Light: Science and Applications **3**, 10.1038/lsa.2014.3 (2014) (cited on page 44).

[68]G. A. Lopez, M. C. Estevez, M. Soler, and L. M. Lechuga, *Recent advances in nanoplasmonic biosensors: Applications and lab-on-a-chip integration*, Jan. 2017 (cited on page 44).

[69]A. J. Ollanik, I. O. Oguntoye, G. Z. Hartfield, and M. D. Escarra, "Highly Sensitive, Affordable, and Adaptable Refractive Index Sensing with Silicon-Based Dielectric Metasurfaces", Advanced Materials Technologies **4**, 10.1002/admt.201800567 (2019) (cited on pages 44, 56).

[70]A. Kapoor and E. K. Sharma, "Long period grating refractive-index sensor: Optimal design for single wavelength interrogation", Applied Optics **48**, 10.1364/AO.48.000G88 (2009) (cited on page 44).

[71]E. Zanganeh, Z. Sadrieva, P. Kapitanova, and A. Bogdanov, "High- Q Mie resonators for refractive-index sensing", Physical Review Applied **21**, 10.1103/PhysRevApplied.21.024028 (2024) (cited on page 44).

[72]J. Zhou, A. Panday, Y. Xu, X. Chen, L. Chen, C. Ji, and L. J. Guo, "Visualizing Mie Resonances in Low-Index Dielectric Nanoparticles", Physical Review Letters **120**, 10.1103/PhysRevLett.120.253902 (2018) (cited on page 44).

[73]B. Gallinet and O. J. Martin, "Refractive index sensing with subradiant modes: A framework to reduce losses in plasmonic nanostructures", ACS Nano **7**, 10.1021/nn4021967 (2013) (cited on page 44).

[74]Y. Shen, J. Zhou, T. Liu, Y. Tao, R. Jiang, M. Liu, G. Xiao, J. Zhu, Z. K. Zhou, X. Wang, C. Jin, and J. Wang, "Plasmonic gold mushroom arrays with refractive index sensing figures of merit approaching the theoretical limit", Nature Communications **4**, 10.1038/ncomms3381 (2013) (cited on page 44).

[75]H. Hu, W. Lu, A. Antonov, R. Berté, S. A. Maier, and A. Tittl, "Environmental permittivity-asymmetric BIC metasurfaces with electrical reconfigurability", Nature Communications **15**, 10.1038/s41467-024-51340-7 (2024) (cited on pages 45, 66).

[76]A. Aigner, T. Possmayer, T. Weber, A. A. Antonov, L. de S. Menezes, S. A. Maier, and A. Tittl, "Optical control of resonances in temporally symmetry-broken metasurfaces", Nature, 10.1038/s41586-025-09363-7 (2025), https://doi.org/10.1038/s41586-025-09363-7 (cited on pages 46, 83).

[77]L. E. Ocola and A. Stein, "Effect of cold development on improvement in electron-beam nanopatterning resolution and line roughness", Journal of Vacuum Science & Technology B: Microelectronics and Nanometer Structures Processing, Measurement, and Phenomena **24**, 3061–3065 (2006), https://doi.org/10.1116/1.2366698 (cited on page 48).

[78]F. Rahman, D. Carbaugh, J. Wright, P. Rajan, S. Pandya, and S. Kaya, "A review of polymethyl methacrylate (PMMA) as a versatile lithographic resist – With emphasis on UV exposure", Microelectronic Engineering **224**, 111238 (2020) (cited on page 48).

[79]C. Oehr, "Plasma surface modification of polymers for biomedical use", Nuclear Instruments and Methods in Physics Research Section B: Beam Interactions with Materials and Atoms **208**, 40–47 (2003), https://www.sciencedirect.com/science/article/pii/S0168583X03006505 (cited on page 48).

[80]S. Anbumani, A. M. da Silva, A. Alaferdov, M. V. Puydinger dos Santos, I. G. B. Carvalho, M. de Souza e Silva, S. Moshkalev, H. F. Carvalho, A. A. de Souza, and M. A. Cotta, "Physiochemically Distinct Surface Properties of SU-8 Polymer Modulate Bacterial Cell-Surface Holdfast and Colonization", ACS Applied Bio Materials **5**, 4903–4912 (2022), https://doi.org/10.1021/acsabm.2c00632 (cited on page 48).

[81]K. Sun, H. Wei, W. Chen, Y. Chen, Y. Cai, C.-W. Qiu, and Z. Han, "Infinite-Q guided modes radiate in the continuum", Physical Review B **107**, 115415 (2023), https://link.aps.org/doi/10.1103/PhysRevB.107.115415 (cited on page 49).

[82]K. V. Sreekanth, Y. Alapan, M. ElKabbash, E. Ilker, M. Hinczewski, U. A. Gurkan, A. De Luca, and G. Strangi, "Extreme sensitivity biosensing platform based on hyperbolic metamaterials", Nature Materials **15**, 621–627 (2016), https://doi.org/10.1038/nmat4609 (cited on page 56).

[83]Y. Li, H. Fei, X. Liu, and H. Lin, "Design of Refractive Index Sensors Based on Valley Photonic Crystal Mach–Zehnder Interferometer", Sensors **25**, 10.3390/s25113289 (2025), https://www.mdpi.com/1424-8220/25/11/3289 (cited on page 56).

[84]H. Li, Z. Shi, H. Zhang, S. Qiu, and Z.-K. Zhou, "Hybrid Metasurface Based on Si3N4 Nanopillar for Optical Sensing with Dual Channels", ACS Applied Nano Materials **8**, 2965–2973 (2025), https://doi.org/10.1021/acsanm.4c06648 (cited on page 56).

[85]F. Usman, J. O. Dennis, E. M. Mkawi, Y. Al-Hadeethi, F. Meriaudeau, Y. W. Fen, A. R. Sadrolhosseini, T. L. Ferrell, A. Alsadig, and A. Sulieman, "Acetone Vapor-Sensing Properties of Chitosan-Polyethylene Glycol Using Surface Plasmon Resonance Technique", Polymers **12**, 10.3390/polym12112586 (2020), https://www.mdpi.com/2073-4360/12/11/2586 (cited on page 56).

[86]L. Suo, H. Zhou, Y.-P. Peng, F. Yang, H.-C. Chui, and N.-K. Chen, "High Sensitivity Fiber Refractive Index Sensors Based on Asymmetric Supermodes Interference in Tapered Four Core Fiber", Photonics **9**, 10.3390/photonics9010045 (2022), https://www.mdpi.com/2304-6732/9/1/45 (cited on page 56).

[87]Z. Li, L. Hou, L. Ran, J. Kang, and J. Yang, "Ultra-Sensitive Fiber Refractive Index Sensor with Intensity Modulation and Self-Temperature Compensation", Sensors **19**, 10.3390/s19183820 (2019), https://www.mdpi.com/1424-8220/19/18/3820 (cited on page 56).

[88]X. Yang, A. Antonov, A. Aigner, T. Weber, Y. Lee, T. Jiang, H. Hu, and A. Tittl, "Polarization-independent metasurfaces based on bound states in the continuum with high Q-factor and resonance modulation", Optics Express **33**, 15682–15689 (2025), https://opg.optica.org/oe/abstract.cfm?URI=oe-33-7-15682 (cited on pages 65, 83, 89).

[89]A. I. Kuznetsov, M. L. Brongersma, J. Yao, M. K. Chen, U. Levy, D. P. Tsai, N. I. Zheludev, A. Faraon, A. Arbabi, N. Yu, D. Chanda, K. B. Crozier, A. V. Kildishev, H. Wang, J. K. W. Yang, J. G. Valentine, P. Genevet, J. A. Fan, O. D. Miller, A. Majumdar, J. E. Froch, D. Brady, F. Heide, A. Veeraraghavan, N. Engheta, A. Alu, A. Polman, H. A. Atwater, P. Thureja, R. Paniagua-Dominguez, S. T. Ha, A. I. Barreda, J. A. Schuller, I. Staude, G. Grinblat, Y. Kivshar, S. Peana, S. F. Yelin, A. Senichev, V. M. Shalaev, S. Saha, A. Boltasseva, J. Rho, D. K. Oh, J. Kim, J. Park, R. Devlin, and R. A. Pala, "Roadmap for Optical Metasurfaces", ACS Photonics **11**, 816–865 (2024), https://www.ncbi.nlm.nih.gov/pubmed/38550347 (cited on page 66).

[90]P. Genevet, F. Capasso, F. Aieta, M. Khorasaninejad, and R. Devlin, "Recent advances in planar optics: from plasmonic to dielectric metasurfaces", Optica **4**, 139–152 (2017), https://opg.optica.org/optica/abstract.cfm?URI=optica-4-1-139 (cited on page 66).

[91]Z. Bomzon, G. Biener, V. Kleiner, and E. Hasman, "Space-variant Pancharatnam-Berry phase optical elements with computer-generated subwavelength gratings", Opt Lett **27**, 1141–1143 (2002), https://www.ncbi.nlm.nih.gov/pubmed/18026387 (cited on page 66).

[92]E. Lassalle, T. W. W. Mass, D. Eschimese, A. V. Baranikov, E. Khaidarov, S. Li, R. Paniagua-Dominguez, and A. I. Kuznetsov, "Imaging Properties of Large Field-of-View Quadratic Metalenses and Their Applications to Fingerprint Detection", ACS Photonics **8**, 1457–1468 (2021), https://doi.org/10.1021/acsphotonics.1c00237 (cited on page 66).

[93]R. Paniagua-Dominguez, Y. F. Yu, E. Khaidarov, S. Choi, V. Leong, R. M. Bakker, X. Liang, Y. H. Fu, V. Valuckas, L. A. Krivitsky, and A. I. Kuznetsov, "A Metalens with a Near-Unity Numerical Aperture", Nano Lett **18**, 2124–2132 (2018), https://www.ncbi.nlm.nih.gov/pubmed/29485885 (cited on page 66).

[94]Y. Luo, C. H. Chu, S. Vyas, H. Y. Kuo, Y. H. Chia, M. K. Chen, X. Shi, T. Tanaka, H. Misawa, Y. Y. Huang, and D. P. Tsai, "Varifocal Metalens for Optical Sectioning Fluorescence Microscopy", Nano Lett **21**, 5133–5142 (2021), https://www.ncbi.nlm.nih.gov/pubmed/34097419 (cited on page 66).

[95]A. Aigner, F. Ligmajer, K. Rovenska, J. Holobradek, B. Idesova, S. A. Maier, A. Tittl, and S. M. L. de, "Engineering of Active and Passive Loss in High-Quality-Factor Vanadium Dioxide-Based BIC Metasurfaces", Nano Lett **24**, 10742–10749 (2024), https://www.ncbi.nlm.nih.gov/pubmed/39191398 (cited on page 66).

[96]A. Aigner, T. Weber, A. Wester, S. A. Maier, and A. Tittl, "Continuous spectral and coupling-strength encoding with dual-gradient metasurfaces", Nat Nanotechnol, 10.1038/s41565-024-01767-2 (2024), https://www.ncbi.nlm.nih.gov/pubmed/39187580 (cited on pages 66, 84, 98).

[97]L. Kuhner, L. Sortino, R. Berte, J. Wang, H. Ren, S. A. Maier, Y. Kivshar, and A. Tittl, "Radial bound states in the continuum for polarization-invariant nanophotonics", Nat Commun **13**, 4992 (2022), https://www.ncbi.nlm.nih.gov/pubmed/36008419 (cited on page 66).

[98]P. Vaity, H. Gupta, A. Kala, S. Dutta Gupta, Y. S. Kivshar, V. R. Tuz, and V. G. Achanta, "Polarization-Independent Quasibound States in the Continuum", Advanced Photonics Research **3**, 2100144 (2021), https://onlinelibrary.wiley.com/doi/abs/10.1002/adpr.202100144 (cited on pages 66, 67, 84).

[99]S. Xiao, M. Qin, J. Duan, and T. Liu, "Robust enhancement of high-harmonic generation from all-dielectric metasurfaces enabled by polarization-insensitive bound states in the continuum", Opt Express **30**, 32590–32599 (2022), https://www.ncbi.nlm.nih.gov/pubmed/36242316 (cited on pages 66, 70, 84).

[100]H. Zhong, T. He, Y. Wang, T. Qi, Y. Meng, D. Li, P. Yan, and Q. Xiao, "Efficient polarization-insensitive quasi-BIC modulation by VO(2) thin films", Opt Express **32**, 5862–5873 (2024), https://www.ncbi.nlm.nih.gov/pubmed/38439302 (cited on pages 66, 84).

[101]Y. Cai, Y. Huang, K. Zhu, and H. Wu, "Symmetric metasurface with dual band polarization-independent high-Q resonances governed by symmetry-protected BIC", Opt Lett **46**, 4049–4052 (2021), https://www.ncbi.nlm.nih.gov/pubmed/34388808 (cited on page 66).

[102]X. Wang, S. Li, and C. Zhou, "Polarization-independent toroidal dipole resonances driven by symmetry-protected BIC in ultraviolet region", Opt Express **28**, 11983–11989 (2020), https://www.ncbi.nlm.nih.gov/pubmed/32403699 (cited on pages 66, 84).

[103]J. Y. Gao, J. Liu, H. M. Yang, H. S. Liu, G. Zeng, and B. Huang, "Anisotropic medium sensing controlled by bound states in the continuum in polarization-independent metasurfaces", Opt Express **31**, 44703–44719 (2023), https://www.ncbi.nlm.nih.gov/pubmed/38178534 (cited on pages 66, 84).

[104]R. Masoudian Saadabad, L. Huang, and A. E. Miroshnichenko, "Polarization-independent perfect absorber enabled by quasibound states in the continuum", Physical Review B **104**, 235405 (2021), https://link.aps.org/doi/10.1103/PhysRevB.104.235405 (cited on pages 66, 84).

[105]S. Chen, Y. Zeng, Z. Li, Y. Mao, X. Dai, and Y. Xiang, "Passive nonreciprocal transmission and optical bistability based on polarization-independent bound states in the continuum", Nanophotonics **12**, 3613–3621 (2023), https://doi.org/10.1515/nanoph-2023-0319 (cited on page 66).

[106]L. Wang, Z. Zhao, M. Du, H. Qin, R. T. Ako, and S. Sriram, "Polarization insensitive symmetry protected quasi-bound states in the continuum at terahertz band", Journal of Applied Physics **130**, 10.1063/5.0075056 (2021), https://doi.org/10.1063/5.0075056 (cited on page 67).

[107]J. Ding, L. Huang, Y. Luo, T. Wang, J. Hu, R. Li, and S. Xiao, "Multi-Band Polarization-Independent Quasi-Bound States in the Continuum Based on Tetramer-Based Metasurfaces and Their Potential Application in Terahertz Microfluidic Biosensing", Advanced Optical Materials **11**, 2300685 (2023), https://onlinelibrary.wiley.com/doi/abs/10.1002/adom.202300685 (cited on page 67).

[108]A. Aigner, A. Tittl, J. Wang, T. Weber, Y. Kivshar, S. A. Maier, and H. Ren, "Plasmonic bound states in the continuum to tailor light-matter coupling", Sci Adv **8**, 4816 (2022), https://www.ncbi.nlm.nih.gov/pubmed/36490330 (cited on pages 70, 90).

[109]E. A. Gurvitz, K. S. Ladutenko, P. A. Dergachev, A. B. Evlyukhin, A. E. Miroshnichenko, and A. S. Shalin, "The High-Order Toroidal Moments and Anapole States in All-Dielectric Photonics", Laser & Photonics Reviews **13**, 1800266 (2019), https://onlinelibrary.wiley.com/doi/abs/10.1002/lpor.201800266 (cited on page 70).

[110]P. D. Terekhov, V. E. Babicheva, K. V. Baryshnikova, A. S. Shalin, A. Karabchevsky, and A. B. Evlyukhin, "Multipole analysis of dielectric metasurfaces composed of nonspherical nanoparticles and lattice invisibility effect", Physical Review B **99**, 45424 (2019), https://link.aps.org/doi/10.1103/PhysRevB.99.045424%20https://journals.aps.org/prb/abstract/10.1103/PhysRevB.99.045424 (cited on pages 70, 71).

[111]P. D. Terekhov, K. V. Baryshnikova, Y. A. Artemyev, A. Karabchevsky, A. S. Shalin, and A. B. Evlyukhin, "Multipolar response of nonspherical silicon nanoparticles in the visible and near-infrared spectral ranges", Physical Review B **96**, 35443 (2017), https://link.aps.org/doi/10.1103/PhysRevB.96.035443 (cited on pages 70, 71).

[112]C. Menzel, C. Rockstuhl, and F. Lederer, "Advanced Jones calculus for the classification of periodic metamaterials", Physical Review A **82**, 53811 (2010), https://link.aps.org/doi/10.1103/PhysRevA.82.053811 (cited on page 72).

[113]F. Neubrech, C. Huck, K. Weber, A. Pucci, and H. Giessen, "Surface-Enhanced Infrared Spectroscopy Using Resonant Nanoantennas", Chemical Reviews **117**, 5110–5145 (2017), https://doi.org/10.1021/acs.chemrev.6b00743 (cited on page 82).

[114]A. Tittl, A. John-Herpin, A. Leitis, E. R. Arvelo, and H. Altug, "Metasurface-Based Molecular Biosensing Aided by Artificial Intelligence", Angewandte Chemie International Edition **58**, 14810–14822 (2019), https://doi.org/10.1002/anie.201901443 (cited on page 82).

[115]D. Dregely, F. Neubrech, H. Duan, R. Vogelgesang, and H. Giessen, "Vibrational near-field mapping of planar and buried three-dimensional plasmonic nanostructures", Nature Communications **4**, 2237 (2013), https://doi.org/10.1038/ncomms3237 (cited on page 82).

[116]D. Rodrigo, A. Tittl, N. Ait-Bouziad, A. John-Herpin, O. Limaj, C. Kelly, D. Yoo, N. J. Wittenberg, S.-H. Oh, H. A. Lashuel, and H. Altug, "Resolving molecule-specific information in dynamic lipid membrane processes with multi-resonant infrared metasurfaces", Nature Communications **9**, 2160 (2018), https://doi.org/10.1038/s41467-018-04594-x (cited on page 82).

[117]J. Wang, T. Weber, A. Aigner, S. A. Maier, and A. Tittl, "Mirror-Coupled Plasmonic Bound States in the Continuum for Tunable Perfect Absorption", Laser & Photonics Reviews **17**, 2300294 (2023), https://doi.org/10.1002/lpor.202300294 (cited on pages 82, 84, 87, 91).

[118]M. Autore, P. Li, I. Dolado, F. J. Alfaro-Mozaz, R. Esteban, A. Atxabal, F. Casanova, L. E. Hueso, P. Alonso-González, J. Aizpurua, A. Y. Nikitin, S. Vélez, and R. Hillenbrand, "Boron nitride nanoresonators for phonon-enhanced molecular vibrational spectroscopy at the strong coupling limit", Light: Science & Applications **7**, 17172 (2018), https://doi.org/10.1038/lsa.2017.172 (cited on page 82).

[119]D. Rodrigo, O. Limaj, D. Janner, D. Etezadi, F. J. García de Abajo, V. Pruneri, and H. Altug, "Mid-infrared plasmonic biosensing with graphene", Science **349**, 165–168 (2015), https://doi.org/10.1126/science.aab2051 (cited on page 82).

[120]M. Barkey, R. Büchner, A. Wester, S. D. Pritzl, M. Makarenko, Q. Wang, T. Weber, D. Trauner, S. A. Maier, A. Fratalocchi, T. Lohmüller, and A. Tittl, "Pixelated High-Q Metasurfaces for in Situ Biospectroscopy and Artificial Intelligence-Enabled Classification of Lipid Membrane Photoswitching Dynamics", ACS Nano **18**, 11644–11654 (2024), https://doi.org/10.1021/acsnano.3c09798 (cited on page 82).

[121]T. Jiang, A. Bhattacharya, M. Barkey, A. Aigner, L. Rohrer, T. Weber, J. Wang, S. A. Maier, and A. Tittl, "A Comparative Analysis of Plasmonic and Dielectric Metasurface Sensing Platforms Powered by Bound States in the Continuum", Advanced Functional Materials **n/a**, e16021 (2025), https://doi.org/10.1002/adfm.202516021 (cited on pages 82, 85).

[122]G. Giubertoni, M. Bonn, and S. Woutersen, "D2O as an Imperfect Replacement for H2O: Problem or Opportunity for Protein Research?", The Journal of Physical Chemistry B **127**, 8086–8094 (2023), https://doi.org/10.1021/acs.jpcb.3c04385 (cited on page 82).

[123]O. Limaj, D. Etezadi, N. J. Wittenberg, D. Rodrigo, D. Yoo, S.-H. Oh, and H. Altug, "Infrared Plasmonic Biosensor for Real-Time and Label-Free Monitoring of Lipid Membranes", Nano Letters **16**, 1502–1508 (2016), https://doi.org/10.1021/acs.nanolett.5b05316 (cited on page 82).

[124]A. John-Herpin, A. Tittl, and H. Altug, "Quantifying the Limits of Detection of Surface-Enhanced Infrared Spectroscopy with Grating Order-Coupled Nanogap Antennas", ACS Photonics **5**, 4117–4124 (2018), https://doi.org/10.1021/acsphotonics.8b00847 (cited on page 82).

[125]S. H. Huang, J. Li, Z. Fan, R. Delgado, and G. Shvets, "Monitoring the effects of chemical stimuli on live cells with metasurface-enhanced infrared reflection spectroscopy", Lab on a Chip **21**, 3991–4004 (2021), http://dx.doi.org/10.1039/D1LC00580D (cited on page 82).

[126]L. Dong, X. Yang, C. Zhang, B. Cerjan, L. Zhou, M. L. Tseng, Y. Zhang, A. Alabastri, P. Nordlander, and N. J. Halas, "Nanogapped Au Antennas for Ultrasensitive Surface-Enhanced Infrared Absorption Spectroscopy", Nano Letters **17**, 5768–5774 (2017), https://doi.org/10.1021/acs.nanolett.7b02736 (cited on page 82).

[127]M. Caldarola, P. Albella, E. Cortés, M. Rahmani, T. Roschuk, G. Grinblat, R. F. Oulton, A. V. Bragas, and S. A. Maier, "Non-plasmonic nanoantennas for surface enhanced spectroscopies with ultra-low heat conversion", Nature Communications **6**, 7915 (2015), https://doi.org/10.1038/ncomms8915 (cited on page 83).

[128]G. Qiu, Z. Gai, Y. Tao, J. Schmitt, G. A. Kullak-Ublick, and J. Wang, "Dual-Functional Plasmonic Photothermal Biosensors for Highly Accurate Severe Acute Respiratory Syndrome Coronavirus 2 Detection", ACS Nano **14**, 5268–5277 (2020), https://doi.org/10.1021/acsnano.0c02439 (cited on page 83).

[129]N. A. Toropov, M. C. Houghton, D. Yu, and F. Vollmer, "Thermo-Optoplasmonic Single-Molecule Sensing on Optical Microcavities", ACS Nano **18**, 17534–17546 (2024), https://doi.org/10.1021/acsnano.4c00877 (cited on page 83).

[130]M. C. Houghton, S. V. Kashanian, T. L. Derrien, K. Masuda, and F. Vollmer, "Whispering-Gallery Mode Optoplasmonic Microcavities: From Advanced Single-Molecule Sensors and Microlasers to Applications in Synthetic Biology", ACS Photonics **11**, 892–903 (2024), https://doi.org/10.1021/acsphotonics.3c01570 (cited on page 83).

[131]D. Etezadi, J. B. I. V. Warner, H. A. Lashuel, and H. Altug, "Real-Time In Situ Secondary Structure Analysis of Protein Monolayer with Mid-Infrared Plasmonic Nanoantennas", ACS Sensors **3**, 1109–1117 (2018), https://doi.org/10.1021/acssensors.8b00115 (cited on page 83).

[132]F. Neubrech, A. Pucci, T. W. Cornelius, S. Karim, A. García-Etxarri, and J. Aizpurua, "Resonant Plasmonic and Vibrational Coupling in a Tailored Nanoantenna for Infrared Detection", Physical Review Letters **101**, 157403 (2008), https://link.aps.org/doi/10.1103/PhysRevLett.101.157403 (cited on page 84).

[133]C. Wu, A. B. Khanikaev, R. Adato, N. Arju, A. A. Yanik, H. Altug, and G. Shvets, "Fano-resonant asymmetric metamaterials for ultrasensitive spectroscopy and identification of molecular monolayers", Nature Materials **11**, 69–75 (2012), https://doi.org/10.1038/nmat3161 (cited on page 84).

[134]E. Baù, A. Aigner, J. Biechteler, C. Heimig, T. Weber, T. Gölz, S. A. Maier, and A. Tittl, "Spatially Encoded Polaritonic Ultra-Strong Coupling in Gradient Metasurfaces with Epsilon-Near-Zero Modes", Advanced Materials **n/a**, e10402 (2025), https://doi.org/10.1002/adma.202510402 (cited on page 84).

[135]T. Gölz, E. Baù, A. Aigner, A. Mancini, M. Barkey, F. Keilmann, S. A. Maier, and A. Tittl, "Revealing Mode Formation in Quasi-Bound States in the Continuum Metasurfaces via Near-Field Optical Microscopy", Advanced Materials **36**, 2405978 (2024), https://doi.org/10.1002/adma.202405978 (cited on page 84).

[136]L. Paggi, A. Fabas, H. El Ouazzani, J.-P. Hugonin, N. Fayard, N. Bardou, C. Dupuis, J.-J. Greffet, and P. Bouchon, "Over-coupled resonator for broadband surface enhanced infrared absorption (SEIRA)", Nature Communications **14**, 4814 (2023), https://doi.org/10.1038/s41467-023-40511-7 (cited on page 90).

[137]R. Adato, A. Artar, S. Erramilli, and H. Altug, "Engineered Absorption Enhancement and Induced Transparency in Coupled Molecular and Plasmonic Resonator Systems", Nano Letters **13**, 2584–2591 (2013), https://doi.org/10.1021/nl400689q (cited on page 90).

[138]K. Chen, R. Adato, and H. Altug, "Dual-Band Perfect Absorber for Multispectral Plasmon-Enhanced Infrared Spectroscopy", ACS Nano **6**, 7998–8006 (2012), https://doi.org/10.1021/nn3026468 (cited on page 91).

Acknowledgements

The past four years have unfolded in ways far beyond what I could have anticipated when I first decided to cross continents and come to Germany. Looking back, I wonder whether I would still have had the courage to come if I had known in advance what I would need to learn, adapt and grow. And yet, I feel deeply grateful for the experiences along the way that have brought me to where I am and shaped who I am today. In many ways, a PhD thesis is like the visible tip of an iceberg, modest on the surface, but supported by a much larger foundation beneath: living life abroad, self-understanding, growth in both mind and body, and a sense of peace with the path I went through.

I would like to sincerely thank **Prof. Andreas Tittl** for believing in me and offering me the opportunity to pursue my PhD when I had two and a half years left on my contract. He holds high academic standards while remaining kind and respectful, and I appreciate the trust and support he gives to international students. Although our group is large and there are many strong projects, I always felt that he understood my time constraints and encouraged me to move forward in a steady and realistic way. In particular, he allowed me to start from projects and publications that matched my ability, which greatly eased my pressure. With his guidance, I could clearly feel my work becoming more solid step by step, and the quality of my output improving over time. Whenever I encountered difficulties, I was always willing to communicate with him, and I often left our discussions feeling lighter and clearer. I feel truly fortunate to have had a supervisor I respect, whose guidance and support helped me move forward through these years.

My sincere thanks also go to **Prof. Leonardo Menezes** for his support. Thank you for reminding me of my credit requirements, for respecting my choices, and for supporting me in gaining important opportunities. Without your help, I would not have had the chance to complete my studies at the Nanoinstitute.

I would like to thank **Prof. Stefan Maier** for bringing me to the LMU Nanoinstitute, giving me the opportunity to study and work abroad, and for his generous support in helping me settle in during the early stage of my PhD.

I would also like to thank my co-authors **Dr. Alexander Antonov, Dr. Andreas Aigner, Thomas Weber, Dr. Haiyang Hu, etc.**. Thank you for the collaboration on several projects and for the contributions each of you made toward our shared goals. These experiences strengthened my ability to collaborate and communicate effectively and also helped me develop a clearer sense of professional boundaries.

I am also grateful for the moments shared beyond work with colleagues at the institute hiking with **Dr. Thorsten Gölz** and **Dr. Angana Bhattacharya**, conversations with **Jennifer, Enrico Baù**, **Michael Hirler, etc.**, and playing billiards organized by **Christoph Gruber**. These shared activities allowed me to experience a sense of friendship beyond work, and they have stayed with me as warm memories alongside daily research life.

My thanks also go to **Reinhold Rath, Denise Wedemeyer, Jonas Biechteler, Connor Heimig, Martin Barkey, Lina Rohrer, Ruosong Wang, Yuan Si, Kevin Alex, Vitus Magin, Dr. Manobina Karmakar, Dr. Yohan Lee, Dr. Wenzheng Lu, Levin Seidt, Dr. Luca Berger, Xueqing Miao, Thomas Possmayer, Jiaqi Chen, Dr. Abhinav Sharma, Franz Gröbmeyer, Chenghao Fan, Edoardo Mariani, and Dr. Simone Ezendam**. I am very glad to have met you all.

I am deeply grateful to my parents and family, and to my wife Lu, for their unconditional support, and for the safe, gentle, and steady comfort they have given me. Thank you for helping me through the lows that others did not see, and for giving me strong inner strength and emotional energy to keep moving forward.

Finally, I would like to thank myself. Over these years, I learned to reset my mindset in time and to keep moving forward, one small step at a time. This thesis is a concise summary of the goals and outcomes of these four years, and I hope it can serve as a modest but useful reference for others. With these acknowledgements, I close my PhD chapter with gratitude and a steadier confidence.